Swansea University
Prifysgol Abertawe

Production and Applications of Nanoparticles Grown or Deposited on Surfaces

James E. McCormack

Submitted to Swansea University in fulfilment of the requirements for the Degree of Doctor of Philosophy

Swansea University

2023

Abstract

This thesis focuses on the development of two methods of nanoparticle synthesis, the applications of the nanoparticles and the characterisation, classification, and behaviour of the nanoparticle structures. Building on the previously developed Matrix Assembly Cluster Source (MACS) technology, gold nanoparticles were fabricated using a newly created MiniMACS system, altered by using butane as a matrix gas which deposits using readily available liquid nitrogen (at a temperature of 77 K). Direct sputtering of atoms from a target material was also developed in this system, displaying the versatility of the system by the ease of switching between the two methods. This Sputtered Atom Source (SAS) technique was calibrated and subsequently used to create nanoparticles by growth of gold clusters from atoms on a carbon surface then were classified according to the cluster structure. After analysis of over 600 gold clusters identified in aberration corrected Scanning Transmission Electron Microscopy (STEM) images, it was found that clusters smaller than 300 atoms tend to have a glassy/amorphous structure, while above this size decahedral and FCC (Face – Centred Cubic) motifs compete for the dominant structure, with FCC being slightly more favourable. Icosahedral was observed very rarely when carrying out this analysis.

Dynamic analysis was also undertaken by studying a video of 500 frames of the same two clusters showing a coalescence event. Before aggregation, the larger cluster analysed structurally consisted of less than the 309 atoms that represent an "ideal" magic number cluster and crosses this threshold after the event has taken place. The dominant structure went from a prevailing decahedral shape before coalescence to an amorphous/glassy configuration, with the second most commonly occurring structure being FCC. The decahedral shape appeared much less frequently post aggregation.

The chamber housing the MiniMACS was adapted to include two probes to measure resistance in-situ while depositing atoms using the SAS method. Fabrication of gold contacts on a suitable silicon substrate was successfully achieved, allowing for the observation of a resistance profile during creation of a percolating network of gold clusters. From here, exposure to the atom beam could be correctly terminated at a point just below the percolation threshold, allowing for the creation of atomic filament growth and potential with potential to image these in the TEM.

Calibration of a larger scale MACS system was undertaken to create silver nanoparticles deposited on both copper and silver foils for use in catalysis. Lead nanoparticles were also deposited into carbon fibre paper to fabricate an electrode for use in water purification. This feat demonstrated that the MACS method is approaching rates needed for research and development in industry of the production of fuel cells, creating clusters at a rate of around 0.05 mg/cm^2/hour. This fabrication also demonstrated the depth the clusters can penetrate a porous structure, with strong signal found in the top 50 μm, and then a diminished signal at around 150 – 200 μm, numbers which correlate to the carbon paper's pore size.

This project has gone beyond that of the work carried out in the literature, whereby this reports on the first instance in which clusters created with the MACS method, with clusters been fabricated at a higher temperature than before, and as butane with a matrix gas.

Surface grown clusters were also discovered using readily available instruments that the MACS uses, allowing for quick switching between the two techniques. The non-mass selected nature of the clusters allowed the observation of single atoms, allowing investigations into the number of atoms surface grown clusters contain, classified by their structure.

Coating carbon fibre paper with lead clusters accomplished both a proof-of-concept reactive oxygen species for water purification, as well as demonstrating a high cluster yield.

Finally, instrumentation development, beam calibration and exposure recipes have lead way to large cluster coverage on the scale of percolating thing films for use of imaging filaments in a memristor device. This work has laid the foundation for further work to be developed.

Declaration

This work has not previously been accepted in substance for any degree and is not being concurrently submitted in candidature for any degree.

Signed...................█████████...

Date............................29/09/2023..

This thesis is the result of my own investigations, except where otherwise stated. Other sources are acknowledged by footnotes giving explicit references. A bibliography is appended.

Signed................█████████...

Date.......................29/09/2023..

I hereby give consent for my thesis, if accepted, to be available for electronic sharing

Signed.............█████████..

Date.....................29/09/2023...

The University's ethical procedures have been followed and, where appropriate, that ethical approval has been granted.

Signed..............█████████...

Date........................29/09/2023...

Contents Page

Permissions

No Permissions Required

List of Acronyms

Au NPs	Gold Nanoparticles
Ag NPs	Silver Nanoparticles
Pb NPs	Lead Nanoparticles
MACS	Matrix Assembly Cluster Source
MiniMACS	Mini Matrix Assembly Cluster Source
SAS	Sputtered Atom Source
TEM	Transmission Electron Microscopy
STEM	Scanning Transmission Electron Microscopy
HAADF	High Angular Annular Dark Field
DF	Dark Field
BF	Bright Field
QCM	Quartz Crystal Microbalance
PVD	Physical Vapour Deposition
SEM	Scanning Electron Microscopy
EDX	Energy Dispersive X-ray Spectroscopy
VW	Volmer-Weber
SK	Stranski-Krastanov
FM	Frank-van der Merwe

The terms "nanoparticle" and "cluster" are used interchangeably throughout this thesis.

The terms "amorphous", "unidentified" and "glassy" are also used interchangeably

Acknowledgements

I would like to thank Prof. Richard Palmer and Dr Richard Cobley for their advice, guidance, and support throughout the completion of this thesis, as well as Dr Chris Barnett for his help at the write up stage. I should also like to thank Dr Tom Slater for his TEM work at Diamond Light Source, Dr Yubiao Niu for his expertise on the TALOS TEM, and Mr Pete Davies, Mr Morris Mathews, Dr Jerome Vernieres, Dr Chiara Spadaro, Dr Rongsheng Cai, Dr Yingdi Yan, Dr Milos Baljozovic, Miss Basia Sliwa, and Dr Theo Pavloudis for their assistance throughout this project. Thank you to Dr RMM for keeping me sane throughout the writing, and finally thank you to my friends and family for their constant support, without which I would not have finished this thesis.

Titles of Publications Arising from the Research of this PhD Thesis

<u>Published:</u>

1. Fabrication of electrodes by deposition of lead clusters from the Matrix
   Assembly Cluster Source (MACS) into porous carbon paper for
   electrocatalysis.
   Kazimierska, E., Niu, Y., McCormack, J., Tizaoui, Cobley R., Palmer R.
   J Nanopart Res 25, 69 (2023). https://doi.org/10.1007/s11051-023-05717-2

2. Stabilization of two-dimensional raft structures of Au nanoclusters with up to
   60 atoms by a carbon support
   Th. Pavloudis, S. Lethbridge, J. McCormack, T. J. A. Slater, J. Kioseoglou,
   R. J. Cobley, R. E. Palmer **https://doi.org/10.1002/smsc.202400093**

3. Characterisation of the morphology of surface-assembled Au nanoclusters on
   amorphous carbon
   M Dearg, S Lethbridge, J McCormack, RE Palmer, T. J Slater - Nanoscale,
   2024 DOI: 10.1039/D4NR00978A

<u>In Preparation</u>:

1. Analysis of stable cluster structures from in-situ heating from TEM videos
   H. Hoddinott, J. McCormack, M. Dearg, T. Slater, R. E. Palmer
2. Cluster coalescence of Au nanoparticles from TEM videos
   J. McCormack, T. Slater, M. Dearg, H. Hoddinott, R. E. Palmer

Chapter 1: Introduction

In recent years, the field of nanotechnology has emerged as a critical field of scientific discovery, promising to revolutionise various industries, and pave the way for groundbreaking advancements in science and technology. At the heart of these developments lies the hidden world of nanoparticles. These infinitesimally small particles, ranging in size from 1 to 100 nanometres, exhibit unique properties and behaviours that differentiate them from their bulk counterparts. In part due to the surface area to volume ratio when compared to the bulk, their extraordinary attributes have propelled them to the forefront of research and development, finding applications in fields as diverse as medicine, electronics, energy, and environmental science.

Nanoparticles possess distinctive physical, chemical, and biological properties that arise from their small size, large surface area-to-volume ratio, and quantum effects. These characteristics enable them to interact with matter at the atomic and molecular scale, granting unprecedented control over the manipulation and modification of materials. The ability to engineer nanoparticles with tailored size, shape, composition, and surface properties has allowed a myriad of possibilities for the creation of novel materials with enhanced properties and functionalities. Nanoparticles have found their way to diverse corners of the scientific world, playing increasingly important roles in medicine. For example, nanoparticles are being explored as drug delivery systems which allow for targeted and controlled release of therapeutic agents thus improving treatment efficacy and minimizing side effects. Furthermore, antibacterial nanoparticles can be used for sterilisation of medical equipment, in electronics nanoparticles enable the development of ultra-compact devices, high-performance displays, and advanced sensors. Additionally, nanoparticles hold tremendous promise in energy technologies including solar cells, fuel cells, and energy storage devices, where their unique properties offer opportunities for improved efficiency and sustainability. Nanoparticles have the potential to address critical environmental challenges, such as pollution, water purification, and efficient catalysis for sustainable chemical processes. Their

versatility and multifunctionality make them indispensable tools in scientific research, enabling the study of fundamental phenomena, understanding of biological systems, and advancement of materials science.

Over the past few decades, gold nanoparticles (Au NPs) have been of considerable interest to the scientific and engineering communities. Many groups around the world have achieved not only the production of Au NPs, but also their incorporation into electronic and medical diagnostic devices. However, one critical failure stands out, industrial scale metallic nanoparticle synthesis generally means the form of colloids; metal nanoparticles surrounded by stabilising ligands that will more often than not need removing by other potentially harmful chemicals. Alternative methods exist that produce "pure" nanoparticles that do not have ligands attached but have the caveat of a very diminished rate of production when compared to chemical methods. This thesis aims to explore techniques that have the potential to bridge the gap between small scale production for research, and the industrial demand. The literature is reviewed in Chapter 2, theory reviewed in Chapter 3 and scientific methods explored in Chapter 4.

To achieve the overall goals of more environmentally friendly, pure, and high throughput production of Au NPs, three methods have been developed and investigated in this thesis. Chapter 5 looks in detail at the development of a MiniMACS system, which utilises an carrier gas to trap the atoms of a target material which is then subsequently bombarded with argon ions to initiate cluster growth and ejection onto a sample surface. This thesis further reports in Chapter 5 on work to adapt the MiniMACS to a comparatively simpler Sputtered Atom Source (SAS) system, a simple dynamic example of Physical Vapour Deposition (PVD). Chapter 5 reports observations made while analysing Transmission Electron Microscopy (TEM) data on Au NPs close to magic number sizes, where structural changes were observed in real time as a small cluster was "swallowed up" by a larger cluster under the beam.

Chapter 6 reports experiments carried out to assess the scale-up potential of the MACS method used in the MiniMACS system to produce Ag nanoparticles, using a scaled-up MACS system. The yield suggests that it is possible that Ag NPs can be

produced close to current industrial R&D rates chemical methods predominantly, and that the NPs can be used in applications such as electro catalysts and water purification.

Finally, the Au NPs produced using the SAS method were tested in a Neuromorphic application, an exciting and fast developing field aiming to mimic the working of the brain as an alternative architecture to current computing designs. Chapter 7 investigates Au NPs produced in Chapter 5 to create a network of clusters that imitate neural pathways.

Throughout this thesis the Au NPS produced have been imaged by collaborators on a TALOS F200X system in Swansea University and JEOL ARM aberration - correction STEM system in Diamond Light Source, Harwell. An explanation of all techniques and instrumentation is given in Chapter 3.

Chapter 2: Literature Review

This chapter reviews the literature underpinning the experiments described in Chapters 5, 6 and 7. The chapter first reviews general methods of Au NP production, including chemical synthesis, before exploring a more in-depth review of literature relating directly to MiniMACs, MACS and SAS techniques. The chapter also reviews the literature published on nanoparticle structures, work published on the uses of nanoparticles in electrocatalysis, water purification and fuel cells.

2.1 Methods of Au Nanoparticle Synthesis

In recent years there has been an acceleration in scientific and engineering interest in nanoparticles, with many groups around the world synthesising particles out of various materials using different methods for a range of applications. These applications include antibacterial coatings[1–15], drug delivery[16–28], use in ultra compact electronics[29–38], catalysis[39–87], energy storage[88–90], water purification[91–94] and bio diagnostics[95–97].

A wide range of synthesis methods have been developed which can be classified into two main categories: chemical and physical methods. Chemical methods include:

- sol-gel techniques, producing Au NPs ranging in size from 5-50 nm
- reduction in acidic environment to produce 3-40 nm Pd and Pt NPs
- reduction process to make 2-40 nm Au NPs
- wet chemistry that have been used to make Ag NPs ranging in size from 20-60 nm[98].

However, in the context of the sustainability agenda, problems with chemical synthesis include chemical waste, nanoparticle impurities, and environmental and safety concerns about the chemicals used. Therefore, physical methods (known as gas phase methods), have also been developed at a slower rate through several systems that include Supersonic Cluster Beam Deposition (SSCD), magnetron sputtering gas aggregation, direct sputtering of clusters and Swansea's Matrix

Assembly Cluster Source (MACS). In Chapters 5 - 7, Au nanoparticles are synthesised using physical methods, but it important to review more established methods to gauge the impact of this new technology and to find solutions to key questions posed by other areas. The following section of this chapter will focus on the cluster sources that produce pure metallic nanoparticles by physical methods as opposed to the chemical methods that use capping ligands to stabilise the colloidal nanoparticles.

2.2 Physical Methods of Au Nanoparticle Production

Figure 1: Portrait of William Grove, a pioneering scientist in the field of physical chemistry, renowned for his contributions to the discovery of sputtering as a technique. Grove's work laid foundational principles for the development of modern material science and surface engineering

Sir William Robert Grove, depicted in Figure 1, was a distinguished scientist, lawyer, and judge from Swansea, renowned for his invention of the fuel cell in 1839 and for his pioneering discovery of material sputtering. The research presented in this thesis draws inspiration from Grove's seminal contributions, employing sputtering techniques to develop novel synthesis methods that have the potential to

produce enough cluster flux to enable the fabrication of hydrogen fuel cells and similar devices.

Gas phase cluster sources play a pivotal role in numerous scientific and industrial applications due to their unique properties and versatility. These sources serve as crucial platforms for the production and manipulation of clusters, enabling fundamental research into cluster behaviour, structure, and dynamics. Moreover, gas phase cluster sources are integral in fields such as nanotechnology, materials science, and surface chemistry, facilitating the development of novel materials, catalysts, and devices with tailored properties. Understanding the significance of gas phase cluster sources not only advances fundamental knowledge of cluster physics but also drives innovation across various technological domains, shaping the landscape of modern science and engineering.

Eberhardt et al[99] used sputtering of platinum with a xenon plasma to create clusters of size 1 to 6 atoms, mass selected by the use of a quadrupole onto a silica surface. From here, photoemission of Pt_1 to Pt_6 was undertaken, concluding that such small clusters do not exhibit metallic characteristics akin to the bulk. Developing from this, Fayet et al[100] used the same cluster source as Eberhardt, but during deposition, cryotemperatures were used to cool the sample and incoming soft landed, mass selected clusters of Pt could be analysed in a specially designed chamber with use for photoemission. The clusters analysed in this way were monodisperse Pt_1, Pt_2, Pt_3, and Pt_{19}, mass selected with quadrupole, with supports of silver films. This impinging ion beam is called a cold reflex discharge ion source, or CORDIS. Additional developments were undertaken by Roy et al[101] with work carried out using the same initial cluster source, with platinum and palladium targets being bombarded by the xenon ion beam, which are then mass selected through the quadrupole. A UHV chamber (vacuum below 2 x 10^{-10} mbar) housed the sample, with XPS, UPS, and LEED measurements *in-situ*.

Later development came with Vadja et al[102], used the same cluster source but with the added addition of 3 more targets, totalling 4. For these reaction experiments which include size selection, need to have a high cluster flux, so the addition of three extra targets additional to the original, means four beams can be used to sputter

material. These produce negatively and positively charged cluster, as well as neutral particles. This allowed enough yield to be able to observe reactions of nickel particles with carbon monoxide, with nickel – carbonyl clusters forming, with the stability of the structure being measure by way of excitement with a laser, with the carbon ligands showing photodesorption.

The development of the nanoparticle source, with its progressively enhanced features and diverse applications, highlights the versatility and continual advancement of nanoparticle sources. Its capabilities in electronic observations and catalytic properties showcase how nanoparticle technology can be adapted for a wide range of uses. This machine exemplifies the ongoing innovation in the field, reflecting the broader trend of constantly improving nanoparticle sources to meet emerging scientific and industrial needs. The significance of this advancement lies in its ability to facilitate progress in electronics, catalysis, and other areas, demonstrating the dynamic and evolving nature of nanoparticle technology.

Supersonic Cluster Beam Deposition (SCBD)

Sputtering is a key mechanism in the method of Supersonic Cluster Beam Deposition (SCBD) [103–108] of the University of Milan, where an electrical discharge is used to ablate the target material in a vacuum chamber, inert gas is also injected at relatively high pressure which causes condensation of atoms to form clusters. The formation mechanism is the three-body cooling, in which two hot metal atoms encounter a colder gas atom that will dissipate the energy, enabling the two target material atoms to aggregate. This gas-cluster mix is then directed through a nozzle into the expansion chamber which creates a beam of clusters shaped by several apertures called aerodynamic focusers. This collimates the beam into a profile with less than 1 degree of divergence. The nanoparticles then land on a sample substrate, supported by an XY stage, allowing for control and possibly through a mask, the creation of complex patterns.

Barborini et al[109] used this method to produce graphite/carbon nanoparticles at a rate of 5nm/min. Similar results were found by Piseri[110] in 2001, where they produced clusters with a peak size of ~450 atoms with an upper tail to 2000 atoms/cluster. Barborini[111] in 2003 also produced TiO_2 NPs of a spherical foam, reaching sizes of ~10nm. They also observed that annealing, post-synthesis, results in larger clusters. Meanwhile, Ghisleri et al[112] (part of the same Milani group as Barborini) used the same method to produce Au-NPs embedded in PDMS with mean diameter 3.9 ± 1.4 nm at a rate of 0.02nm/s, characterised using AFM.

Magnetron Sputtering Gas Aggregation Source

The SCBD method has been shown to produce nanoparticles of different materials, however size selection is difficult because of the tendency of the clusters formed to be neutral. Therefore, when size selection of clusters is required, a magnetron sputtering gas aggregation source has been used by several groups to tackle this problem.

The magnetron source uses a vaporisation technique to bombard the surface of a target material, liberating the atoms from the surface. The vaporisation is achieved by igniting a plasma from a gas (usually argon) by ripping the electrons away from the nucleus by introducing a potential difference between two plates. These ions are then attracted to the cathode which sits behind the target. To increase efficiency of the vaporisation process, a magnet is placed in conjunction with the cathode, encouraging a higher flux of ions to bombard the surface of the material. As with the SCBD technique, the introduction of a cool carrier gas into an adjacent chamber promotes three-body collisions, promoting nucleation and growth of clusters. One of the biggest advantages of the magnetron source is that of the resulting synthesised clusters, around 30% are positively charged, meaning that electrostatic lenses can be applied to manipulate the path of these clusters. Some variations of the magnetron cluster beam sources have a mass selection chamber, sometimes using a quadrupole mass spectrometer which filters out user controlled mass through alternating an electric field to control the path of specific masses from their mass to charge ratio, or the use of an infinite range, time-of-flight (TOF) analyser which changes the lateral direction without affecting the initial speed or shape of the beam. This displaces the selected nanoparticle size while filtering out other sizes[113].

For example, Pratontep[114] et al used this method to create size selected Au cluster of 100 atoms, Ag clusters of 8,000 atoms, Cu cluster of 60,000 atom and Si cluster of 20 atoms, demonstrating the time of flight (TOF) mass filter to size select clusters. Haberland et al[115] have used a magnetron source to vary cluster size between 50 and more than 10^6 atoms per cluster, showing the landing of accelerated clusters of varying energies, while simulating the landing. Clusters will become flatter with more energy during flight, eventually creating a crater with 10 keV.

The versatility of the magnetron sputtering technique means that it has become one of the most widespread methods of gas phase production of clusters. Additional target heads have been utilised to facilitate the creation of clusters consisting of two, even three materials, i.e., alloyed materials of binary and ternary clusters. As an example, Singh et al[116] have accomplished this, creating such structures as core-shell nanoparticles – with a Pd core and a MgO shell. Two other cluster types that can be created are the Janus structure, and the alloyed cluster. Core-shell clusters are a promising technology in several fields. Researchers can engineer them with specific functionalities such as enhanced stability, and surface functionalisation thereby enabling interactions and compatibility with other materials[117].

There are two issues with magnetron sputtering method. The first is that clusters are weakly landed upon the surface, and the second is scale of production. Therefore, the Alton Cluster Source and the Matrix Assembly Cluster Source (MACS) have been developed and are of great interest to the nanotechnology community.

Alton Cluster Source

The Alton Source is an instrument that has unique way of fabricating predominantly negative clusters. G. D Alton, from Oak Ridge National Laboratory, sought out to build a material source to use as a universal negative or positive ion source[118], using work carried out on negative ion production of various elements by Krohn et al[119]. The different approach incorporates a technique based on sputtering material, as standard cluster sources do, but by swapping an inert gas, with caesium as a positive ion source. Additionally, a small monolayer of caesium is deposited onto the target material in order to reduce the material's work function, or will naturally

form/implant into the target surface through the ion sputtering step. This works from "…classical surface ionisation theory…"[118] whereby a dissimilar surface is coated with a monolayer of an alkali material, the work function is lowered due to the readily available "spare" electron present in the outer shell (group one in the periodic table), donating it to the target material. The amount the work function is lowered, is determined by the electron affinity the material has, which in turn determines the amount of negatively ionised particles that leaves the surface when sputtered. For better optimisation, a thin layer is thermally sputtered onto the target surface before sputtering. Negatively charged clusters are of interest, not only due to the rarity of creating negatively charger nanoparticles, but due to the nature of potentially having a higher affinity to bind positively charged species, such as the work carried out by chemical methods by Reddy et al [120], where negatively charged silver atoms were synthesised, and functionalised through electrostatic interactions with a polymer.

The source underwent several different designs, optimising the design with each iteration[121]. S. G. Hall et al.[122] retrofitted the source with ion optics and mass selection properties, with the use of a Wien velocity filter. Electrostatic plates are used to filter out clusters that do not meet velocities of $v=E/B$, where v is velocity of the particle, E is the electric field and B is magnetic field. This can be tuned with changing the power on the filter. Additionally, to filter out neutral cluster unaffected by the filter, the beam is deflected through a 10-degree change after the Wien filter causing neutral particles to deposit onto the wall.

A reduction of extraction energy of material has been reduced from the 20 kV in the past, to 1.5 kV, which allows the Wien filter to work. Lowering the energies even more narrows the size selection range of the nanoparticle, allowing for high precision of size selection to occur. The Alton source can create clusters of atoms of 1 - 20 atoms. With a sample bias, the clusters can either be soft landed onto the sample surface, or can be accelerated to land energetically, implanted into the surface. Pratontep et al used the Alton source to create negatively charged ions of silver and gold with size seven atoms. They were then accelerated into the surface of a highly oriented pyrolytic graphite (HOPG) sample, implanting the nanoparticles[123]. One negative to this technique is the very low yield of clusters fabricated. In its current configuration, clusters must be size selected, and the narrow band of the size

selection range means that only a small amount of target material is collected onto the sample.

This technique is not widely used and is limited to one group currently based at Swansea University.

MACS

Although the Alton Source is excellent for very small cluster formation, and like the magnetron source allows mass selection of charged clusters, scale is an issue. The Matrix Assembly Cluster Source is a novel way to create clusters that bridge the gap between traditional gas phase production and industrial demand. The research reported in Chapter 6 demonstrates the scale up potential. A copper block is cooled with liquid helium to around 12 K, existing as a cold surface for condensation of an inert gas. Simultaneously, a target material is evaporated towards the copper surface where the gas is forming, becoming trapped in the still growing, solidified gas - forming a matrix of the two components. The work carried out shows that optimum metal loading ranges from 1-4% by number of atoms[124]. Once sufficient growth has been achieved, introduction of the gas and evaporation of the target material is ceased. The next step involves the bombardment of this matrix by an ion beam, an acceleration voltage of between 100 V and a several kV, with a beam current of 10 - 100 mA. Ions are accelerated towards the metal-gas matrix, resulting in an injection of energy into the system which causes a cascade of collisions between the trapped metal atoms. These collisions leads to nucleation and growth as well as ejection of clusters from the solidified gas to generate a cluster beam. The same mechanism as other cluster sources is used by way of three body cooling, where the solid gas acts as the cooling source.

MACS clusters have been studied in several areas such as catalysis[125] and previous structural analysis[126]. Clusters from the MACS can also be made to have ligands, allowing for enhanced stability and resistance to chemical degradation[127].

Palmer et al[128] first reported the MACS technique in 2016 by way of producing Au and Ag NPs using an Ar rare gas matrix cooled using helium gas to 15 K. Further work carried out on the MACS system by Oiko et al[129] used CO_2 as the matrix gas at a temperature of less than 20 K and produced Ag nanoclusters, of size ranging from

80 to 175 atoms, with the variance due to different matrix loading. Molecular dynamics simulation of the formation mechanism has been carried out by Zhou et al[124] and shows that the cluster growth mechanism can be described as thermal spike enhanced clustering. Thermal spike enhanced clustering is a process where a brief, but intense burst of heat (a thermal spike) occurs when energetic particles collide with a material. This sudden increase in temperature helps atoms in the material to move around and cluster together more effectively, leading to improved formation of structures, in this case, nanoparticles.

The MACS technique has been demonstrated to use a variety of target materials for cluster synthesis. In a publication in Applied Energy Materials, Xu et al[130] a report on the synthesis of Co NPs of diameter 3.2 nm, surrounded by a number of 1.8 nm clusters were created. These were then used for efficient and stable oxygen evolution. The use of cobalt and ruthenium clusters helps in maintaining the structural integrity and performance of the catalysts over extended periods, thus enhancing their stability during the oxygen evolution reaction. They also outperformed commercially available Ru/C and RuO_2 particles in both stability and specific activities. Development on the MACS configuration has been carried out by Cai et al[127] to deposit sized-controlled Au and Ag NPs on a water-soluble thin film of polymer, which are then dissolved in order to make a colloidal suspension of metal in a polymer film. Different types of water-soluble thin films have been shown to work, such as polyvinylpyrrolidone, polyvinyl alcohol and polyethylene glycol.

Scale up potential has been demonstrated by Cai et in 2020[131,132], who deposited Au and Ag NPs onto gram scale powders of TiO_2 for heterogeneous catalysis for propylene combustion and ozonation of nitrophenol. MACS operation is discussed in Figure 13.

2.3 Structural Isomers of Gold

Chapter 5 of this thesis reports on observations of the structure of Au NPs with the aberration – corrected STEM. In this section, some of the literature relating to structural isomers of gold nanoparticles is reviewed.

Bulk gold has a face-centred cubic structure (FCC), meaning that the unit cell arrangement of the atoms is a cubic structure, with atoms residing at the corners and in the centre of each face. However, NPs of gold can form other structures depending on the number of atoms in the cluster. Iijima and Ichihashi[133] published in Physical Reviews Letter in 1986 a paper where they observed structural instability of a 2 nm gold cluster while carrying out TEM. Their results showed different orientations of FCC structures, meaning energy imparted from the electron beam to the cluster influences its structure. Work carried out by Jennison et al[134] showed that 55 and 135 atom clusters of Ru, Pd and Ag showed both cuboctahedral and icosahedral forms. Koga et al[135] studied the structure of gold nanoparticles and found that near the melting temperature, clusters between 3 nm and 14 nm undergo structural changes from icosahedral to decahedral. Similar observations were also made by Kuo and Clancy[136].

The first ac – STEM study of size selected clusters by Li et al[137] have used multi-slice STEM simulation alongside experiments to identify that gold clusters of 309 atoms can be decahedral, icosahedral or FCC. Wang. Z. W and R. E. Palmer[138] created a simulation atlas in which many orientations of cluster structures were simulated for reference against experimental results. These simulations focus on the ideal numbers of atoms that make a "full" shape, being referred to as "magic number clusters".

2.4 Uses of Nanoparticles for Electro Catalysts, Water Purification, Fuel Cells and Neuromorphics

It has been mentioned in the previous section that the MACS method can produce nanoparticles for catalysis. In this section additional examples of the use of Au nanoparticles are discussed.

Nanoparticles have been used by several groups as a catalyst for hydrogen production. Heidary and Kornienko[80] studied 5-hydroxymethylfurfural (HMF) on gold nanoparticle surfaces to understand reactivity for water splitting. By using operando Raman spectroscopy, the researchers can observe the behaviour and transformation of molecules on the catalyst surface, providing insights into the

reaction mechanisms. This helps in understanding how the gold nanoparticles facilitate the oxidation of HMF and in designing more efficient catalytic systems. Chadderdon et al[139] have used bimetallic Pd-Au to oxidise HMF to 2,5-furandicarboxylic acid (FDCA). Chapter 6 reports on experiments in which Ag-NPs produced using the MACS method have been deposited onto foils to improve the rate of HMF reduction. This collaboration builds on work has previously been researched by the University of Bologna. Sanghez de Luna et al[140] published a paper in 2020 where they deposited Ag films on Cu open cell foams and compared the results to Ag films deposited on Ag and Cu foils. They found the combination of silver and copper foams increased the rate of conversion for HFM to 2,5-bis(hydroxymethyl)furan (BHMF) by around 4 times compared to silver their foil counterparts. The next logical step is to use a higher surface to volume ratio – i.e. nanoparticles.

Nanoparticles have also been used to great effect for water purification and enhanced battery cathodes. Salazar et al[79] created a Ni nanoparticle carbon fibre paste that was electro spun to create a carbon fibre with spherical nanoparticles firmly embedded throughout. Chapter 7 reports on experiments that produced similar impregnation of nanoparticles in a fibrous carbon paper sample using the MACS method to create the clusters. Work by Liu et al[78] has demonstrated that it is possible to grow carbon nanotubes from metal nanoparticles embedded on the surface of a carbon fibre which was then used as a cathode for enhanced battery performance.

Chapter 7 discusses experiments carried out as part of this thesis to utilise Au-NPs produced using the Single Atom Source (SAS) method in Chapter 5, to form nanoparticle films just below the point of percolation for implementation in the field neuromorphic computing. Bose et al[141] in 2017 published a paper in IEEE Transactions on Electron Devices, reporting work involving the induced formation of filaments between oxidised tin nanoparticles. This work has evolved, with the same group publishing in 2022 a method to evaporate gold to form a discontinuous nanoparticle film, showing switching properties and neuron – like electrical signals, supported with simulations[142]. Minnai et al[143] have created memristive devices using gold nanoparticles deposited below the percolation threshold in between two electrodes supported by an insulting surface of glass. Mirigliano et al[144] also used

gold nanoclusters to create a memristive device from a film that was beyond the percolation threshold. The switching nature of the device does not come from filament growth as it is theorised with a network of clusters below the percolation threshold. Instead, with a cluster based, thin film (as opposed to a discrete layer of individual clusters), the non-ohmic behaviour of the complex resistive switching arises from nanogranular structure. The non-uniformity of the cluster film allows for the presence of defects and junctions, which affects the transport of current while being dynamically rearranged.

Marinella et al[145] has reported the use of memristor devices in use of reservoir computing. Reservoir computing is a computational framework based on recurrent neural network theory. It achieves its functionality by transforming input signals into higher-dimensional computational spaces via the dynamic behaviour of a fixed, non-linear system known as a reservoir. An input is fed into the reservoir, which is treated as a "black box", a readout mechanism is trained to map the state of the reservoir by previous training of the system. The synaptic weights of the reservoir are determined by previous training of the neural network. In other words, the memristor readout will depend on the data/signal it has "remembered" before. An array of these devices will allow for large parallel computing to be undertaken, which is useful for large datasets where fast output is essential, such as pattern recognition[146], analysis of neural signals in real time for neuroelectronic applications[147], and real time signal processing[148].

Chapter 3: Theory

This section of the thesis will describe, in detail, the theory work that underpins the core methodologies and techniques employed in this research. Starting from the very basic building blocks on the foundational physics that govern nanoparticle growth, to techniques that facilitate this, to applications of these clusters. The intricate field of neuromorphic computing provides the cognitive blueprint, emulating neural architectures and functionalities of human brain to enhance computational efficiency. These theoretical frameworks collectively inform the experimental and analytical techniques utilised, facilitating advancements in material science and nanotechnology.

Sputtering
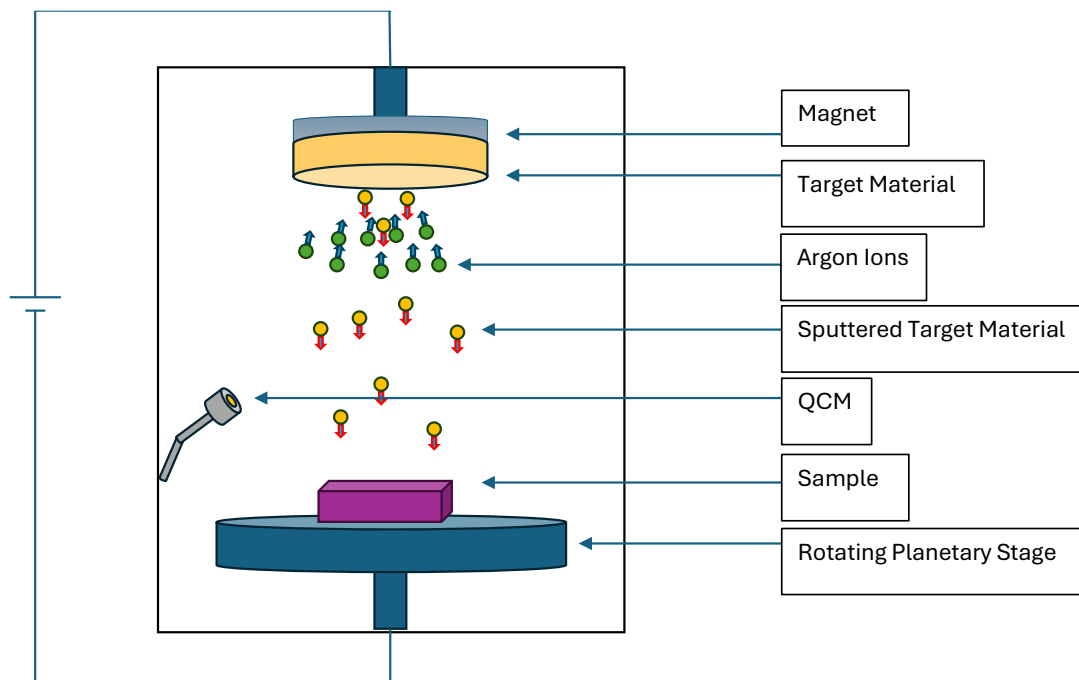
Figure 2: A schematic of a sputter coater. The inert gas is introduced to an electric field, ripping off electrons and accelerates the ions towards the anode (with the target material in the path), knocking off target material on an atomic level

Physical vapour deposition (PVD)/sputtering is a crucial technique in the thin film fabrication field and can be used to create surface grown clusters (described later in

this chapter). The most common type of sputtering is magnetron sputtering, which as the name implies, uses a magnetron to direct ions to a target material. A target material sits in front of a cathode in a vacuum chamber. Inert gas (usually argon) is introduced between the cathode and anode, where plasma is ignited, and the ions are attracted to the target at high energies. The subsequent liberated atoms are then ejected out of the target material and onto the sample. Rates are very high due to the physical close packed nature of the chamber meaning several nanometres of material can be deposited within seconds, making magnetron sputtering systems very efficient for thin film deposition. A rotating planetary stage sits at the bottom usually, meaning that samples can sit and change speed during sputtering for an even coat all over the sample, this is especially useful for very porous samples such as fibres. The thickness of the film is determined by a quartz crystal microbalance (QCM).

Quartz crystal microbalance (QCM)

A QCM is used to determine the thickness of an adjacent sample during deposition. Usually used in PVD or sputtering, the QCM is an invaluable tool keeping track of how much material is evaporated/sputtered. A quartz crystal sits in a housing of steel with the actual crystal exposed to the beam. A monitor measures the frequency at which the crystal is exhibiting, with frequency getting smaller as more material lands on the surface.

Crystal Structure of gold nanoparticles

Gold clusters of small atomic volume will tend to be one of three crystalline shapes, decahedral, icosahedral or FCC in the shape of cuboctahedra. Due to the TEM's 2D image representing a 3D space, different orientations of the cluster may not initially be intuitively sorted into these three shapes. Previous work done on the multi-slice method shows a comprehensive simulation of perfect magic number clusters in differing orientations to use as a cross reference for identifying. Standard models of XYZ coordinates of each cluster relative to each other were used as a basis for the simulation. The QSTEM simulation package was then used with a "multi-slice"

method of simulating the electron beam in a microscope. This simulates the beam in different planes to produce a final STEM simulated cluster close enough to allow for comparisons with real life data.
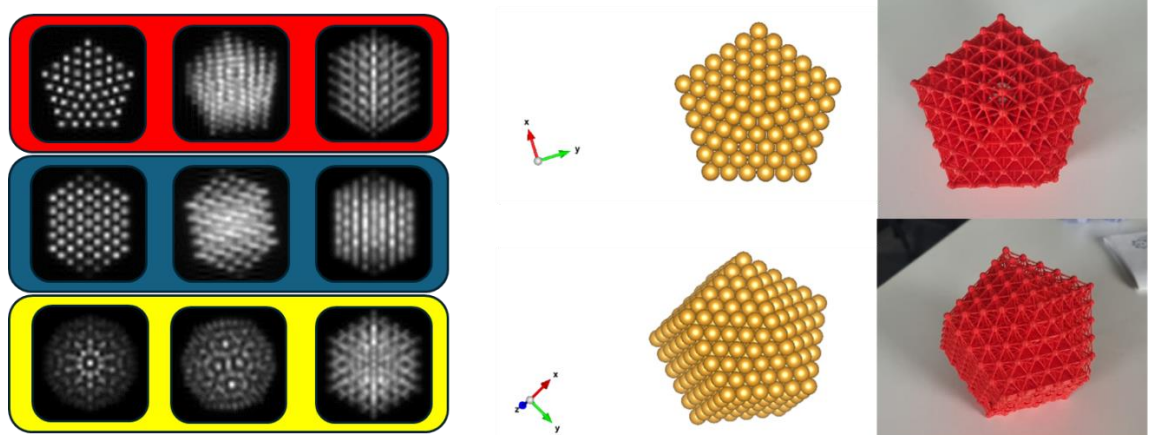

Figure 3: a) Examples of different orientations of projected simulated clusters using the multi-slice method. The top row simulates decahedral, the middle row simulates FCC (cuboctahedral) and the bottom row simulates icosahedral. b) shows a VESTA simulation of positioning of the atoms in reference to each other in a decahedron, with a 3D printed model of that XYZ coordinate file. The number of atoms in both simulations and 3D printed model is 561

Aggregation

Due to the methods of cluster fabrication pursued in this project, aggregation of small clusters/single atoms is important to understand. Two different methods of aggregation will come into play during later chapters of this thesis that explain specific sizes of clusters. These two mechanisms are called Ostwald ripening and Smoluchowski ripening.

Ostwald Ripening

In a nutshell, Ostwald ripening it's the growth of larger particles at the expense of smaller ones, in the nanoparticle world the smaller cluster donates its atoms to the larger cluster before both settling in a stable configuration leading to usually a

bimodal distribution. Usually for this mechanism to occur both clusters are pinned to their position, with atoms diffusing from one cluster to the other, due to dependence on vapour pressure, as well as the adatom-surface bond being greater than that of the adatom-adatom bond. Clusters found in later chapters of static images have a bimodal distribution most likely caused by Ostwald ripening due to the surface grown nature of the clusters[149].

Smoluchowski Ripening

Alternatively, Smoluchowski ripening occurs when a smaller cluster migrates and is completely absorbed into a larger cluster. Sufficient energy of the whole cluster will overcome adatom-surface bond strength allowing for this migration and coalescence to occur. In the case of the aggregation event that occurs later in this thesis, the extra energy to allow this diffusion possibly comes from energy injected into the system from the electron microscope. In the TEM, electrons with an acceleration voltage of 200 kV are accelerated and hit clusters of below 3 nm with a fast scan speed, meaning the cluster is exposed to a lot of high energy as well as high current. In the video seen later, cluster growth had ceased several days before (fabricated in a lab then transported a few weeks later to the TEM), and effectively had stopped growing. The addition of the energy facilitated growth through Smoluchowski ripening[149].

Surface grown cluster formation

There are two main modes of cluster formation that are relevant in this thesis, colloquially termed pre-landed cluster formation and surface dependant cluster formation. Conventional cluster sources described previously (magnetron cluster source, Alton source, MACS) all create clusters in-flight, meaning that there is a "minimum" size cluster that will appear on the sample surface. Conversely, surface grown clusters rely on the aggregation of somewhat energetic single atoms landing on a surface and meeting. They are highly surface dependant with differing fundamental growth modes that determine the outcome. At a glance, there are three modes of surface growth, island growth (Volmer-Weber), layer by layer (Frank-van

der Merwe) and a mix, island on layer (Stranski-Krastanov). When an target material atom comes into contact with the sample, a bond is formed. Depending on how strong that bond is relative to other target atom bonds, will determine what outcome the larger structure will take.
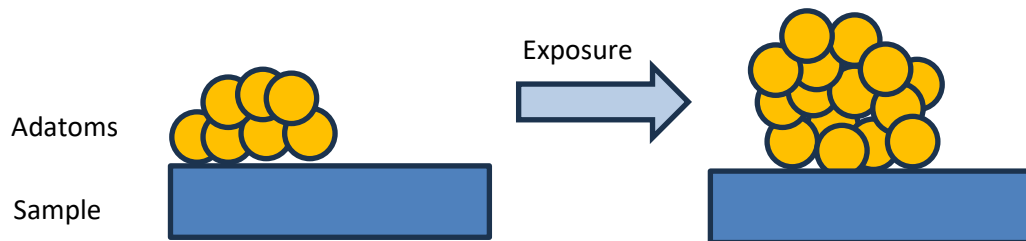

Figure 4: Diagram of Volmer-Weber growth. As atoms are deposited on the surface, the force of atom – atom attraction is stronger than atom – surface attraction, leading to cluster formation

Volmer-Weber growth

Volmer-Weber (VW mode) is the predominant form of cluster synthesis in the "Single Atom Sputtering" described in this thesis. Sputtered atoms arrive on the sample surface, and provided that the adatom-sample bond is weaker than the adatom-adatom bond, then the outcome is island/cluster growth. According to "Thin Film Materials: Stress, Defect Formation and Surface Evolution":

 "For most film-substrate material combinations, films grow in the Volmer-Weber (VW) mode which leads a to polycrystalline microstructure." "…the distinguishing feature of this growth mode is that deposited material gathers into discrete clusters or islands on the substrate surface from the outset, with no tendency toward planar growth. Thereafter, the microstructure evolves through a sequence of stages that is characteristic of a wide range of material combinations. Following the initial nucleation of islands of film material, successive stages typically include: island growth, island-to-island contact and coalescence into larger islands, establishment of large area contiguity, and filling in of the remaining gaps in the structure to form a continuous film"[150]. This an important detail to note as this mode will work if trying to create a percolating film of clusters by using a voltage to induce filament growth,

as current will travel in the expected path of the clusters and not any underlying layer. Previous work has shown larger cluster formation occurring in defects on a step, on a graphite substrate. This is an example of VW mode, with "…larger particles arising from diffusion and aggregation of deposited clusters, are visible with the scanning electron microscope (SEM)…"[151].
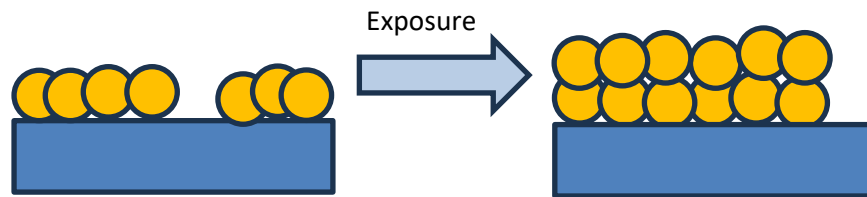
Figure 5: Diagram of FM growth, atoms will prefer to fill in gaps and adhere to the sample surface as opposed to clustering up to other adatoms, causing this layer-by-layer growth

Frank-van der Merwe growth

Frank-van der Merwe growth (FM mode) is a planer/layer by layer growth, occurring when adatom-adatom weaker than adatom-surface bonding. Meaning when an atom of target material lands on the substrate surface, surface diffusion may occur but will tend to be strong enough to not allow any adatom to diffuse on top of other adatoms. As more and more atoms land on the surface they eventually will build a thin film. Eventually the next layer will be built but depending on temperature of the surface, another layer will be built on top of that, ad infinitum until deposition ceases. For obvious reasons this mode of growth is highly unwanted in this work.
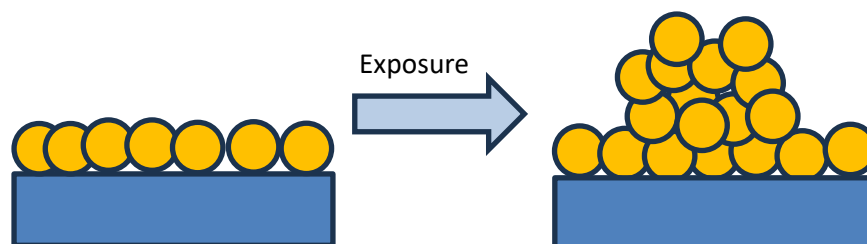
Figure 6: Diagram of SK growth, a mix of the first two modes of growth, clusters will form a layer before forming a cluster above the layer

Stranski-Krastanov growth

Stranski-Krastanov growth (SK mode) is a mixture of the two preceding modes, island growth on top of layer growth. After a few monolayers of target material has been formed, the crystal structure of the thin film becomes better defined, SK mode is preferential when heavily strained stresses occur due to substrate alignment/interference[152]. As with FM mode, this mode is undesirable. If neuromorphic experiments are to be undertaken, a voltage will be applied across clusters and immediately the circuit will be shorted through the bottom layer of epitaxial target growth, not through the desired path of the clusters.

By utilising the theory of PVD and the VW growth of clusters, an alternative method to MACS cluster growth is readily available with minimal alterations to the set up. Single Atom Source (SAS) consists of an ion beam sputtering the target material, with clusters growing in the VW mechanism of growth to produce nanoparticles.

Chapter 4: Scientific Methods

This chapter introduces Transmission Electron Microscopy (TEM) that was used to carry out characterisation of the Au NPs produced throughout the experiments described in this thesis. This chapter is an explanation of the theory of TEM and the instruments used.

4.1 Transmission Electron Microscopy (TEM)

4.1.1 Introduction

TEM is an analytical technique that can provide atomic scale images with resolution less than 0.1 nm. TEM relies on a beam of electrons that is directed toward and transmitted through the sample to form an image. In Scanning TEM (STEM), The electrons hit a feature on the sample and are scattered hitting several detectors that sit below the sample. The first TEMs were constructed by Paul Anderson and Kenneth Fitzsimmons in Washington State University in 1935 and Albert Prebus and James Hillier in University of Toronto in 1938. TEM along with other electron microscopy techniques such as the Scanning Electron Microscope (SEM) have continued to develop improvements to resolution and increased functionality.
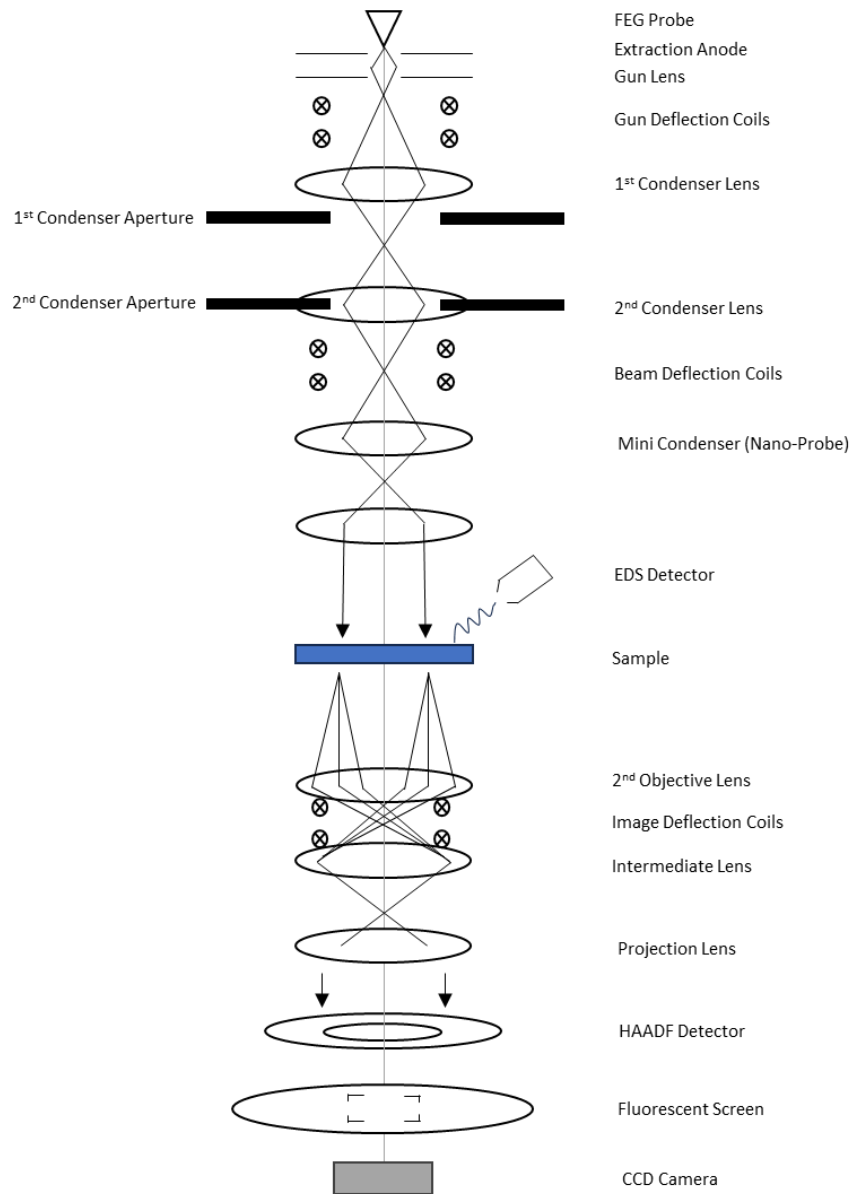
4.1.2 Theory

FEG Probe
Extraction Anode
Gun Lens

Gun Deflection Coils

1st Condenser Lens

1st Condenser Aperture

2nd Condenser Aperture   2nd Condenser Lens

Beam Deflection Coils

Mini Condenser (Nano-Probe)

EDS Detector

Sample

2nd Objective Lens
Image Deflection Coils
Intermediate Lens

Projection Lens

HAADF Detector

Fluorescent Screen

CCD Camera

Figure 7: A cross-sectional diagram of a TEM, developed and recreated from KNI lab at Caltech

Figure 7 shows a cross-section diagram of a Transmission Electron Microscope (TEM). Electron microscopes can be analogous to their light microscope counterparts, but utilizing electrons instead of photons and electromagnetic lenses instead of glass lenses[153]. Due to their small size and weight, electrons are highly prone to scattering. Atmospheric molecules will interfere with the path of the electron, resulting in a poor image quality. To resolve this, the electron source and

24

sample are kept in a high vacuum (HV) to ultra-high vacuum (UHV) environment. The electron source, usually a tungsten filament, has a very high voltage, ranging from 80kV to 200kV on standard TEMs. Due to the high volume of electrons released by the filament, several apertures are needed to filter out everything except for the relevant electrons that are normal to the sample surface. Akin to eyes, if too many photons emitted from a source are detected, then the eye will automatically adjust to filter the excess. Similarly with the TEM, too high a signal will require a smaller aperture as a filter, with consideration on balancing signal and resolution. Due to small tilts on the surface, the beam will have some astigmatism affecting the final image. This is corrected in the x and y direction of the beam to become perfectly circular from the point of the detector, allowing for even more clarity during imaging. This is accomplished through the adjusting the strength of the fields of the lenses to manipulate the shape of the beam in the x and y direction. This is a vital step in getting high resolution clarity, as the final image may well be in focus but will look very distorted if the astigmatism is not dealt with. Due to the nature of TEM imaging being the image of the reciprocal space, the sample must be sufficiently thin to allow electrons to pass through. The thicker the sample, the smaller the mean free path of the electron is, resulting in more scattering events, thus creating a large loss of detail. The mean free path is a useful observation that highlights the need for thin samples. The definition is the length of the path that an electron will take before an interaction that causes a significant scattering event. In this thesis, the mean free path inside the sample is the most relevant. The thicker the sample, the probability of another significant scattering event will increase. So, as said before to minimise scattering events (or increasing the mean free path), the sample must be as thin as possible.

Another way of resolving resolution is to consider the relationship of wavelength and spatial resolution. Knowing that they are proportional, increasing the electron voltage will decrease the wavelength of the electron. To put this into perspective, the average SEM will operate at usually a maximum of 30 kV acceleration voltage. The Talos F200X system maximises at 200 kV. Labs in Japan followed this development route and has a TEM that can supply 1MV worth of energy. Despite having such a high resolving instrument, not all samples can handle this level of energy and will deteriorate over time. Other higher end TEMs have kept to the 200 kV range, but have included aberration correction . These top-of-the-range microscopes can image

single atoms with relative ease using advanced electro-magnetic lenses to reach sub-atomic resolution. These are housed in a vibration-free, soundproof and environmentally neutral room, with the operator controlling the system in a separate room, due to the fact that even sound from speaking can cause vibrations in imaging.

Imaging

To image a sample with S/TEM, the number of scattering events the electrons encounter during their pass through the sample, must be minimised before deflecting onto the detector. Dark Field (DF) and Bright Field (BF) detectors work with regards to angle deflected. If an electron encounters and is deflected a single atom, there will be a clear signal and sharp image shown on the computer software. Thicker samples will cause more scattering events, causing the image to become blurred.
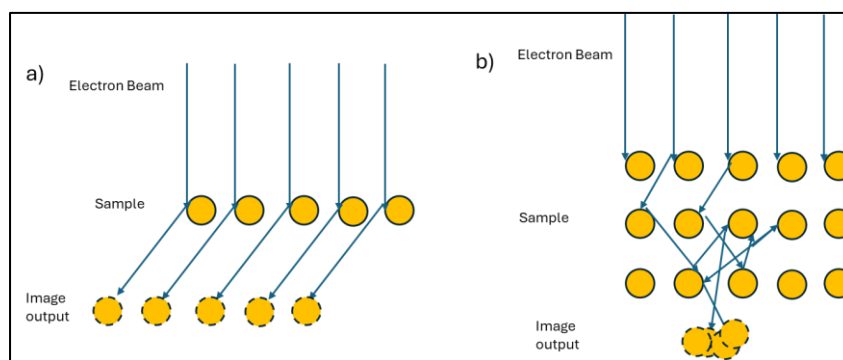
Figure 8: A visual representation of the path an electron will take in TEM, with a) a thin sample, and b) a thick sample. The thinner sample will have very few deflection events, producing a very clear image. Electrons will experience more of these deflection events the thicker the sample is, projecting a blurred image

To optimise this, samples must be electrically transparent to be able to allow electrons to pass through. There are several techniques to prepare samples for TEM to achieve areas thin enough to allow for electron transparency, each sample dependant. For powders, a suitable technique to use would be the drop-cast method, in which powder is placed into an alcohol - such as isopropanol, then deposited onto a TEM grid. The grid is then left to dry leaving behind only the powder. Simpler methods are used for metallic nanoparticles. Existing in small enough spatial volumes, no preparation is needed, just an exposure of a TEM grid to the nanoparticle beam. However, they must be supported onto a suitable film on the

TEM grid. Ideally made of an atomically light material (such as carbon) to allow a good contrast between support and sample. Thickness of the film should be sub 50nm to minimise the mean free path of the incident electron beam. For steel samples, a twin - jet TenuPol by Struers can be used to punch a hole through the material, leaving a thin enough area on the rim to be imaged. It operates on the basis of electro-polishing, where an electric current is passed through a specimen submerged in an electrolyte solution, in which the electrolyte is dependent on the material. Automatic stopping of the polishing process occurs when light (or a hole) is detected through the sample. The areas of around said hole are thin enough to be electron transparent, allowing imaging in the TEM to be carried out. This electro-polishing is highly localised, causing a small hole on the micron scale as to not affect the structural integrity of the rest of sample, making it reliable during mounting for TEM.

Alternatively, the Precision Ion Polishing System (PIPS II Bet by Gatan) is a more controlled method of thinning out samples, allowing for both top and bottom sides of the sample to be milled simultaneously, hence being structurally more stable than single side milling. One of the most eminent uses for TEM is for the semiconductor industry. With manufacturing of devices coming down to the nanometre scale, TEM is an essential tool to visualise the processes. A Focussed Ion Beam (FIB) SEM is used to extract a micron scale deep cross section from the bulk and then subsequently thinned. The sample is thinned until the area of interest has become electrically transparent at 5 kV electron beam acceleration voltage, using the lower detector (in the case of the Zeiss Crossbeam 550), which is called the Secondary Electron Secondary Ion (SESI) detector. This detector can be used as an indication of electron transparency, with lighter contrast on the area of interest indicating electron transparency when viewed in the TEM.

Other Modes of TEM: STEM

Scanning Transmission Electron Microscope (STEM) is a form of TEM where the incident electron beam will raster scan across the sample. The resulting scattered electrons are collected using various detectors positioned under the sample to produce images that can give further structural and chemical information.
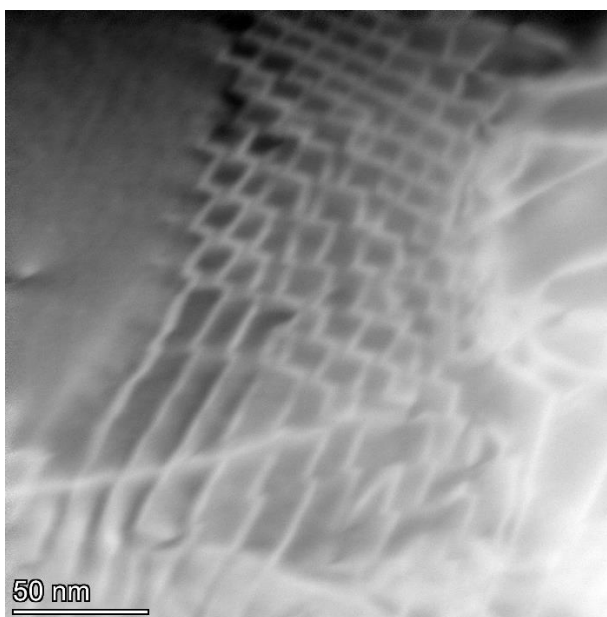

Figure 9: HAADF STEM image of a steel sample thinned with a Tenu-Pol. Screw dislocations are observed here, with nanoparticles terminating the propagation. This is what is thought to give the steel its mechanical strength

Figure 9 shows a HAADF STEM image of a thinned-out steel sample, displaying screw dislocations. The Talos TEM (discussed later on in this chapter) is one of the main microscopes that helped carry out the majority of the work found in this project. It is equipped with both TEM and STEM modes, with several detectors used specifically for STEM. One of the most important detectors that has relevance for nanoparticles seen in this thesis is the High Angular Annular Dark Field (HAADF) detector. Sitting relatively close below the sample, the HAADF is a disc shaped detector that shows a high contrast of heavier elements compared to light elements. This due to the higher deflection angle electrons take after being scattered in relatively dense materials (such as gold). To take advantage of this, samples with a heavier atomic weight (such as gold nanoparticles) sitting on a very thin film of a light atomic weight material (like carbon) will produce the best contrast to get the optimum image. Several other detectors are found on the Talos such as the Dark

Field 4 and the Dark Field 2 (DF4 and DF2 respectively) which work on the same principle as the HAADF but for less deflected electrons (i.e. medium-heavy elements with respect to a material like gold). Finally, the bright field detector (BF) which highlights the lightest elements with least deflection. The detector is a flat disc that sits directly underneath the sample. The contrast in this case is inverted, with light elements showing a contrast as white and heavier elements shown as black. For the three dark field detectors, the lighter the pixel, the more scattered the electron has undergone. So, this could either be due to density or thickness of the sample. Usually, a sharp, but light image will depict a heavy element, whereas a blurry but light image will depict a thick sample.

EDX

Energy Dispersive X-ray (EDX) is a technique that allows for chemical analysis of the sample.
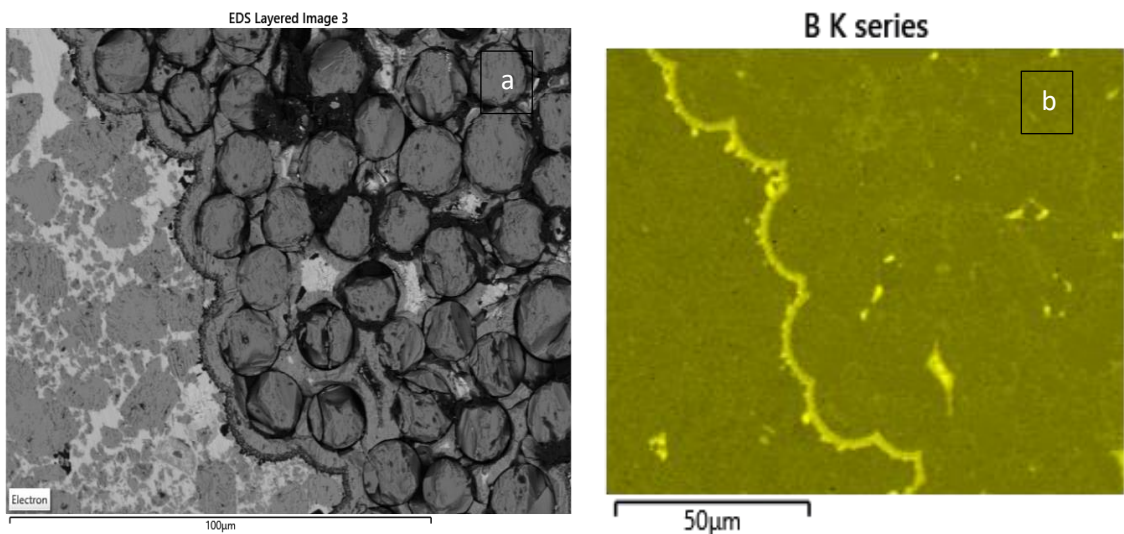

Figure 10: a) An SEM image of carbon fibres, b) 16 hour EDX map of the same area, showing Boron as a coating

Figure 10 shows an image of a map of a sample taken by the JEOL 7800F FEG-SEM, with an Oxford Instruments EDX detector. An incident electron from the SEM/TEM beam excites an electron in the sample material, promoting it to a higher shell. This unstable state results in an electron falling to a lower energy state to fill

the gap by way of releasing energy in the form of x-rays. Each element has semi-distinct x-ray energy peak/s, which can be cross referenced to previously calibrated energies. Throughout regular scanning during imaging, x-rays are being emitted from the sample consistently. To detect this, the Talos is equipped with four x-ray detectors sitting above the sample. The software will log and plot the incoming x-ray energy during the raster scanning, assigning an element with the corresponding energy peak to the position of the image, building up an elemental map over time. However, care must be taken when selecting the holder that houses the sample. Due to interaction volumes, secondary electrons emanating from the sample may strike the other parts of the sample, or even the holder itself. These secondary electron interactions emit their own x-rays which can alter the energy map. Using a standard brass holder may cause significant amounts of copper and zinc signals which can be avoided by using a beryllium holder. Being a comparatively rare material in a lot of uses, beryllium data on the software can be readily ignored and removed from the results. Despite EDX usually struggling with lighter elements, the latest detectors have a high enough channel resolution that can achieve clear detection of elements as light as boron, demonstrated by Figure 10. Boron coating the carbon fibre was revealed after a 16-hour exposure had been undertaken.

4.1.3 The Instrument

Figure 11 shows the FEI Talos F200X, the main microscope used for most of the results in this thesis. With a resolution of 1.6Å, the Talos has very high spatial resolution, capable of visualising columns of atoms in nanoparticles when the alignments are correct and the particle orientation is suitable.

Figure 11: FEI Talos F200X System at Swansea University

Due to the very small scale that imaging is carried out, vibration isolation is of utmost importance. The Talos sits on its own concrete slab, separate from the foundations of the rest of the building to prevent everyday noise such as vibrations from foot traffic and doors closing from propagating into the system. The stage is also set upon a set of air legs which further reduce any noise from reaching the system. When at the highest magnifications, even sound waves from talking may affect image stabilisation, meaning care was taken to remain silent when imaging. The system is controlled by a computer placed several metres away to reduce disruptions during scanning. With these mechanisms in place the Talos provides stable imaging at high resolution with ease, allowing for overnight scans of EDS for full x-ray detection maps to show clearly.

Chapter 5: MiniMACS and SAS

This chapter reports the design of the MiniMACS system, and the results of experiments designed to calibrate the setup and understand the controllability of the Au NPs produced. It was also discovered that the system could be used without a matrix gas, to directly sputter the target material to create gold nanoparticles, in a mode called Single Atom Sputtering (SAS). This chapter will discuss the observations made when carrying out TEM on clusters produced in this way, their structures and NP aggregation. The results found are then compared to nanoparticles produced by previous groups using other methods that have been discussed in the Chapter 2.

5.1 MiniMACS and SAS

5.1.1 Design and Test

The MinMACS system was built by retrofitting a cold finger onto the preparation chamber for an Omicron VT STM/AFM. New components fitted included a thermally conductive but electrically isolated matrix support attached to a stainless-steel pipe (grade 310s24) that sits in the centre of the chamber. Fitted on to established ports, an evaporator and an ion gun were positioned to be pointed at the matrix support, ensuring optimum exposure during operation.

The chamber is a large cylindrical container made of high-grade stainless steel that has been engineered to create a highly controlled environment, with a view port installed to monitor correct positions of samples as well as monitoring correct functioning of instruments. For evaporator rate monitoring, a quartz crystal microbalance (QCM) was installed with a vacuum compatible bellows attached to allow movement in and out of the evaporator beam for precise measurement of the deposition rate, and then retracted as to not block any of the matrix support from the gold vapour. For the gas injection, a thin steel pipe was vacuum welded to a needle valve, designed to controllably bleed gas into the system without compromising the

other instruments as well as allowing control of the direction of the gas by bending the pipe. This allows a larger local pressure to be created, allowing faster matrix growth. The interior of the chamber is completely free of air and is maintained at a very low pressure using sophisticated vacuum pumps such as a turbomolecular pump to pull the chamber to very low pressures such at $1\text{x}10^{-8}$ mbar, backed by a rotary vane pump which handles the bulk of the air particles, from atmosphere down to $1\text{ x }10^{-3}$ mbar. These pressures are needed for both operation of the high-powered instruments without being ignited by the presence of oxygen, and for the path of the clusters to encounter as minimal scattering as possible, landing directly onto the sample.
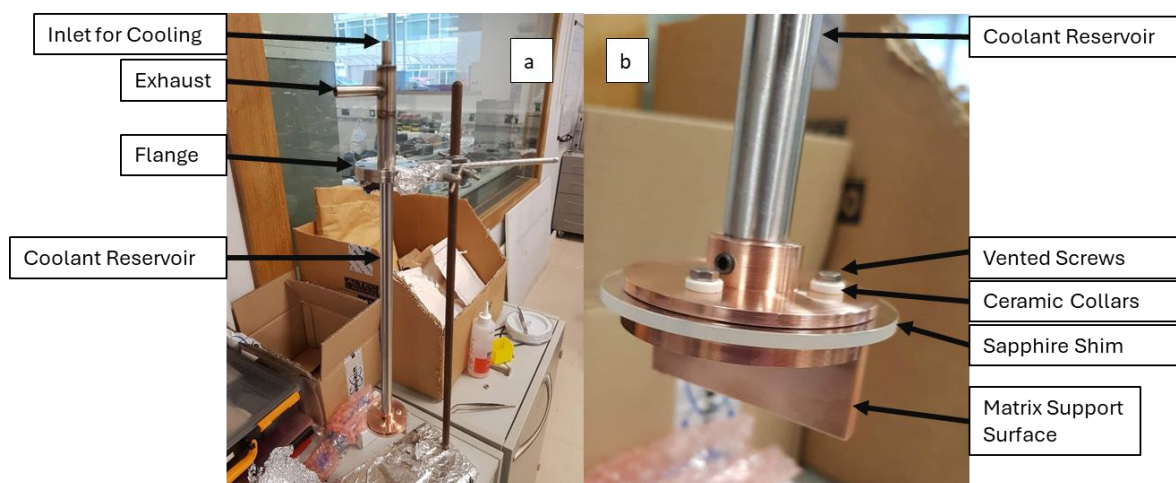
Figure 12: Photo of a) Cold finger assembly with exhaust to allow accelerated cooling and b) close of matrix support with a sapphire isolating plate

Figure 12 illustrates the design of the coldfinger, being vacuum compatible as well as thermally dissipating heat as effectively as possible. The matrix support was made from oxygen free high conductivity (OFHC) copper to ensure maximum transport of temperature. Separating the pipe and the matrix support is a thermally conductive, electrically isolating sapphire shim, coated in gold to maximise surface contact. The matrix support needs to be electrically isolated in order to measure the flux of the incoming ion beam. At the back of the matrix support sits a cable that runs through an electrical feedthrough which in turn leads to a multi-meter to ground. This allows precise reading of the ion beam. The screws are fastened with a ceramic collar to

keep the support isolated while securing the support block tightly to the sapphire shim. These vented screws are specifically designed to allow trapped air to be easily pumped through the bored hole in its centre. Without this, the pressure in the chamber would take a needlessly long time to pump down due to the slow release of the trapped gas, known as a virtual leak. A further provision was to silver solder the pipe to the vacuum flange in such a way that there was minimal surface contact with the rest of the system, increasing the lifetime of the poured liquid nitrogen. To measure the temperature of the support, a 4-pin Rhodium-Iron resistance temperature device (Rh-Fe RTD) was employed. A 4-probe system was used, in that a current of 1mA was passed through two of the pins, and voltage was measured, in turn resistance was calculated. A three point calibration curve was used as a reference to determine the temperature of the block.
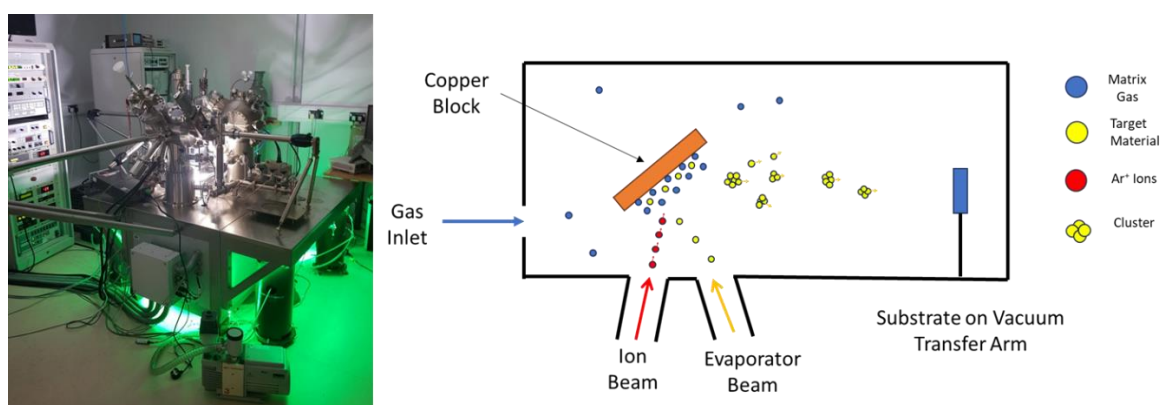

Figure 13: Photo of the cluster source, and schematic of the MiniMACS source from above, looking down. Underneath the copper block sits a QCM that is on a retractable bellows to avoid obstruction

A diagram showing the theory behind the Matrix Assembly Cluster Source (MiniMACS) is shown in Figure 13. The MiniMACS system is made up of a matrix support (copper block) welded onto a cooling system, making up the coldfinger, as shown in Figure 12. Liquid nitrogen is continuously poured into the pipe, until the Rh-Fe temperature sensor reads a voltage relating to a temperature of 77 K. Once cold enough, gas is supplied through the use of a needle valve for a steady pressure, to condense onto the matrix support surface. An e-beam evaporator is used to vaporise the target material while gas is condensing on the matrix support, creating a metal loaded gas matrix. A QCM is used to monitor the amount of material being vaporised, which sits close to the matrix support to get as accurate a reading as

possible. Once the matrix-metal has grown to a thick enough amount, the next step is initialising the cascade of collisions to facilitate growth of the cluster, and ejection of said cluster out of the cold gas. To do this, an ion gun is used, with collection of the clusters occurring with the use of the STM's manipulator arm acting as a sample mount. Initial calibration testing was carried out using a TEM copper mesh grid with a holey carbon thin film being used as a support material. The angle of the ion gun to the matrix support is 120°, and the angle of the matrix support to sample holder is 45˚. First, attempts at finding a suitable matrix gas was investigated, then before operation onto samples, initial calibration tests to observe the beam profile and position of the centre were carried to ensure best capture of ejected material.

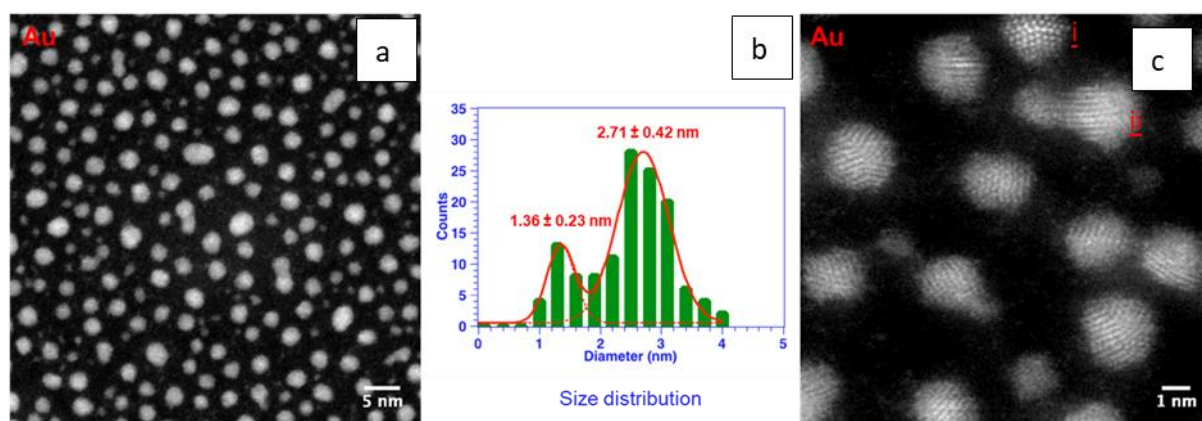**Testing the MiniMACS with CO$_2$**

Figure 14: a) STEM image of Au NPs on carbon TEM Grid b) Histogram of NP size distribution with red line imposed to illustrate bimodal peak and c) Close STEM image of Au NPs showing crystalline structure

Initial testing of the MiniMACS system with CO$_2$ as a matrix gas are shown in Figure 14. Dosing pressure of the CO$_2$ gas was 1 x 10^{-5} mbar with gold simultaneously evaporated for 40 minutes. Ion bombardment with a setup of 4 kV acceleration voltage and a flux of 30 μA for 10 minutes was initiated after the first step was completed. Substrate material was a holey carbon film on a copper TEM grid. Images were taken with HAADF-STEM to determine characteristics of the sample. There is clear evidence that clusters have been synthesised with a bimodal

distribution of sizes, with peaks at 1.36 nm and 2.71 nm. This is likely the feature of aggregation through Ostwald ripening, as discussed in the theory. One smaller cluster is atoms to a close larger cluster until a stable equilibrium is reached, leaving one small and one large cluster, hence the bimodal distribution. HAADF images taken by the Talos F200X show the crystalline structures of some of the particles, with clear order pertaining to decahedral in the case of the upper most cluster, and evidence of an FCC shape in the centre nanoparticle. In Figure 14 c), evidence of a decahedron can be seen in i), with the five-fold axis being very apparent, with also evidence of an aggregation event occurring in ii). The larger cluster of ii), the FCC structure looks to be influencing the smaller amorphous nanoparticle. Discussed further on, the image of one single snapshot in time is not enough to truly see the effect aggregation has on a nanoparticle's structure. Despite clear evidence of nanoparticles, further experiments were done to confirm that they were produced using the MACS method.
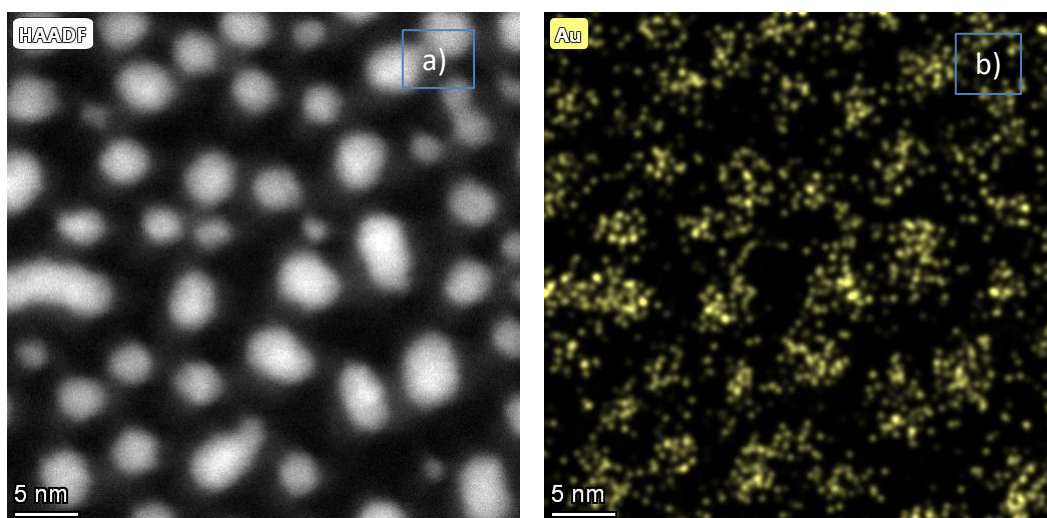

Figure 15: a) STEM image of Au nanoparticles without cooling the matrix support, and b) EDX of the sample confirming that gold nanoparticles are in fact being produced. There were no notable differences between the cooling and non-cooling of the support

Another test was carried out without the cooling of the support, with the resulting TEM image shown in Figure 15. Like before, CO_2 gas introduced into the chamber at a pressure of 1×10^{-5} mbar while gold was evaporated onto the surface of the copper block. The ion beam was kept at the same flux over the same amount of time.

To ensure that exposure time was kept as uniform as possible throughout these tests, the sample was rotated along the axis of the manipulator arm to shadow the sample instantly from exposure to the beam. Nanoparticles are still being synthesised despite not having a cold gas matrix to provide the environment for cluster growth. One explanation of nanoparticle growth could be attributed to the presence of the CO_2 gas acting as an energy sink/buffer gas to encourage gold-gold collisions, akin to a magnetron cluster source. However, due to no aggregation chamber, it is unlikely that this is the case. To test this hypothesis trials were carried out without CO_2 injected into the system.

Testing Without CO_2 (direct sputtering/Single Atom Sputtering method)
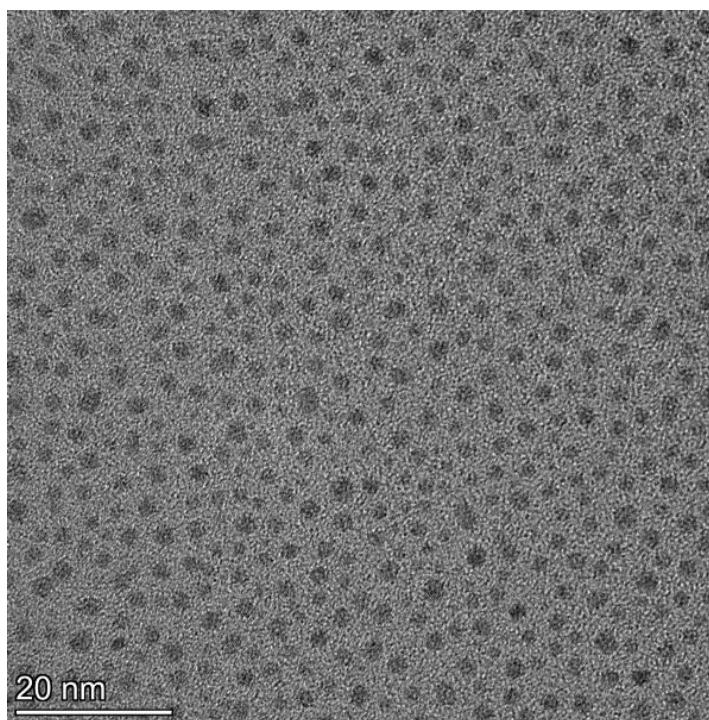

Figure 16: TEM image of Au clusters created without cooling and without CO_2 gas. Again, experiments show that the clusters are growing regardless of cooling or gas

Figure 16 shows a repeat of the experiment in Figure 14 but without the cooling of the support or introducing the CO_2 gas. Gold was evaporated directly onto the warm coldfinger. After this step, the evaporator was halted, and the ion beam was initiated with 4 kV acceleration voltage and 30 μA flux. After 15 minutes, ion beam bombardment was terminated. Bright Field (BF) TEM images shows once again the presence of clusters identical to that of experiments in figures 14 and 15 confirming

that the presence of CO_2 does not have any vital role to play in the forming of these nanoparticles. These clusters are most likely self-assembled on the surface through single atom – atom interactions, governed by one of three types of pre-thin film growth. Magnetron PVD incorporates the same fundamental physics as the Magnetron cluster source discussed earlier, but without any filtering/aggregation chamber to create thin films of material. Before a thin film of material is created, the growth can undergo one of three mechanics, Frank Van Der Merwe (FM) mode, Stranski-Krastanov (SK) mode, and Volmer-Weber (VW) mode. In FM, the adatoms attach themselves to the substrate surface and form a single layer, resulting in a two-dimensional growth mode. In SK mode, the adatoms form a layer on top of the substrate and then begin to form three-dimensional islands, resulting in a transition from two-dimensional to three-dimensional growth. VW mode dictates the adatoms initially form three-dimensional islands on the substrate surface, resulting in a purely three-dimensional growth mode. In the direct sputtering mode (now termed Single Atom Sputtering – SAS), is most likely the VW mode that dictates the growth.
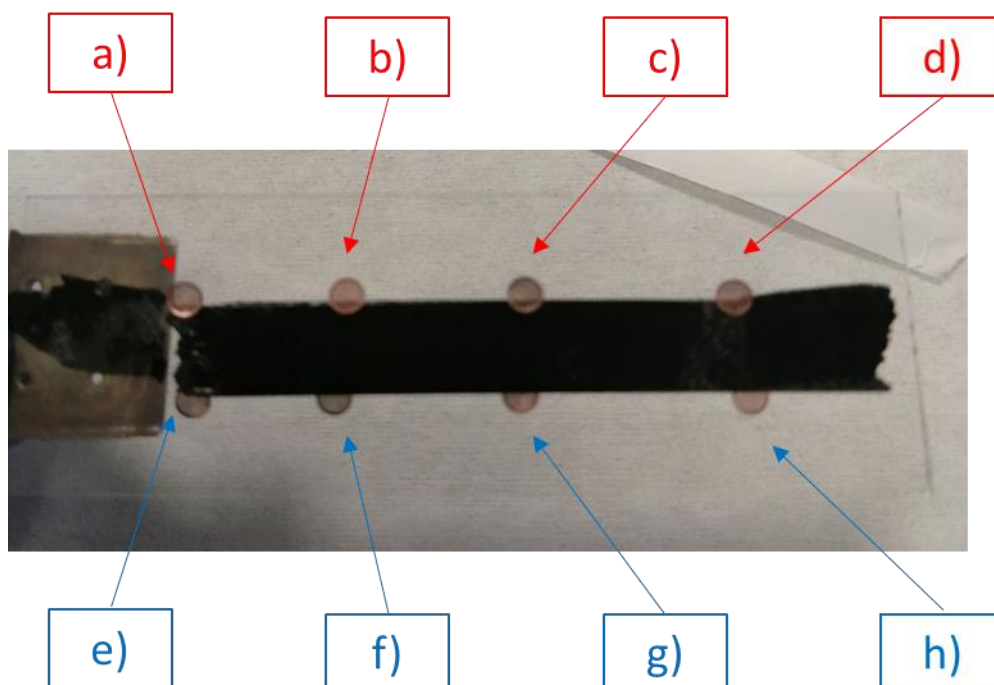
Testing with Butane

Figure 17: A) Photo of Carbon TEM grid mount on either side a glass slide support. Grid a) to d) (side 1) were used for direct sputtering, and grids e) to h) (side 2) used for MACS method with butane gas

The array of TEM grids in Figure 17 shows an attempt at trying to visualise the beam profile by first exposing the TEM grids to the different beams for a very brief time and then to calculate the coverage by surface on the resulting TEM images. A more suitable gas was chosen to be the matrix material in further investigations, this being butane, which has a higher temperature of freezing/sublimation in a vacuum compared to CO_2. Testing whether butane is a gas that will work, some control tests have to be carried out. An array of TEM grids that were secured to a glass slide with carbon sticky tape, shown Figure 17, which itself is secured onto the sample holder, were employed be exposed to a MACS cluster beam. Similarly, an array of TEM grids was placed in a parallel line on the back of the glass slide, rotationally symmetrical to the configuration on the top side to allow for only direct sputtering to occur (without the cold matrix gas). This allows for a direct comparison between the two types of cluster synthesis, limiting differences in variables due to positioning of the samples. First, direct sputtering of gold was attempted for 15 minutes of sputtering, with a beam of 5 kV acceleration voltage and a flux of 30 µA, then exposing the sample for 5 seconds. Secondly, the MACS method of cluster synthesis with cooled butane as a matrix material was attempted, with the same ion beam configuration sample exposure to the beam for 5 second. The intention of the very small exposure to the two types of beams allows for a direct comparison. If a large exposure time was used, agglomeration would be seen by both methods, rendering extreme difficulty in drawing any differences between the two methods. Short exposure ensures a large dispersion of single atoms/clusters which will not garner any significant aggregation events; thus, it should be seen that direct sputtering should show small clusters of <1nm to single atoms, and should the MACS method work, larger clusters will be viewed.

A more comprehensive look at the beam profile spread is investigated later in this chapter.
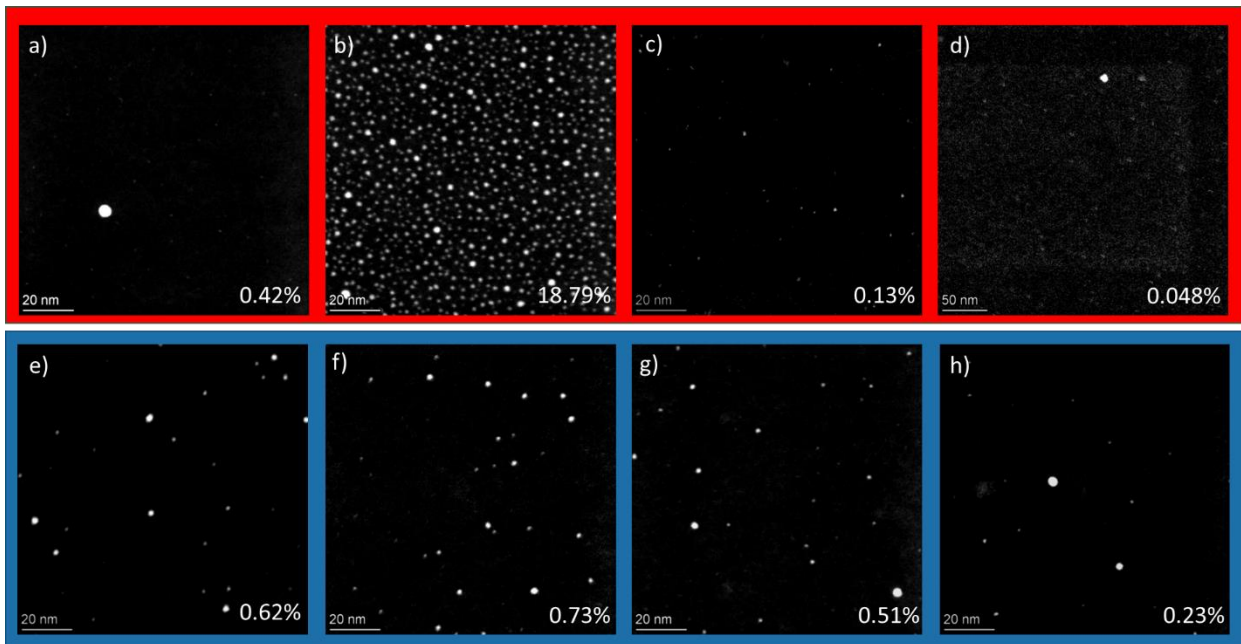
Figure 18: HAADF-STEM images of Au NPs synthesised using a) to d) direct sputtering method with position corresponding to Figure 18 a) – d), and e)-h) using butane method with position corresponding to grid placement in Figure 18 e) -h). Percent shows surface area coverage calculated using threshold mask on ImageJ.

The HAADF images of the TEM grids from both direct sputtering (shown in red) and clusters synthesised by a butane-based matrix gas (blue) have been compiled in Figure 18, in the position that is shown by Figure 17 [i.e. Figure 17 a) = position Figure 18a)]. Figure 18 a) and 18 e) have a very clear distinction in that Figure 18 a) has a surface area coverage of 0.42%, with one single cluster of around 5.75 nm and several very small, potentially single atoms. Figure 18 e) is in the same physical position, but has been exposed with the MACS beam, shows a clear distinction, with a surface coverage of 0.62%, majority in clusters of around 3 nm. The same can be said for comparing c) and g), as well as d) and h). c) and d) show small, barely visible clusters/scattered atoms, with the limits of what a TEM without aberration correction can detect, with d) having a similar single large cluster as a) at 8nm. The presence of this single cluster on a) and d) can be explained by a possible defect on the carbon surface. Images e) to h) show a presence of a larger clusters with a modicum of single atoms present. The only outlier is image b, which shows a large surface area coverage of 18.79%, with the bimodal distribution of sizes, resembling a

longer exposure to a beam such as one seen in Figure 16. This may be an outlier, or it may be the peak intensity of the beam. Considering the noticeable differences in a) - d) when compared with e) - h), it can be confidently concluded that butane does work as a matrix gas.

Figure 18 a) shows one large particle that overshadows small single atoms dispersed throughout the image, indicating that there is not enough material to create surface grown clusters. Figure 18 e) shows relatively large clusters that are a considerable enough distance from each other to have undergone very limited amount of aggregation, if none. Meaning that the clusters must have been synthesised before landing on the sample surface

Further work needs to be carried out, with repeat experiments to confirm both direct sputtering and MACS.
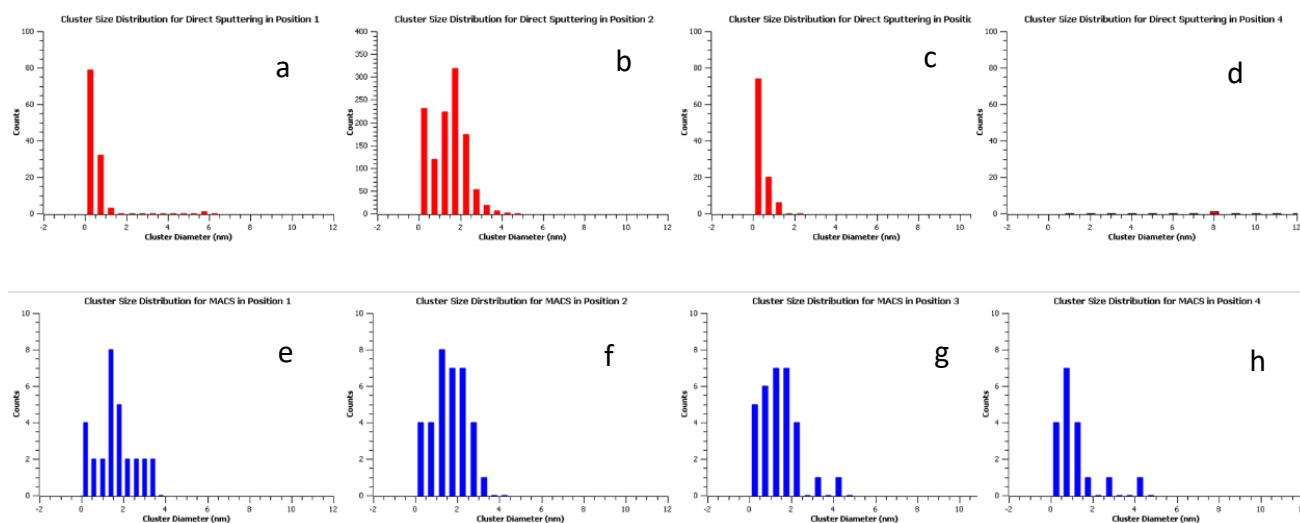

Figure 19: Histograms of the number of particles of Au (counts) vs diameter distribution, synthesised using a) - d) direct sputtering method with position corresponding to Figure 17. e)-h) used butane method with position corresponding to grid placement in Figure 17 and STEM images in Figure 18

To show that there is a clear difference between the two methods, histograms corresponding to the images seen in Figure 18 are shown in Figure 19. The overarching conclusion is that direct sputtering on a small-time frame will not be

able to produce enough material to be able to create sizable clusters on the surface or, has a very small beam profile that sits at position 2 on the sample holder. The MACS method can be seen to produce larger clusters at a lower frequency. From the preliminary tests, it can be inferred that clusters observed by direct sputtering (SAS) form on the surface through energetic movement of landed atoms. Energetically colliding with one another, single atoms aggregating to form surface grown clusters. While the MACS method shows to produce clusters before landing, so surface influence is minimal, meaning a more reliable fabrication method. These histograms reinforce the fact that there are two different types of mechanisms operating during synthesis. Demonstrating the potential versatility of the source, both modes of operation can be utilised with minimal modification of the source. SAS is a simpler, swift alternative to the MACS method, avoiding the cooling and building of a matrix which saves on time as well as complexity. There are several points to consider when choosing which method to use. A support material that has a high tendency to adhere will cause the atoms to potentially get stuck, building layer by layer (FM mode) with little to no clusters forming. In this situation a cluster created before landing is desirable, hence the MACS method is more suitable. Another situation is wanting similar size clusters but on two different materials. SAS methods may cause a different landscape which could cause a confirmation bias as to why one material may be more active than the other for example. MACS would once again be the superior choice in this instance as even if there were aggregation on the surface, most of the clusters will have formed beforehand and act as a foundation for any growth.

Due to the large number of times initial testing was carried out, a very thick layer of gold had been grown on the surface of the copper matrix support, thick enough to not worry about the ion beam milling through to the copper surface behind.

Going forward, any samples that have been prepared that used direct sputtering/SAS, had a gold foil target placed in front of the matrix support to completely minimise any worry of sputtering a large quantity of copper.

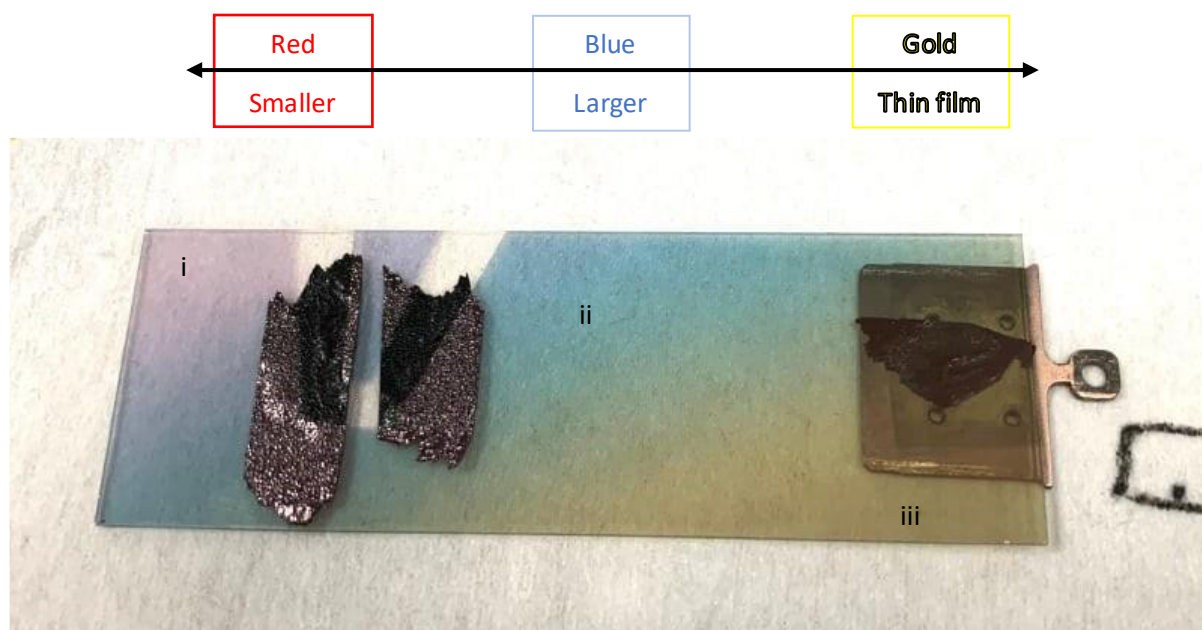**Testing of Beam position for SAS method**

Figure 20: Photo of glass after SAS deposition showing colour gradient relating to Au NPs size. The beam is not very well centred with respect to the slide, with the outer edges of the beam being at position i, and the inner being at position iii. Carbon sticky pads in between point i and point ii shows placement of where cursory samples for neuromorphic applications sat, described later in this thesis. The glass slide is secured with carbon tape on the STM holder to be positioned in front of the atom beam

Due to the SAS's method of cluster production being one continuous step, a glass slide can be used to find the position of the beam. Glass's transparency and the way nanoparticles interact with light mean that it is a suitable support for investigating the position of the beam. Figure 20 shows the slide after sputtering of the gold surface of the target material. The gold of the, highlighted in position iii, shows signs of a thin film/bulk gold forming rather than discreet nanoparticles. Moving further away from the gold area, position ii shows a gradual gradient that leads to a blue hue is observed. This implies that there are larger nanoparticles/island growth that is below the dispersion threshold to make a solid thin film. Continuing further away from the beam, position i shows a continuation of this gradient to a purple/red hue, implying smaller nanoparticles. This is due to a phenomenon called Localised Plasmon Surface Resonance (LPSR). Smaller cluster's electrons collectively oscillate at longer wavelengths, which corresponds to the red colour observed. Conversely, the larger the particle the shorter the wavelength and higher frequencies are observed, tending towards the blue wavelength of the visible spectrum. The shift

in plasmon resonance with size is due to density of the electrons in their energy states. The Pauli exclusion principle says that two electrons in the same state cannot occupy the same energy level. In this case, the more atoms are present, the more the energy levels must shift, causing a smaller and smaller space between the conduction electrons, leading smaller and smaller wavelengths. The converse is true with the discrete energy levels of the conduction electrons having more space the less of the electrons it "shares" a space with.

Figure 20 reveals that the beam has a very wide profile, not being very uniform. One advantage of this non-uniformity is the allowance for the synthesis of small particles. "Steady" growth of these clusters means that islands/percolating films aren't created unless more exposure time is given. Projects undertaken in this thesis and the relevant collaborative work has used samples that meant placement in the beam didn't matter as beam uniformity on a small scale is for all intents and purposes equally exposed. However, a disadvantage would be the need for a larger sample. Exposing it to this beam will cause a non-uniform coating. More experiments should be undertaken; by altering the incident ion beam angle and collection angle to see the effect this has on the atom beam profile. Focusing the beam by way of changing angle could mean a more efficient beam, reducing time of deposition further.

Using this technique to view the beam position has allowed future experiments to reduce the time taken to do one experiment from around 4 hours down to 15 minutes. This both increases efficiency, meaning more samples can be created in a day, as well as saves on instrument usage. Redeposition on the ion beam can be harmful to the gun due to shorting between electrical components, so this method of ascertaining the optimum sample positioning leads to increases the lifetime of expensive equipment.

The SAS technique has been employed on the larger MACS system by other users who have sought out an alternative to synthesising clusters. The SAS method in theory could sputter any target material that can be placed on the matrix support, which is angled towards the sample, demonstrating the versatility of these machines. When this new method was attempted, calibrating the beam was needed as an initial trial to work out if the beam position of MACS in comparison to SAS would be shifted. It is no use to look back at the SAS system and infer results to the MACS

chamber as there are too many differences to hope to account for such as ion beam power, pumping speeds, pressures, distance from ion beam to target material, distance from target material to sample, angle of incident beam etc. Users of the MACS have utilised the glass slide method of checking the placement of the beam by having an array of slides, confirming a quick, easy and time effective way to visualise the rough position of the beam without the need for TEM.

To take this further, Ultraviolet – Visible light spectroscopy (UV-VIS) could be carried on the glass slide to determine the cluster sizes by way of measuring the wavelength of light reflected by the clusters on the surface. Then this in turn reveals the cluster size.

5.1.2 Characterisation of SAS produced Au NPs

As mentioned before, the need to study the fundamental behaviours of gold nanoparticles is significant for prediction and control of sizes and shape, and thus explore and utilise them accordingly. Current techniques for characterising nanoparticle size distributions rely on limited static images, which may not fully represent the entire nanoparticle ensemble. This limitation restricts our understanding of size distribution and its impact on nanoparticle properties and behaviour. The objective of this research is to investigate a variety of nanoparticle sizes using a comprehensive collection of static images and develop robust methodologies for size and structural characterisation. This section of the thesis analyses several hundred nanoparticles with varying sizes and structures to determine any correlation. This work could be analogous to work carried out in astrophysics – observing other stars in the galaxy to get a broader understanding of its changing characteristics over time.
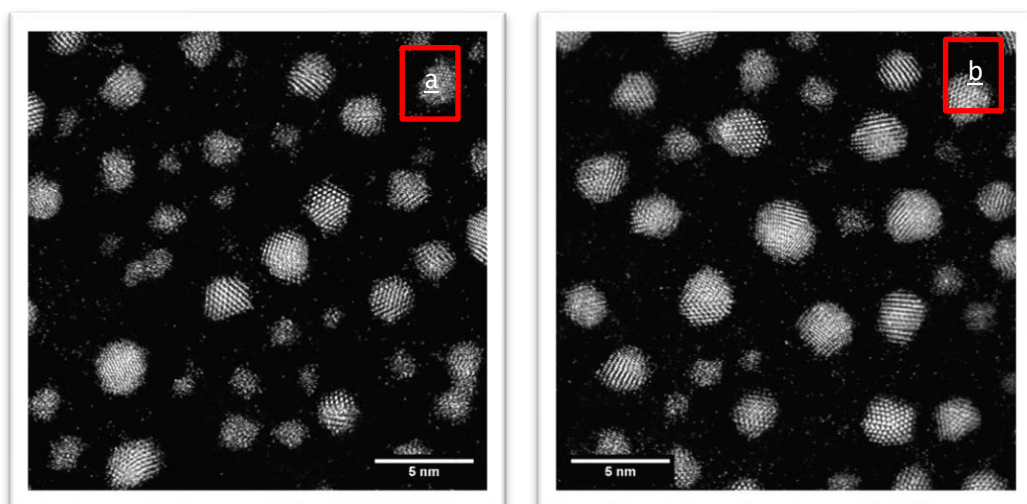
Figure 21 Aberration Corrected HAADF-STEM images of Au NPs synthesised using the SAS method with 4kV ion beam energy, demonstrating the different structures the particles can take

Figure 21 shows an aberration corrected HAADF-STEM images of gold nanoparticles grown on the surface from single atom sputtering from the SAS in two separate locations on an amorphous carbon coated TEM grid. The aberration correction of the JEOL ARM reveals detail that is eluded by other TEM's, such as the existence of single atoms that are free to move about the surface. The advantage of the SAS source is the ability to see a wide dispersion of sizes, even down to the single atom level. Exploiting this fact, along with the fact that the number of atoms in a cluster is linearly proportional to the intensity of the TEM signal that is generated, a size distribution analysis was carried out. First, a bandpass filter was used to filter out noise generated by the microscope. The filter used in the software specifies for larger and smaller features to be filtered, with the smaller filter being relevant to these images. A gaussian filter is used to smooth in Fourier space, and in these cases, either a pixel size of 1 or 2 was chosen to smooth. This is a vital step due to this experimentation pushing the limits of the microscope, with magnifications several million times over. This small-scale data analysis is highly sensitive to small fluctuations in signal. An average of ten or more single atom signals were collated to minimise the potential of using a dimer as a base reference, which would cause high compounding errors when calculating the number of atoms in a cluster. Due to the clusters sitting on a thin layer of carbon, a background subtraction is necessary to get as accurate an intensity reading as possible. Intensity readings are taken around the particle, with a second intensity reading being taken with a larger area but with great

care in making sure that these two areas do not overlap. After some manipulation, the real intensity is found. This is applied to every nanoparticle as well as single atoms. These steps were taken for each image, e.g., intensity of single atoms from Figure 21 a) was not used in finding the number of atoms a cluster has in Figure 21 b). From here, image contrast was enhanced to show more clearly the structure of each cluster. For each image, each cluster was numbered, analysed by number of atoms, and assigned one of several categories of structure. This was all tabulated to keep track of each cluster and its characteristics. A simulation atlas previously constructed of "magic number" clusters was used to cross reference each cluster in the HAADF-STEM image, corresponding to the closest matching atom number.

Bulk gold has an FCC unit cell crystal structure, which is one of the most common structures seen in metals, being the most efficient arrangement of packing atoms. However, as we move down to the nanoscale, an interesting phenomenon is seen where nanoparticles of gold do not always take this structure. Novel structures such as the ten sided or twenty sided shapes (decahedral and icosahedral respectively) are seen to occur.

There were several samples prepared using the SAS technique, by using an argon beam to sputter atoms off the surface of the gold target. A copper TEM grid coated with a holey carbon thin film was used to as a support and to facilitate nanoparticle growth. Investigation of the optimum exposure to create nanoparticles was undertaken using different accelerating voltages of the ion beam, ranging from 1kV to 5kV with a focus on keeping every other variable identical.
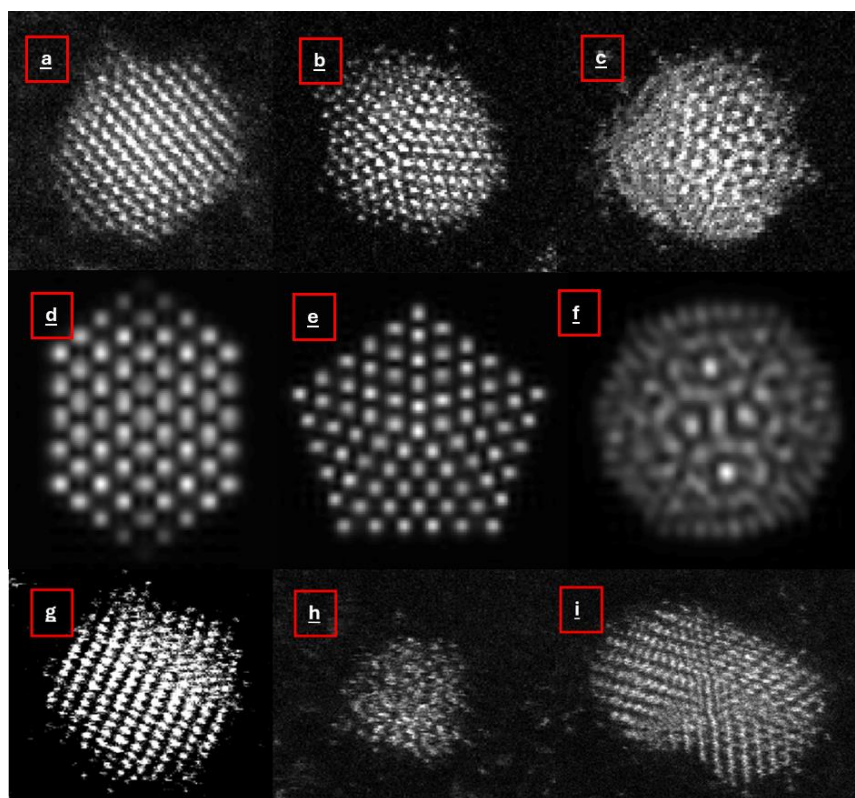
Figure 22: STEM images ideal of examples a) FFC, b) decahedral, c) is icosahedral, and their simulated counterparts d) simulated FCC, e) simulated decahedron, f) simulated icosahedron. Also, other examples of non-ideal clusters are shown with g) non-"ideal" FFC, h) unclassified and i) post aggregation Au NPs). All clusters are taken from various samples during these experiments, all were fabricated using the SAS method. The simulations were taken from the multislice method[154]

Figure 22 shows the three most clear examples of each shape found in gold nanoparticles of around 100-500 atoms in volume. These images are taken from the results seen in this chapter, from several different images of different samples. Figure 22 a) shows an FCC shape in the form of a cuboctahedron. One of the identifying features of the cuboctahedron is the 4-fold axis upon which two vertices of the triangular facets align with the two vertices of the square shaped facets. At orientation (0, 0) (with reference to the simulation atlas), this quadripoint can be seen after acclimatising to visualising the 3D structure. The five-fold axis demonstrated in Figure 22 b) is an exemplary instance of the decahedral shape, with the edges of the facets being more prominent than the other characteristics. The third and final significant shape explored in this work is an icosahedron, highlighted by the ring like structures seen in Figure 22 c). For these orientations it is obvious that these shapes

are all very distinct and can neatly be assigned. However as mentioned before, it is not always this easy to assign the clusters as these patterns are a lot more obvious to pick out compared to different orientations. Figure 22 d) shows another FCC, cuboctahedral structure that at first glance does not have a simulation counterpart. The four-fold axis can be observed, with difficulty, in the middle of the structure. The more disorganised region towards the top of the nanoparticle is not presented in any of the simulations, so this could either be a due to an orientation difference, or it may be that this nanoparticle's atomic sum will not produce a clean "full" cuboctahedron. Care must be taken when trying to visualise 3D structures when looking at nanoparticles as the image being seen on HAADF does not convey depth and wrong conclusions may be drawn. Figure 22 e) shows a glassy/amorphous nanoparticle that does not have any type of clear structure to it. While small ring features are present, current simulations primarily focus on magic number clusters. Simulating the growth of every type of nanoparticle, from a single atom to thousands of atoms, is currently not feasible due to the limitations of computing speeds as well as the vast amount of data generated would be overwhelming for human researchers to analyse.

Figure 22 f) is an example of what looks to be the start of island growth, whereby two nanoparticles of roughly the same size have coalesced to some degree. This is an example that demonstrates two crystal structures of the two nanoparticles rearranging themselves to align with each other, as demonstrated in previous work[154].
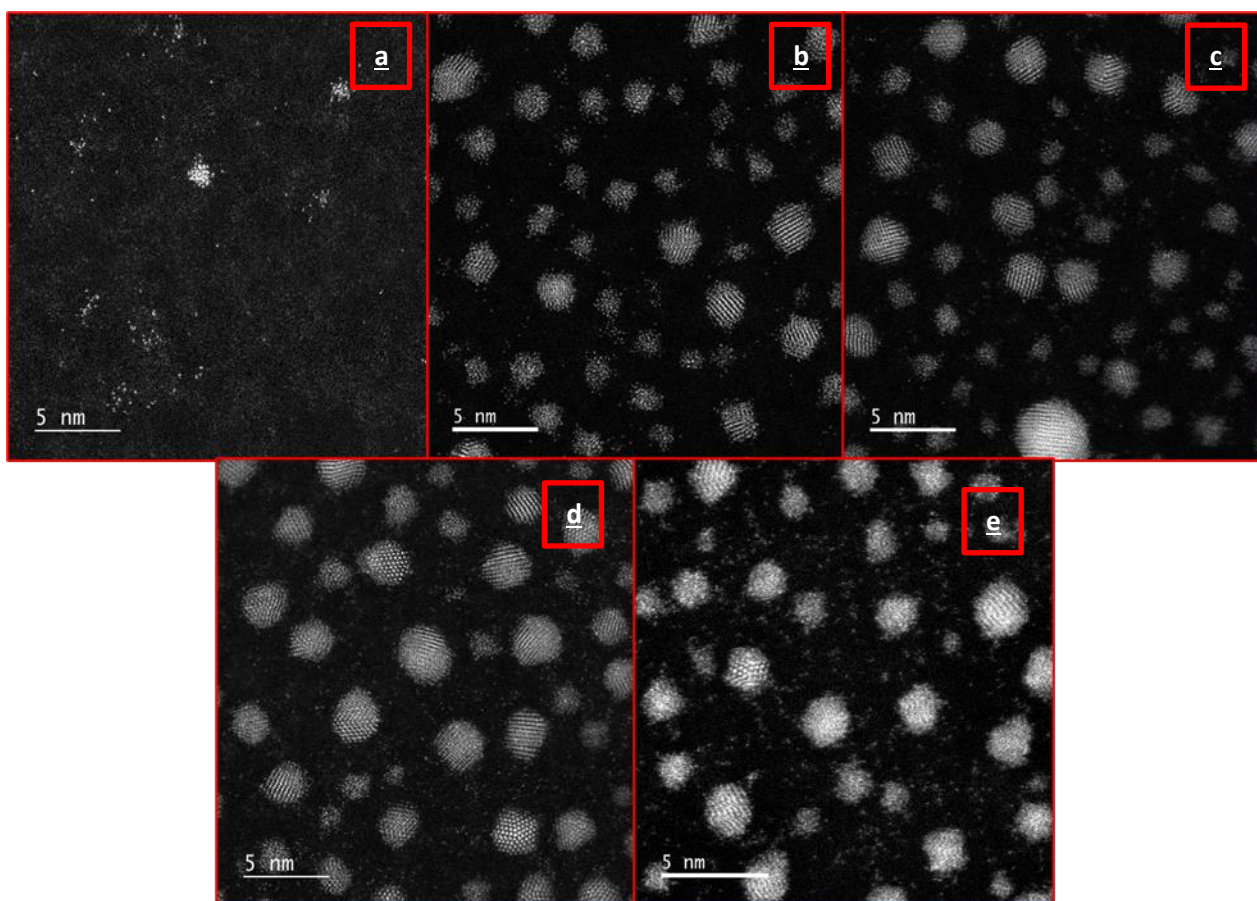
Figure 23: TEM images of SAS fabricated Au NPs, synthesised using ion acceleration of a) 1 kV, b) 2 kV, c) 3 kV, d) 4 kV and e) 5 kV

Five holey carbon film TEM girds, Figure 23, were all exposed to the SAS beam for 15 minutes with an incident flux of around 30μA each. Figure 23 a) – e) have all been exposed to the beam at 1kV, 2kV, 3kV, 4kV and 5kV respectively. All the images have been taken with an aberration corrected TEM, allowing the imaging and intensity normalisation of a single atom. All the images have been taken at a magnification of 8Mx, except for e) which was taken at 10Mx mag. Image a) shows a few clusters of tens of atoms around 1 nm or below, with several vivid scattered single atoms. Despite being around 1 nm in diameter, the clusters consist of less than 100 atoms. Comparing to the other similar sized clusters, they should comprise of a greater number of atoms. The amorphous nature of these small clusters suggests that there is no stable structure for them to reside. It has been suggested that these are the nucleation points of the larger clusters, forming a 2D "raft". Image b) shows a mix of sizes of clusters, being roughly 2 nm in diameter. There are signs of crystallinity in some of the larger clusters but still an amorphous majority in the smaller sizes.

Image c), d) and e) are each showing a lot more crystallographic examples, with FCC and Dh being displayed in abundance. There is a hint of a ring like structure on image c) suggesting part of an icosahedral structure, but is not identical to any of the orientations presented in the simulation atlas. Images d) and e) have an abundance of single atoms, but with e) having a greater number and a more intense signal, highlighted by the vivid brightness. This could indicate the atoms are in fact dimers or even trimers, meaning that there might be a threshold of cluster growth before new clusters start to build up. Analysis of beam exposure for ion gun acceleration voltages from 1-5kV shows that the prime range for cluster structural analysis is between 3kV and 5kV, with extra care being focused on the single atom reference at high voltages.
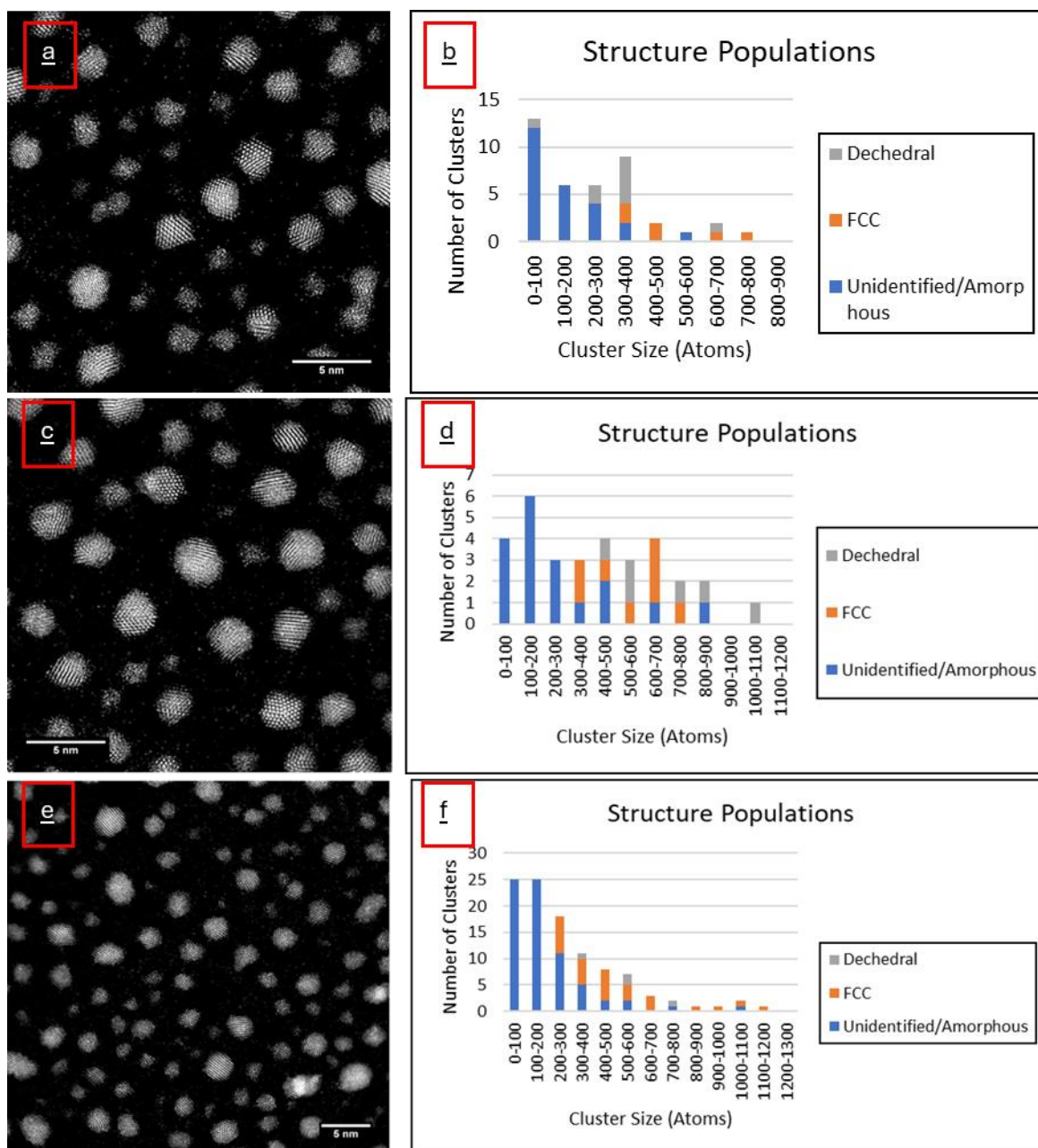
Figure 24 HAADF-STEM images of SAS synthesised Au NPs using 4kV ion acceleration voltage and their corresponding histogram of structure populations from three different areas of the sample

Figure 24 shows the structure populations frequency against number of atoms, to the corresponding STEM image. After a bandpass filter and background intensity subtraction has been applied, each cluster was sorted by number of atoms and referenced back to the simulation atlas. This way of organising the data can offer a clear way of discovering any trends that may be shown. From a cursory glance, smaller particles tend to have a glassy structure, not being able to settle into anything with stability. Out of 40 particles analysed in this image, nine where Dh, six were

FCC and 25 were amorphous, with amorphousness tending to the smaller particles, Dh to the relatively mid-sized range, and FCC being the preferred status of the larger nanostructures. However, 40 particles could be considered circumstantial evidence, so several hundred more clusters must be analysed before any conclusions can be drawn. As briefly touched upon in Figure 23 b), the smaller amorphous particles may be 2D in structure, creating these "rafts" of atoms, as some structure can be seen but not enough to confidently assign to one of the classifications. Potential simulations could be undertaken to explore this further and what causes the instability in smaller clusters as opposed to their larger counterparts.

Figure 24 d) also indicates that the dominant classification of the smaller clusters is of a glassy nature with decahedral being preferred mid-range and FCC being the preferred larger structure. This image has an exemplary example of a decahedral structure at orientation (0, 0), meaning that the atomic columns are aligned incidentally to the incoming electron beam. FCC structures are also quite populous in this instance with eight examples appearing, more than decahedral at six examples. Another brief observation is that there seems to be a threshold of around 300 atoms before any crystalline structure starts to emerge, which seems to be decahedral.

Looking at the overall trend of Figure 24 b), d) and f), it can been inferred that the incoming ion gun acceleration does not play a role in the structure of the clusters, only the amount of material that is sputtered off of the target material. 4 kV at 15 minutes exposure looks to be the most favourable conditions for structural isomer population analysis, allowing for both large enough clusters to exhibit crystalline structures, as well as being small enough to view single atoms for the intensity reference. The image of Figure 24 c) is an excellent example of the range of crystallographic geometries, by showcasing several 2D clusters, an obvious FCC and a very vivid decahedral shape as well as an abundance of single atoms to use as an intensity reference. Out of the 104 clusters imaged, 28 were FCC and four were Dh with FCC being the favourable structure at the lower end of the sizes.

As mentioned before, it takes a long time to characterise the shape of the clusters of even one image due to the need to post-process each image, label each cluster and

then refer to the simulation atlas. To overcome this problem, the analysis of gold particle structures conducted in this study holds significant potential for training a machine learning program to recognise and classify various nanoparticle structures. By systematically studying the diverse morphologies and crystallographic arrangements of gold nanoparticles, we can generate a comprehensive dataset of labelled images representing different particle structures, such as FCC lattices, decahedral shapes, and those of a glassy nature. This dataset can serve as a valuable resource for training a machine learning model, enabling it to learn and recognise the characteristic features and patterns associated with specific nanoparticle structures. The knowledge gained from this analysis will help establish a robust foundation for the machine learning program, enhancing its ability to accurately classify and identify nanoparticle structures in future TEM imaging experiments. Ultimately, this integration of machine learning with TEM analysis has the potential to automate the characterisation of nanoparticle structures, facilitating advancements in nanoscience research and applications. The need for manual analysis in place of purely computer classification is from the reality of structures of surface grown nanoparticles, less perfect than its simulated counterpart which computers struggle to identify.
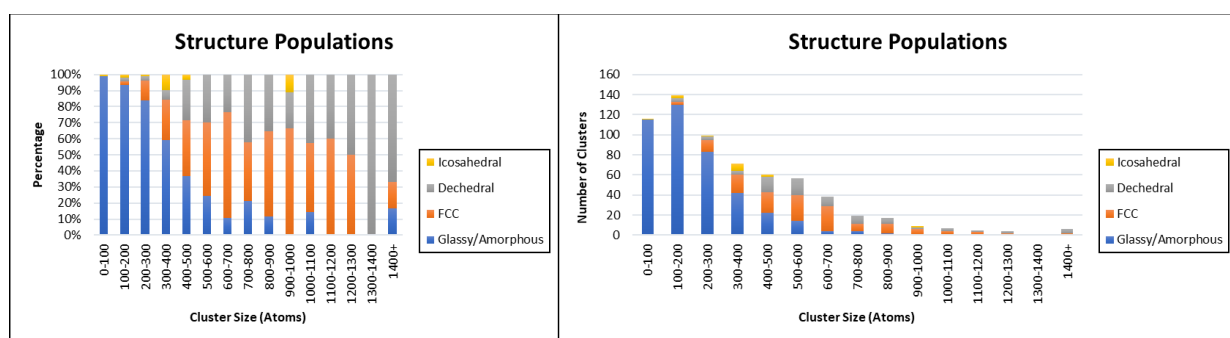

Figure 25 Graphs of accumulative structure populations of 648 measured Au NPs

It can clearly be seen in Figure 25 that there is an abundance of unstable smaller clusters, that are classified as glassy or amorphous. These clusters tend to be 2D in nature, with clusters showing around 70 atoms having a comparable diameter as a cluster of 400 atoms. It may be inferred that the growth mechanism of these clusters is a result of either VW or SK growth on a localised level, meaning that a small layer is constructed before incoming atoms come into contact and build out the bulk of the

nanoparticle. As the number of atoms increase, more stable structures can be seen, with FCC and decahedral competing for the more reliable structure. Increasing the number of atoms, FCC tends to be the more frequent structure which is in line with both previous work, and logical due to the bulk structure of gold being an FCC structure. Previous work with silver clusters has been undertaken in a similar vein. When comparing the two sets of data, it can be seen that decahedral structures are less common, with the two dominant features being that of FCC and icosahedral. Due to the inert nature of gold and easier time silver has of oxidising at a nanoparticle scale, it has been postured that the silver clusters tends to favour icosahedral structures rather than decahedral, due to the presence of oxygen in the air. Overall, 648 clusters were analysed with 418 being glassy/amorphous, 136 being FCC, 79 being Dh and 15 are Ih. Clusters below 300 atoms tend to prefer to remain glassy/amorphous, with the mid-range/larger clusters preferring either decahedral or FCC, with a skew towards the latter.

To build upon this analysis, three approaches are recommended. Firstly, a machine learning based program to quickly classify the structure of the clusters would enable huge amounts of data to be processed, getting a more reliable understanding of any trends/relationships that may be seen with cluster growth in this manner. This would also lead into the second recommendation to build on this experiment, the use of videos rather than snapshots of moments in time. As proven in the previous chapter, one cluster size may undergo several changes in its crystal structure. If the two methods were combined; machine learning characterisation and videos of several hundred clusters in frame at once, there would be enough data to dwarf that of what is found in this project. Separate from the machine learning aspect, a comprehensive investigation by size selecting clusters in increments of 100 atoms at a time to find any trends with regards to atom number thresholds that may occur. If there is a change of preference of structure then to repeat with a smaller scope of selectivity, moving in the range of 10's of atoms to find the transition points.

5.1.3 Real Time Au NP Aggregation

While characterising the cluster structural configurations, several videos were taken to view the structure changes under the electron beam in the TEM. One significant occurrence observed was a coalescence event between a small and large cluster. Understanding the behaviour of Au NPs in dynamic environments can be considered important for both fundamental scientific investigations on growth behaviour and practical applications. Aggregation of Au NPs is one such phenomenon that has interested researchers in recent years to understand fundamental behaviours. When Au NPs come into proximity, either through attractive forces or changes in their surrounding environment, they tend to aggregate forming larger clusters. These clusters can exhibit distinct optical[155], electronic[156], and mechanical properties[157], making them an intriguing subject of study.

While these techniques provide valuable insights into the morphology and structure of the aggregates, they often fail to capture the dynamic nature of the aggregation process. In other words, they offer a static perspective of a dynamic phenomenon. To overcome this limitation, this chapter presents a more in depth approach to study gold nanoparticle aggregation by capturing and analysing a video sequence of two gold nanoparticles during the process. This video-based technique allows us to observe and analyse the time dependant evolution of the aggregation event, providing a more comprehensive understanding of the dynamics involved. The whole video shows examples of all three classifications of structures of interest with regards to gold – decahedral, cuboctahedral and amorphous/glassy, both before and after aggregation. Frames from the video highlighting important events are shown in Figures 27.
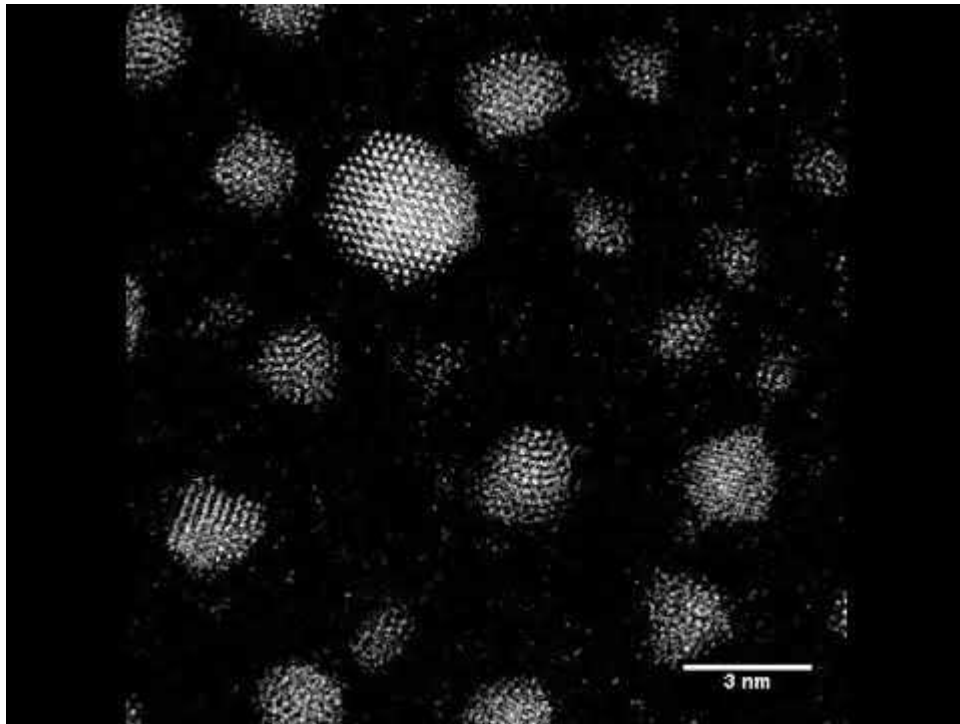
Figure 26: HAADF-STEM video of the coalescence event between a large and small nanoparticle of gold. The clusters of interest are two near the centre, highlighted in Figure 27
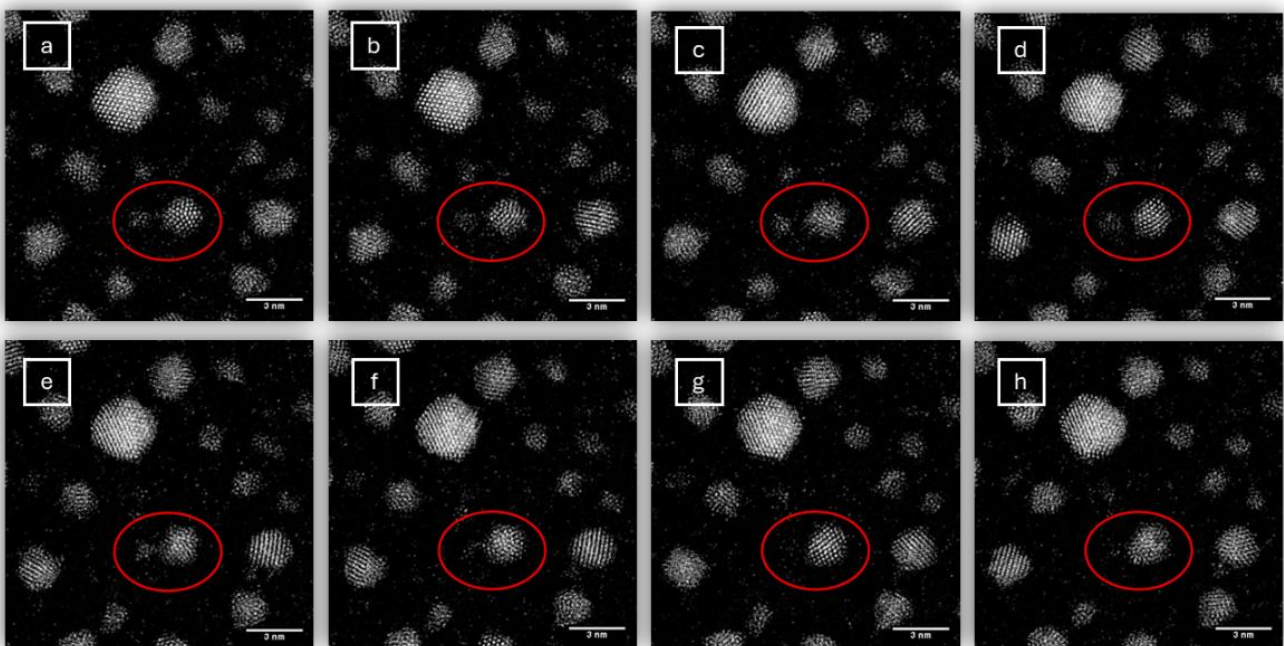

Figure 27: HAADF-STEM images from key frames of the coalescence video with a red circle highlighting the relevant two clusters. a) – e) shows the clusters before the aggregation event, and f) – g) shows after the event has finished. Several different structures are competing, with the dominant structure changing post aggregation

Figure 27 a) shows a snapshot of a video of gold nanoparticles, imaged using a JEOL ARM300CF aberration-corrected microscope which allows a high enough resolution to image single atoms. The sample was prepared using the SAS, with an argon ion beam energy of 5 kV, a beam flux of 60 µA, impinging on a gold target at 120 ˚ to the sample. The holey carbon grid was used as a support material as it shows a very high contrast with regards to atomic weight when compared with the target material, gold. The first snapshot, a), shows two nanoparticles, one containing 275 atoms, and the smaller 2D cluster containing around 75 atoms.

The larger of the two clusters has a decahedral shape when compared with the simulation atlas, whereas the smaller 2D cluster has an amorphous arrangement – meaning there is no stable shape for the cluster to settle at. The choice of these two clusters coincides with the ideal cluster size, or "magic number cluster" which is the number of atoms needed to create a full decahedral/icosahedral/FCC (cuboctahedral) shape. In this case, the coalescence event shows a transition from below to above the 309 magic number cluster.

The second snapshot in time, Figure 27 b), shows that a short time later the cluster is at a different orientation but still is categorised as a decahedral. The small fluctuations of number of atoms each particle has, can be explained by the surrounding single atoms being accumulated, and atoms in the cluster being ejected out by energy from the electron beam. This injection of energy by the incident electron beam is one of the predominant causes of structure fluctuation, the other being the number of free atoms coupling and decoupling as time passes. The HAADF image reveals the 2D cluster having a disordered arrangement throughout the video, suggesting a limited, or no prominent stable composition with a presence of voids and defects.

It could be argued that the larger structure changes from a normal decahedral to that of a truncated decahedral, evidenced by the ring-like structure where the 5-fold axis normally would converge to. Other novel structures that may fit in with some of the crystals seen throughout these images are Marks-truncated decahedral and Ino-truncated decahedral, which ultimately are classed under the decahedral banner but will have a similar but distinctive look to a complete decahedral.

After subsequent analysis, Figure 27 c) revealed a significant change in its structure. The HAADF image showed that the previously ordered and well-defined decahedral cluster had transitioned into an amorphous structure. This transformation was attributed to the influence of environmental factors, such as temperature from the electron beam, which can induce structural changes in nanomaterials. The amorphous structure of the gold nanoparticle was characterised using electron diffraction and atomic-resolution imaging techniques, which showed a disordered arrangement of atoms with no long-range order. These findings suggest that the properties of gold nanoparticles can be highly sensitive to external factors and emphasises the importance of understanding the structure-property relationships of nanomaterials. This study highlights the potential for HAADF-STEM imaging to provide valuable insights into the dynamic behaviour of nanomaterials under various conditions. Though some sort of order can be ascertained, such as a questionable truncated 5-fold axis, it is difficult to pair it with a counterpart from the simulation atlas. Overall, these findings underscore the need for continued research to fully understand the complex behaviour of nanomaterials and their potential applications in a variety of fields.

Subsequent analysis of the gold nanoparticle in the fourth snapshot, Figure 27 d) shows a change in its structure again, where the previously amorphous nanoparticle had transformed into an ordered FCC lattice structure. The HAADF-STEM image of the nanoparticle revealed a highly organized arrangement of atoms, indicative of a regular and well-defined crystal structure. The transformation from an amorphous to an ordered structure was attributed to, once again, the introduction of energy from the beam to the nanoparticle. It is important to remember that a single image of a nanoparticle is not as good as analysing a series of images of the same area because it provides a limited view of the nanoparticle's behaviour – a snapshot in time. Nanoparticles are complex and dynamic systems that can exhibit different properties and behaviours under different conditions. By only seeing a single image of a nanoparticle, we can miss important information about its shape, size, and behaviour, which can impact its properties and potential applications. Analysing a video can help us understand the nanoparticle's behaviour over time and provide a more

comprehensive view of its properties. This can help us design better nanoparticle-based materials and technologies that are more effective and efficient.

Figure 27 e) shows the beginning of the coalescence event, with both particles displaying an amorphous disorganisation (although the larger cluster does exhibit some limited order, either FCC or decahedral, it is not fully definite as to what the structure is). It is interesting to note that the largest cluster in the whole image of size >1000 atoms has remained stable throughout the video, displaying an FCC composition which suggests that a larger particle at this size is more stable in this configuration. This relates to the widely understood phenomenon that gold nanoparticles are known to exhibit an FCC structure, which is one of the most stable structures for metals. The stability of the FCC structure is due to the arrangement of the atoms, which maximizes the number of nearest neighbours and minimizes the surface energy of the nanoparticle. As gold nanoparticles grow larger, they tend to maintain their FCC structure due to the minimization of the surface energy as well as being the most efficient way to pack spherical atoms. This stability is evidenced in the video, where the gold nanoparticle remains in its FCC structure despite being under the high energy electron beam which is further supported by the fact that bulk gold has a unit cell of an FCC structure.

In can be seen the circled area in Figure 27 f), the larger cluster that has fully absorbed the smaller of the two, which is a clear example of Smoluchowski ripening. In this process, smaller nanoparticles break down, diffuses to the larger particles which in turn leads to its growth. While the cluster does exhibit some order, its structure does not match any examples in the simulation atlas, suggesting that it is amorphous. The exact arrangement of atoms within the cluster is not clear and may be a combination of different structures or a novel structure altogether. This highlights again the complexity and diversity of nanoparticle structures and behaviour. One explanation could be that the nanoparticle is at angle that does not match up with any orientation that is displayed in the simulation atlas. As the atlas has been produced and referenced select iterations of angles, there could an orientation that fits more precisely.

Figure 27 g) shows the gold cluster which has recently absorbed a smaller cluster has increased its size beyond the threshold of magic number of 309 atoms. The cluster appears to be stable, retaining its FCC structure. The individual gold atoms within the cluster are arranged in a closely packed manner, forming a lattice structure with a high degree of symmetry. The surface of the cluster is uniform, with little visible defects or irregularities. The image provides valuable insights into the behaviour of gold clusters at the nanoscale and highlights a potential link to the magic numbers in determining their stability and properties. By absorbing the smaller cluster, the larger gold cluster in the TEM image has exceeded this critical size but has retained its FCC structure. This suggests that the stability of the cluster is not solely determined by the number of atoms but is also influenced by other factors such as the arrangement of atoms and the strength of interatomic interactions.

Finally, Figure 27 h) shows that even though FCC has become the dominant stable crystal structure, it does not mean it is not also subject to becoming amorphous. Once again, some sort of order can be glimmered from the HAADF image, but it does not match any orientation in the simulation atlas. Ring like structures akin to the one exhibited could signal icosahedral configuration, but due to the erratic nature of the edges, it cannot be confirmed one way or another. Consider a surface energy vs time graph, each minima is considered a stable structure. However, there are pockets of local minima where the configuration of the crystal structure is briefly stable, but any small jump in energy (induced by the electron beam) could be enough to overcome the threshold and change structure, also known as a metastable structure. This could be evidence of metastability, a semi-defined orientation of atoms that do not fit conventional shapes.

The total video length is 1.3 seconds with 500 frames taken, meaning each frame is 2.6 milliseconds.
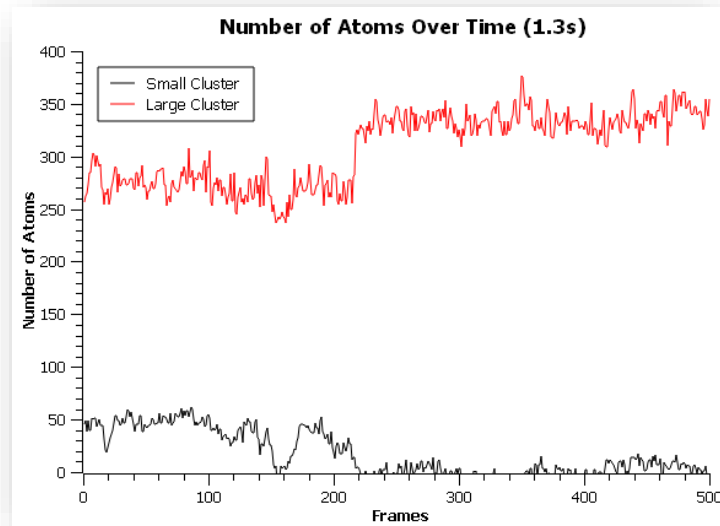
Figure 28: Graph of evolution number of atoms in large cluster (red line) and small cluster (black line) with time

Figure 28 shows the number of atoms as a function of time – in this case it's the frames. The red line shows the larger cluster hovering around 250 – 275 atoms, before the coalescence event. It can be seen that the full coalescence occurs at frame 210, seeing a jump from about 275 atoms to 325 atoms. The converse is true for the smaller particle, whereby the at frame 210, there is a downward jump of 25 atoms. The discrepancy of the addition to the number of atoms of the larger cluster and the number from the smaller cluster may be attributed to the fact that as the larger one grew, several other atoms around the cluster may have been caught in the cluster's influence and absorbed. This also explains the noise that can be seen on both graphs, with stray single atoms venturing in and out of the measurement area.
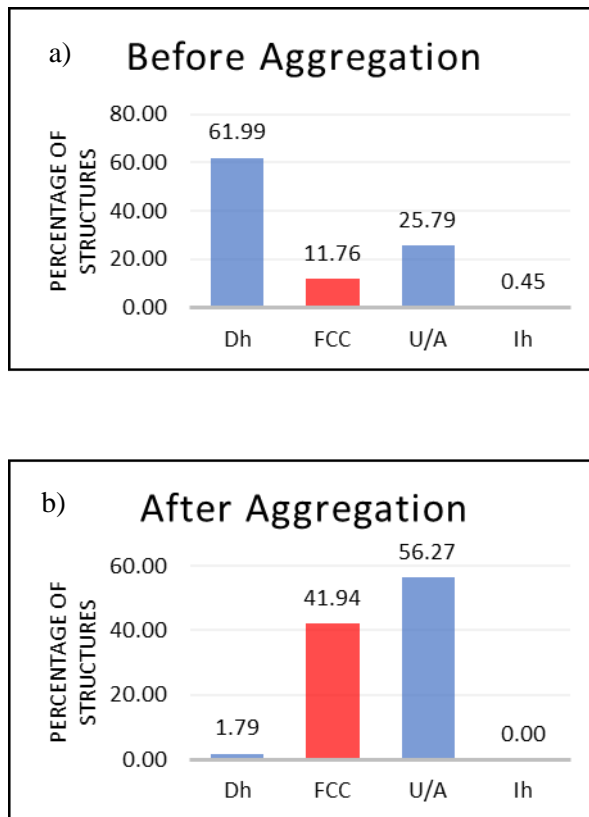
Figure 29: Graphs of percentage structures Decahedral (Dh), Face Centre Cubic (FCC), Unclassified/ Amorphous (U/A) and Icosahedral (Ih) a) before and b) after aggregation

It can be seen in Figure 29 before the coalescence event, the predominant stable structure is the decahedral configuration, at 61.99% frequency whereas the FCC structure was much lower at 11.76%. The unidentified/amorphous structures had a 25.79% occurrence, higher than that of FCC, suggesting that this particle size favours decahedral and will occasionally settle as FCC. Only a few frames displayed the icosahedral shape at 0.45% occurrence. After aggregation, decahedral reduced drastically to 1.79% yet the FCC structure increased to 41.94%, suggesting a change of adequate stability regarding structure. One interesting point to note is that the predominant "structure" is the unidentified/amorphous category, at a 56.27% frequency, suggesting that the structure itself is less stable than before. Icosahedral did not appear at all, which is reinforced by the fact that the gold clusters at this size tend not to exhibit icosahedral structures. It is worth noting that all this data occurs within 1.3 seconds, with 0.546 seconds passing before the coalescence event, and

0.754 seconds passing until the end of the video/characterisation. To reinforce a common theme in this thesis, despite it being a viable way to analyse cluster structure, single frames of nanoparticles show only a snapshot in time of the structure and stability of the cluster. An analysis of videos with frames over a period of time will gleam a narrow but a more comprehensive understanding of the cluster in question. Not to say that single images taken separately doesn't have its benefits, as the analysis of them allows clusters of varying sizes to be analysed and grouped into brackets. Organising like this satisfies a broader look at the data that may prove fruitful to investigate if there is a correlative trend between groups of atomic size clusters.

5.1.2 Conclusion

One of the aims of this thesis is to create a method to produce Au NP that has a high yield as well as being environmentally friendly. As discussed in Chapter 2, CO_2 at liquid helium temperatures can be used as a matrix gas and produce Au NPs with diameter of <3 nm. Here a MiniMACS system was designed and built, with initial testing on CO_2 matrix gas to prove the concept that Au NPs could be produced with diameters of <3nm. However, running the system without CO_2 lead to the discovery of the SAS method of NP synthesis. It is inconclusive is the CO_2 can be used a matrix gas at liquid nitrogen temperatures, as testing ceased for a more suitable gas. Further testing with butane gas has shown that a matrix can be formed at liquid nitrogen temperatures and can produce Au NPs, comparable to that of previous MACS clusters of <3nm. This shows a proof of concept that Au NPs do not have to be synthesised at liquid He temperatures, allowing for both in energy efficiency and a more accessible instrument as liquid nitrogen is readily available in most lab environments.

The SAS method produced Au NPs which were characterised using a JOEL ARM aberration-corrected TEM at Diamond Light Source, and an analysis was carried out to the structural populations. It was found that small clusters, (below 300-400 atoms) have no majority stable configurations while the mid to larger clusters were decahedral or FFC structurally dominated.

Work also discussed in this chapter using Au NPs synthesised using the SAS method and an aberration corrected TEM, has shown the process of NP aggregation and the transition from stable decahedral to an unstable FFC structure.

It has been shown that the MiniMACS is a suitable method for Au NP synthesis, however, its yields are comparatively small due to its relatively small beam profile from the ion gun, and the small surface that the matrix can form on. Chapter 6 discusses an investigation into scale up potential using a MACS system and while using different metal-based NPs. The SAS technique has also been employed by users of the MACS machine as a simple, easy to use method for fabricating clusters on a large scale with ease, alongside MACS made clusters. Widespread investigation onto different surfaces for SAS methods compared to MACS methods could be carried out to better understand the role the support has in surface assembled clusters and the difference they may have catalytically when compared to clusters formed in flight.

Investigations into the coalescence events around other magic number clusters could be carried out, potentially using size selected, mass filtered clusters to get a nanoparticle that is just below the size threshold. Then size select smaller clusters onto the same sample and study any aggregation event that could occur. Under the TEM beam, there most likely will be a cluster pairing like the one observed in the video in this chapter. This could be studied for all different magic number clusters.

Chapter 6: MACS Scale Up to Application

This chapter reports the results of experiments to calibrate a MACS system for larger volume production of silver nanoparticles (Ag NPs) for catalysis, and lead nanoparticles (Pb NPs) for water purification.

6.1 Calibration of the MACS

In recent years, there has been an escalating demand for clusters in various fields, ranging from materials science to catalysis and biomedicine. Clusters, defined as nanoscale assemblies comprising of a few to several hundred atoms, possess unique properties that differ from both bulk materials and individual atoms. These properties make clusters promising candidates for numerous applications, including energy storage, sensing technologies, and advanced electronic devices. However, the practical production of clusters on an industrial scale has remained a significant challenge, often limited by the trade-off between production efficiency and environmental impact. The Matrix Assembly Cluster Source (MACS) emerges as a breakthrough technique that addresses the challenges and paves the way for large-scale cluster production without compromising environmental sustainability. The MACS works by cryocooling a copper matrix support to liquid helium temperatures, wherein an inert gas is introduced into the system, adsorbing onto the cold surface. Simultaneously the target material is evaporated through the use of a thermal evaporator and captured by the gas. Achieving the optimum metal loading percentage in the matrix is crucial for the MACS to work precisely, as too high a loading will achieve an amalgamation of trapped gas in a target matrix which will then be sputtered akin to the SAS method. A key feature of MACS lies in its ability to initiate cluster aggregation through the bombardment of argon ions in the cold gas. This process enables the clusters to assemble and grow prior to surface landing, negating any surface influences that would otherwise inhibit growth. Furthermore, this barrage of energy is sufficient to eject the cluster out of the matrix onto an awaiting sample. One of the most significant advantages of the MACS is its minimal environmental impact. By employing physical methods, the need for ligands is

negated, thus none of the harmful chemicals that are used in colloidal production to remove them. Additionally, the number of clusters being ejected out of the matrix is linearly proportional to the incident ion beam flux, meaning the more ions bombarding the matrix, the more clusters are ejected onto the sample. This combination of environmentally friendly practices and potential to scale up makes MACS an appealing solution for sustainable and scalable cluster production. Where the MiniMACS was a demonstration of the technique using smaller components with readily available cooling, the MACS has a larger ion gun (both in size of beam and ion flux), a larger surface area of the matrix support, a cooling system to get down to lower temperatures, and a larger sample collection area. This is to produce a very efficient, scaled up version of the technique. In this chapter, the aim is to explore the principles and operational details of the Matrix Assembly Cluster Source (MACS) technique and assess its potential for achieving industrial-scale cluster production while maintaining minimal environmental impact. Several practical applications of using the MACS were demonstrated, with both attempts at energy production and catalytic activity being investigated. The gaining of valuable insights was anticipated through a comprehensive analysis of MACS produced clusters, with its practical applications and its role in shaping the future of cluster-based technologies.

Figure 30: i) Photo of MACS sample stage with TEM grids attached at various positions A-E. ii) MACS beam alignment distribution showing percentage coverage by surface area in each position

Figure 30 shows the rotating deposition stage, used to house samples during deposition, holding several TEM grids placed at significant points in the stage which are fixed by carbon sticky tape. The TEM grids are copper mesh with a thin layer of holey carbon to act as a support material to allow analysis in the TEM. The graph shows the percentage coverage by surface area. Position "E" shows the point of highest coverage by surface area when the stage is fully inserted, directly below the matrix support, showing 5.82% coverage. Assuming a symmetrical drop off the beam flux, the significant drop from point "E" to point "A" in contrast to the relatively slight drop off from point "E" to point "C" suggests that the peak of the beam for this configuration of ion beam energies is between the positions "C" and "E". Positions "D" and "B" are very similar in coverage, implying that the alignment of the beam in the x direction is optimal.
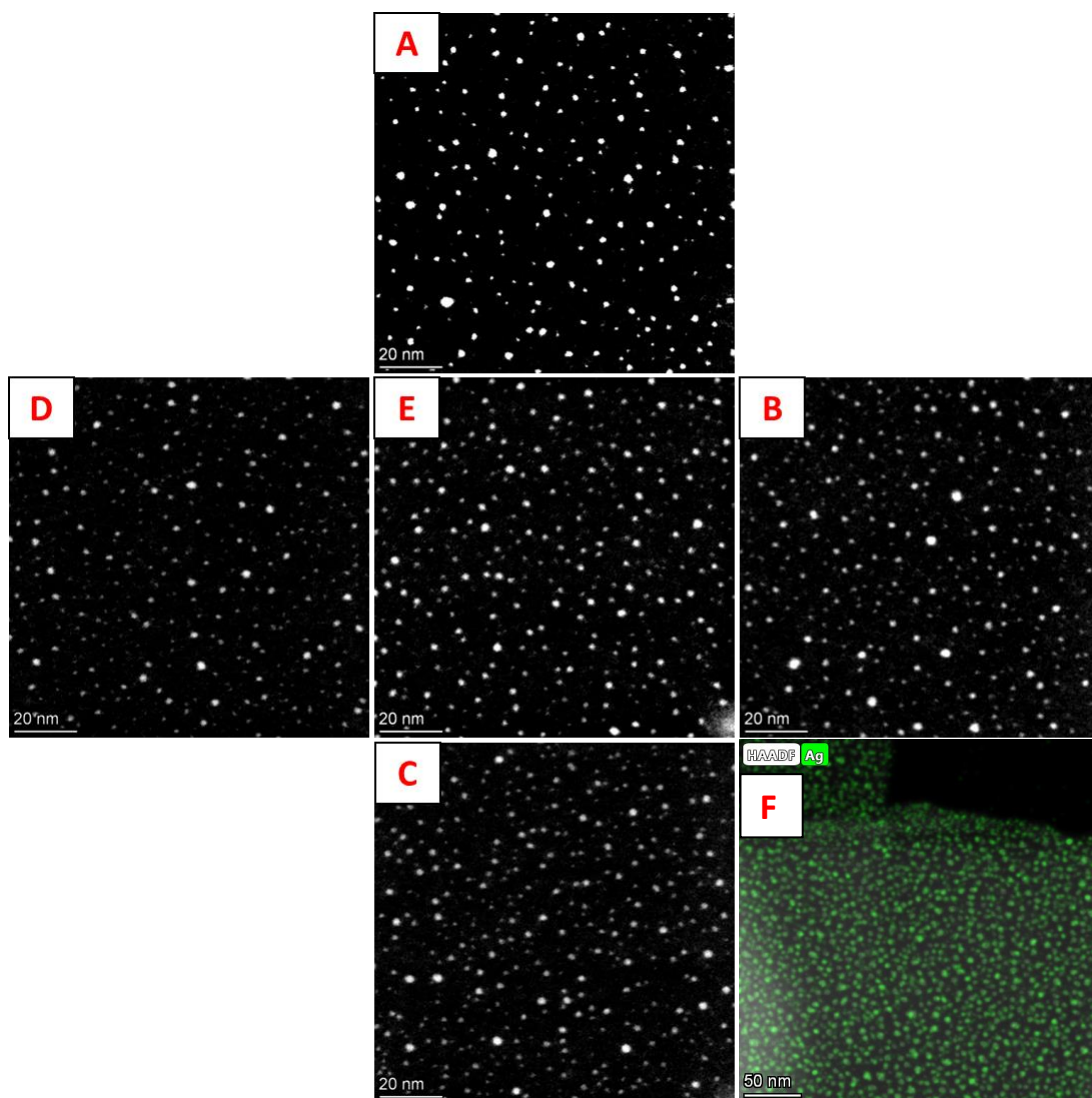
Figure 31: HAADF-STEM images from TEM grids in position A-E from Figure 30 i), and F is the EDX confirming the presence of silver (Note, F is not in any spatial configuration with regards to Figure 30)

Figure 31 shows the HAADF images of the TEM grids in Figure 30 after exposure to the beam. The silver clusters that are seen here were taken by the Talos F200X TEM using STEM imaging. The collection angle for the HAADF detector produces images on a greyscale, interpreting a higher deflection with a brighter image. Lighter features can be caused by either a denser material, a thicker material, or a heavier element. To increase the contrast of the nanoparticles and to minimise the supporting material's effect on the image, a suitable TEM grid coating was chosen to support the clusters. Holey carbon was chosen as a support material due to the large difference in atomic weight, with carbon having an atomic weight of 6 and silver

having 47. The carbon thin film is below 50 nm which also reduces the interference it causes.

It can be seen that there is a bimodal distribution of sizes. This is most likely due to Ostwald Ripening, whereby smaller cluster's atoms are donated to a nearby larger cluster until the distance between them is sufficient, so much so that there is no effect on them, leaving behind two prominent peaks of cluster sizes.

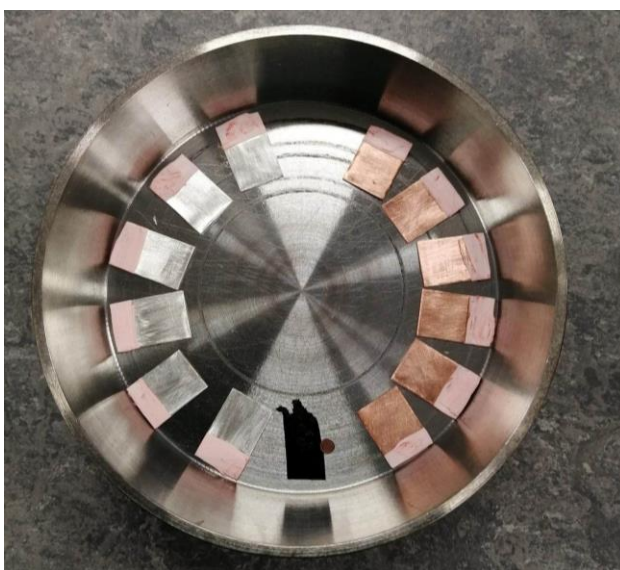## 6.2 Silver Cluster Synthesis for use as an Electrocatalyst

Figure 32: Photo of copper and silver foils attached to MACS samples plate, with a TEM grid placed alongside

With the calibration completed, a recipe was devised to deposit silver clusters onto metal foil to be utilised for electrocatalysis with the copper and silver foils arranged on the sample stage show in Figure 32.

A matrix was built with 4% loading for the initial step, then an argon ion beam bombardment was initialised with 500 V extraction voltage, and a flux of 10 mA. During deposition, the stage was continually rotated to ensure a uniform coating across the different samples, with the TEM grid placed in line with the copper foils. This allows for a good characterisation of the clusters on the foils. A TEM grid is needed as the copper and silver foils are too thick to be used under TEM directly.

When one side of the foils were coated, the foils were removed from the chamber and rotated to expose the uncoated side of the foil. The TEM grid was removed, and a fresh grid was placed in the same position as the previous one. The coldfinger was left to be warmed up to allow the argon ice to desorb off the support to make way for a new matrix with the same parameters as the previous time. This was to try and maximise uniformity of coating from one side to the other.
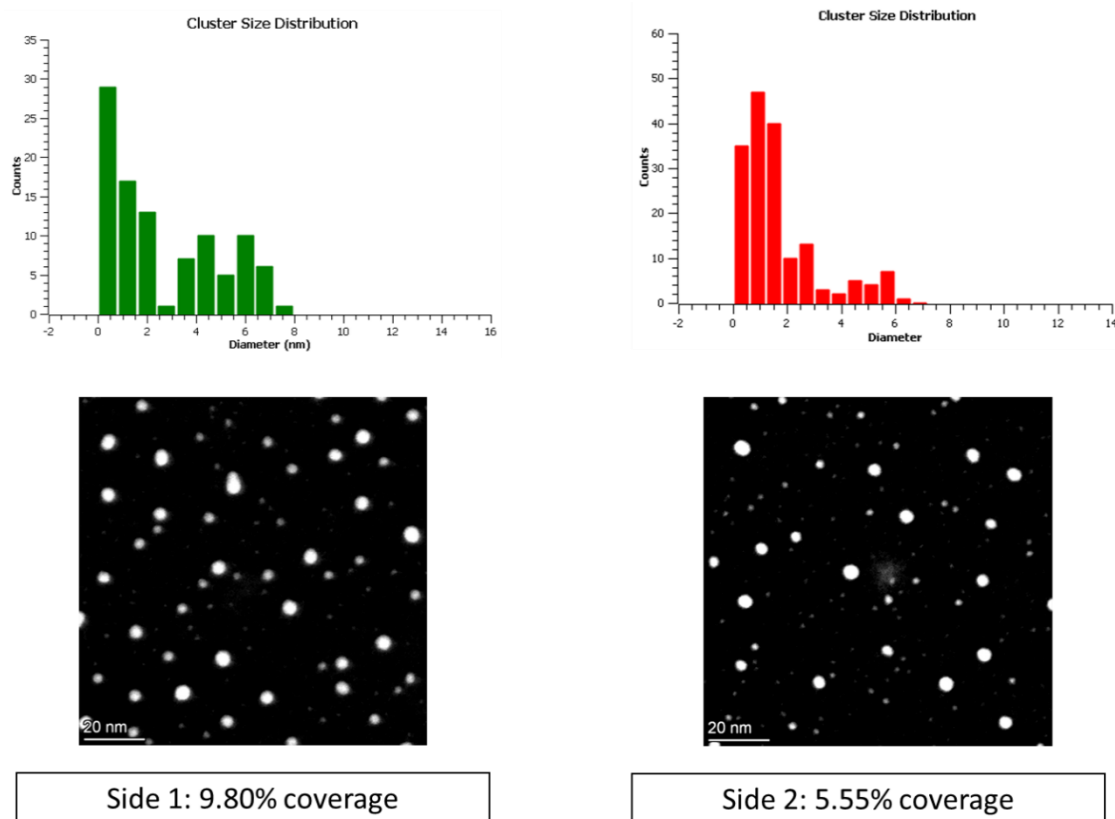

Side 1: 9.80% coverage

Side 2: 5.55% coverage

Figure 33: Histogram of size distribute of Ag NPs on a) side 1 and b) side 2 of MACS sample with corresponding STEM images

The TEM grid mounted on side one (Figure 33) has a 9.80% Ag NP coverage by surface area with a bimodal (possibly trimodal) distribution of sizes, peaking at between 0 nm and 1 nm and a peak at a larger size at around 6 nm. The modal bin size is 0-0.5 nm which is due to two potential factors: Ostwald Ripening whereby several smaller clusters may donate to a singular larger cluster, or the Matrix Assembled method of cluster synthesis is not 100% efficient in creating clusters before landing on the surface, i.e. sputtering out a substantial number of single atoms also trapped in the matrix, whereby they grow clusters on the surface of the sample.

Figure 33 shows a lower coverage at 5.55% for side 2, a decrease of 0.57% compared to side 1. This is unknown as to why, but potentially it could be unstable evaporation readings on the QCM during matrix building caused by the evaporator, which in turn causes an uneven density of metal inside the matrix. During sputtering, it may require more energy to sputter the matrix in denser points, or conversely there may be less material to sputter in the first place.

On both sides of the foils, there is a step down in frequency from 4 nm to 5 nm, and a step back up to 6 nm. This could be due to a 5 nm cluster being less stable than 4 nm or 6 nm diameter clusters.

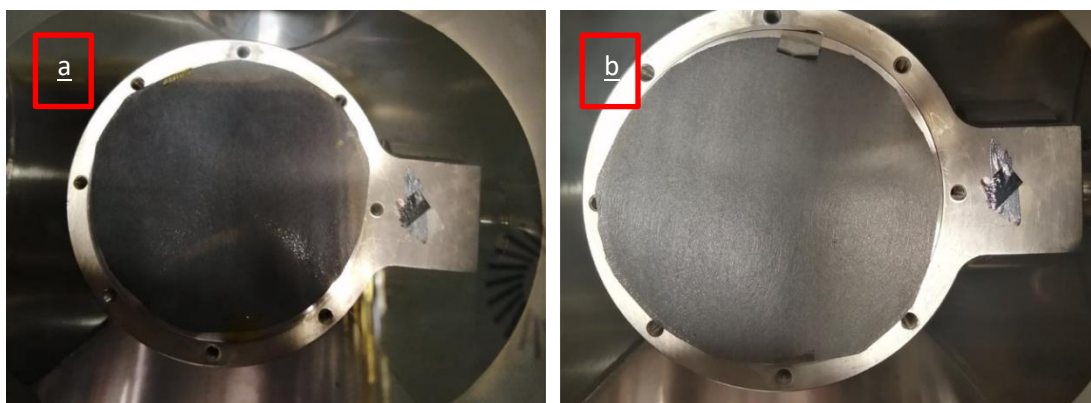## 6.3 MACS Clusters for use in Water Purification Methods

Figure 34: Photo of a) carbon paper 1 and b) carbon paper 2 on MACS sample stage

Due to the increased surface area caused by the porosity of the carbon paper as shown in Figure 34, a lot more catalyst material is needed to be able to coat as fully as possible meaning a TEM grid will not be a sufficient way to analyse the clusters after depositing. To overcome this, a quartz crystal microbalance was used to measure the clusters deposition over time. In conjunction, a small area of the coated paper was placed in liquid nitrogen, snapped, and placed into the TEM for further analysis to the status of the clusters.

As the carbon paper was large and fragile, there was a tendency for it to snap if too much bending occurred. Great care was taken to place them directly onto the stage rather than in the sample holder. From here, when deposition was in effect, the

sample was systematically rotated between clockwise then anticlockwise to attempt to coat areas that were potentially shadowed from the beam if the sample was static. A possible improvement on this technique could be to coat the back side of each of the carbon paper, dispersing the coating more evenly throughout the paper. A bespoke roll-to-roll appendage that has been designed for the MACS would be useful for not only coating more material but could in theory be adjusted in design to have the opposing track which sits (parallel underneath the exposed track), skewed so it exposed the back of the paper simultaneously.
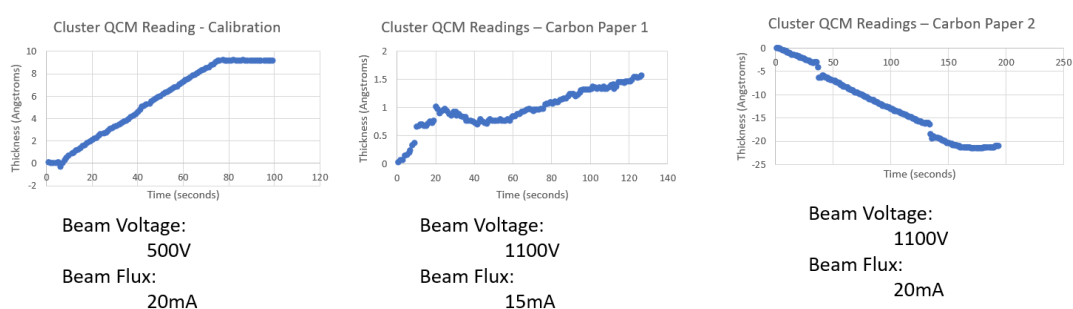

Figure 35: Graphs of Quartz Crystal Microbalance during deposition of Pb NPs

Figure 35 shows the QCM data of cluster deposition of three synthesis events, one calibration to determine flux, and two carbon paper depositions. Before a deposition on a piece of carbon paper could take place, calibration of the beam needed to be undertaken in order to create a suitable recipe. It was assumed that the lead beam would have a similar profile to that of silver, which meant that positioning of the sample was to be the same as the silver recipe. After a matrix of lead trapped in solid argon was built, a QCM was moved into place (several cm above position "A" from Figure 30) and thickness of material was measured for roughly a minute. With an extraction voltage of 500 V, a beam flux of 20 mA, there was a deposition of around 9 Å/min.

The same procedure was then repeated for the second carbon paper. There is a large discrepancy with the calibration graph and the carbon paper graph. This is because the calibration graph was based on a matrix that was grown for about 30 seconds,

whereas the setup for carbon paper 1 had a matrix grown for 294.8 minutes. From casual observation, the evaporator was not stable all the time, possibly due to higher-than-normal pressure arisen from the very thick solid argon gas on the surface of support (resulting in higher-than-normal sublimation rates. Another explanation could be due to the amount of material in the crucible changing over time, as lead a lot of lead was needed in the crucible to enable sufficient quantities to cover the carbon paper. The QCM was fully extended and recorded the initial ion beam bombardment. From 0-20 seconds we can see a steeper incline than the more stable 20+ seconds. This could be due to the initial impact of the ions on the matrix causing a larger than average influx of material to land on the QCM, before settling down to a more stable rate. Carbon paper 2 had an even larger amount of energy given to the ions bombarding the matrix, with a 1100V and 20mA being the maximum the ion gun is stable at in the presence of excess argon. There is an odd occurrence with the QCM from carbon paper 2 in that the thickness of the film seemed to be going in a negative direction. This is most likely a programming error with the software, as the QCM was still displaying sensitivity when it was retracted, as demonstrated by the plateauing of the graph at about 160 seconds, meaning that the inverse of the x axis made more sense. A lot more material was deposited onto this sample when compared with carbon paper 1, demonstrated by the brownish off-colour that was observed after deposition.

Table 1 a): Table of deposition rate of Pb clusters produced from the MACS from readings of the QCM, b) industry research and development target data for Pt loading for fuel cell technology, courtesy of the US Department of Energy (DOE)[158]

		mg/hour - 10cm Diam plate	Amount per cm^2 per hour
a	Calibration	3.838819946	0.048877374
	Carbon Paper 1	1.447875941	0.018434929
	Carbon Paper 2	4.396319627	0.05597568

		2017 Auto System	2020 Auto System	2025 Auto System (High Innovation)
b	Stack Power Density @ Rated Power (mW/cm² active area)	1,095 PtCo/HSC-e after derating to match ANL-optimized stack operating conditions	1,165 Based on PtCo/HSC-f after stack derating	1,500 Consistent with DOE 2020 target of 1,000 at 150kPa abs
	Total Pt loading (mgPt/cm² total area)	0.125	0.125 DOE 2020 target	0.088 Reasonable improv. over 2020 target

The amount of deposited material by weight by time is shown in Table 1a). By taking the diameter of the plate (and carbon paper) to be 10 cm and using the peak of

the material deposited (position "A"), it was worked out that the maximum potential material deposited was carbon paper 2 with a deposition weight of 4.40mg of lead clusters per hour. Then by normalising this to area (specifically square centimetres), we get 0.056 mg/cm2/hr deposition rate.

A note on production rates for the MACS. This experiment demonstrates the MACS's ability to create clusters in a physical method at a rate of 0.056 mg/cm2 per hour.

According to the United States Department Of Energy, the fuel cell industry has a target to create fuel cells as a proof of concept, that only need a platinum loading of 0.088 mg/cm2 to be able to function. Research and development on a new type of fuel cell is for now a proof of concept. This target is only 1.6x higher than the hourly rate shown by the carbon paper 2 attempt, meaning the MACS method may be a viable approach to generating platinum coatings on fuel cells. As mentioned previously, the MACS method produces particles that are ligand free, meaning not only are they more pure than chemical methods of cluster synthesis, but also no harmful chemical process is needed to make the clusters active which aligns with the environmentally friendly conventions the MACS represents. With improved gas phase cluster synthesis, there is potential to become very competitive in this lucrative market. With the ever-increasing awareness of humanity's emissive impact, it is important to reduce waste/harmful material in designing green systems that could negate any green progress the final device makes. Colloidal samples need certain chemicals to remove the aforementioned ligands which on an industrial scale is not a desirable side effect. Also, no process of removal is going to be 100% efficient, so more colloids will inevitably need more material to be as active than pure platinum created through the gas phase.
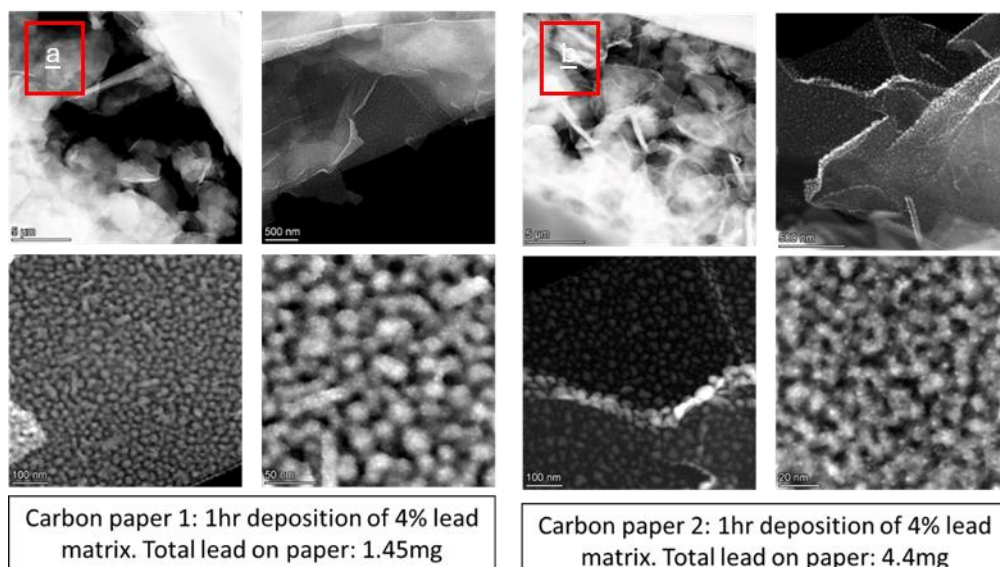
Figure 36: STEM images of Pb NPs fibres from a) carbon paper 1 and b) carbon paper 2 with c) showing a low magnification EDX map of carbon paper 1, showing quite uniform dispersion of clusters on the fibre, potentially preferring to sit along the edge of the fibre. d) shows a high magnification of the lead clusters with a spectra confirming the elements

The HAADF images in Figure 36 show the coating of lead nanoparticles. Due to the thickness of the carbon fibres, TEM mode was used at a low mag to locate a thin area such as a frayed strand to allow the beam of electrons to pass through, then imaged in STEM mode at a much higher magnification. EDX shows the lead particles to be coated mostly evenly across the fibre, with slight preference to rest at the edges of the fibre. The appearance of copper on the spectrum is caused from a secondary signal produced from the brass single tilt holder used in this case.
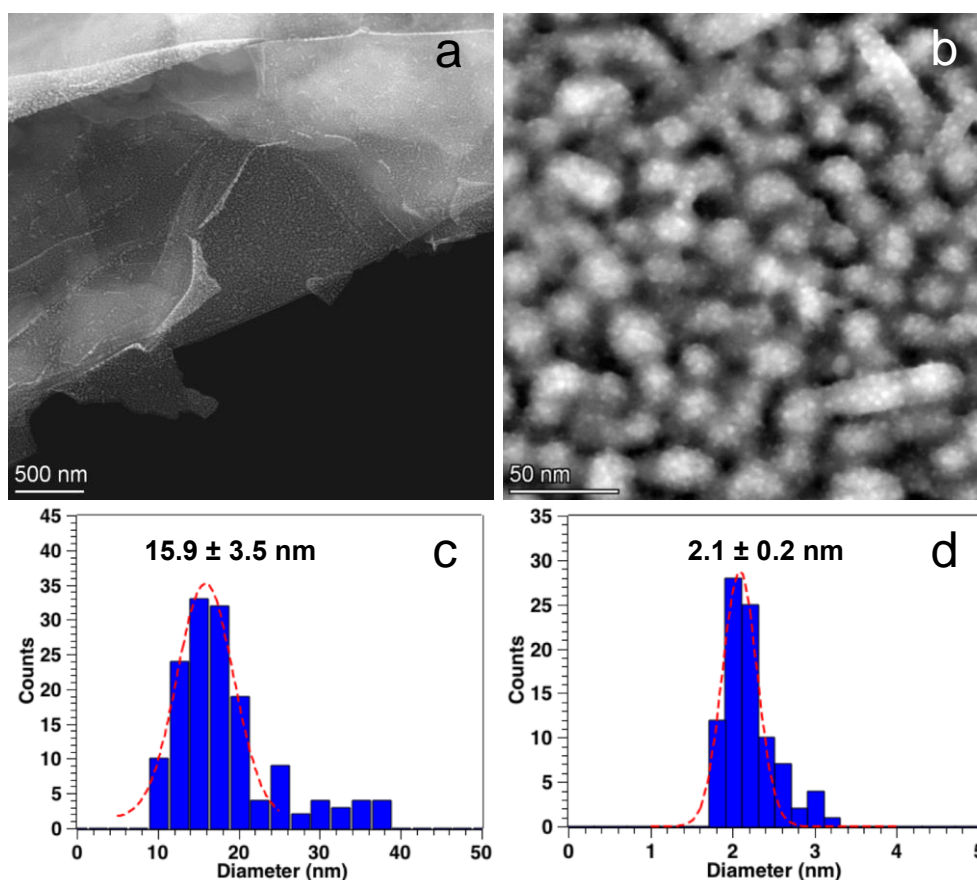
Figure 37: TEM images of Pb NPs on a) fibre and b) on carbon nanostructure and c) and d) are the corresponding size distribution histograms

In this study, Pb clusters, Figure 37, with an average diameter of approximately 2 nm were synthesized using the MACS technique and subsequently deposited into porous carbon paper (C-paper). Both STEM and SEM investigations, along with EDX mapping, provide strong evidence of successful Pb cluster deposition, resulting in the formation of the nanocomposite Pb-C paper system. The EDX analysis indicates that the Pb clusters penetrated the carbon paper to a depth comparable to the pore size, approximately 50 μm. To assess its performance, the Pb-C paper was employed as an electrode for electrochemical generation in an electrochemical flow cell reactor. Initially, the Pb-C paper exhibited activity; however, it eventually deactivated after approximately 10 seconds due to the dissolution of Pb clusters into the electrolyte. Moving forward, further research will be necessary to address the adhesion and anchoring of the clusters to the host material's fibres. Notably, this study demonstrates a technique for presenting a high surface area host material to an

intense directed beam of sub-10 nm clusters. The method involves only a few steps and holds promise as a competitive alternative to chemical approaches.

6.4 Conclusion

Upscaling production is an important step in achieving environmentally friendly nanoparticles for industrial applications. It has been shown in Chapter 6 that is it possible to take the MiniMACS method discussed in Chapter 5, and upscale production using a MACS method as well as demonstrating versatility of target material. Here, silver nanoparticles have been synthesised on a large scale for electro-catalysis although the catalysis research has not been reported in detail as it is beyond the scope of this thesis. Also, lead nanoparticles have also been produced for water purification using the MACS method on a scale about 50% required by current industries R&D targets, proving that scale up of the MACS method is possible. However, further development is needed in this area. Lead clusters were used for their properties to create highly reactive oxygen species (ROS) such as hydrogen peroxide and ozone, which in turn removes organic pollutants[159]. In environmental situations, lead contamination may give way to increased ROS, affecting the natural world[160]. Here, Pb clusters were used to increase surface area to utilise these ROS to purify water. The Pb-C paper exhibited initial activity but deactivated within 10 seconds due to the dissolution of Pb clusters into the electrolyte. Future research should focus on improving the adhesion and anchoring of these clusters to the fibres of the host material. Importantly, this study has demonstrated a technique for exposing a high surface area host material to a concentrated beam of sub-10-nm clusters. This method is simple and could potentially rival chemical approaches.

 Another potential use for NPs in is the developing field of neuromorphics and Chapter 7 reports of results from investigation into using Au NPs produced using the SAS method to form networks below the percolation threshold.

This instrument - heavy thesis has presented several results which should be further studied. It has been shown that the MACS method can be used to produce not only Au NPs but also Ag and Pb NPs. These NPs have been used in collaboration with groups for catalytic and water purification experiments. Further work is needed to further incorporate these particles into devices and to produce a large variety of nanoparticles including bi-metallic and tri-metallic so that their unique properties can be utilised.

It was seen that with a few tweaks, included larger chamber, larger ion gun, larger ion beam flux and larger sample collection, the MACS system is a scaled-up version of the MiniMACS. The lead nanoparticle production rates showed that the method reaches roughly 50% of current industry R&D targets. Not only is further development needed to optimise any more scale up, but cross disciplinary feasibility and strategic business planning is need calculate cost and viability.

Chapter 7: NPs for Neuromorphics

This chapter reports on a series of experiments relating to the use of Au NPs synthesised using the SAS discussed in Chapter 5 to form a film just below the point of percolation to mimic a neuromorphic network. As this is a developing field the chapter starts with a discussion of Moore's Law and how neuromorphic style-networks could be a possible alternative to this.

In recent years, the field of computer architecture has been facing a formidable challenge: the eventual end of Moore's Law. For over five decades, the semiconductor industry has adhered to Moore's Law, which postulates a doubling of the number of transistors on integrated circuits approximately every two years. This exponential growth in computing power has fuelled the rapid advancement of technology. It has become completely intertwined with the world's economy and revolutionised various domains, from personal computing to artificial intelligence. However, as transistors continue to shrink, they approach physical limitations and encounter significant technological, economic, and political obstacles. Consequently, researchers and engineers are compelled to explore alternative computing architectures that can sustain the relentless demand for increased computational capabilities. One such architecture that has gained considerable attention is neuromorphic computing.
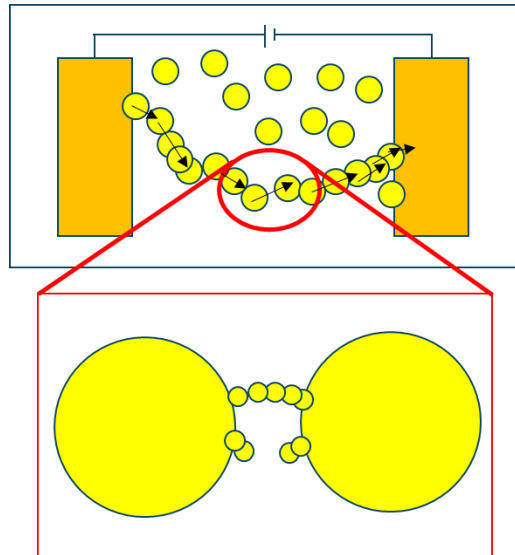
Figure 38: A close look at filament formation between clusters. Below the percolation threshold, filament growth is induced by placing a bias across the two contacts

Neuromorphic computing involves the creating of an alternative architecture to conventional computing. Current architecture for computing relies on the von Neumann architecture which involves the movement of data between the memory unit and the process unit separately. What's known as the "von Neumann bottleneck" is this transfer between the two units (call the bus). Neuromorphic computing offers an alternative to this by using memristors (resistors that remember their input, even after the electrical bias has been stopped). A surface of nanoparticles below the percolation threshold can induce growth of filaments under a bias. Depending on the voltage that is applied, filaments can be destroyed or reformed, making these resettable switches. This is how a neuron in the brain works, with the bridge between the two nanoparticles being the synapse. From here larger arrays of this setup can be implemented with communication channels running between each device. This removes the von Neumann bottleneck, working in parallel with each other at a low power consumption. Differing types of memristors have shown desirable characteristics such as nanoscale sizes, fast switching speeds, and long endurance as devices. Figure 38 Shows the memristor unit, migration from one cluster to another being the principle operation of the device.
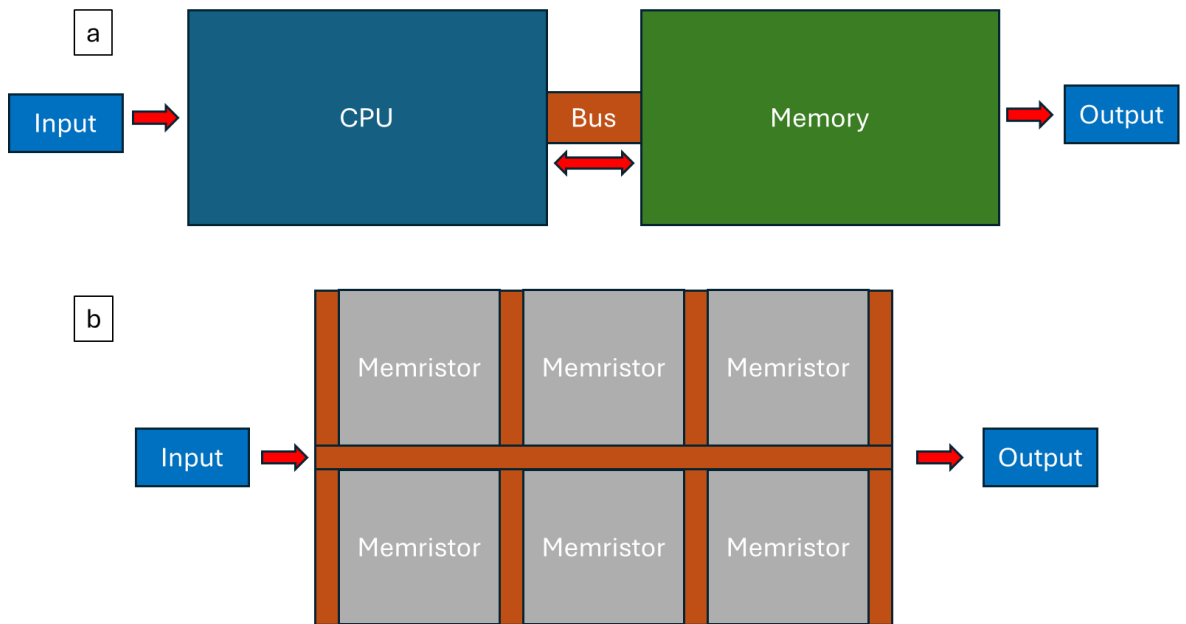
Figure 39: A schematic depicting a) classical von Neumann architecture, highlighting the "bus" being the von Neumann bottleneck. b) shows neuromorphic computing architecture, with information transmission pathways between them

As discussed earlier, neuromorphic computing designed in the setup in Figure 39, an array of memristors will compute in a parallel manner, overcoming the von Neumann bottleneck. Each memristor consists of the neuron and synapse, meaning the whole array is what is considered the "reservoir" or "black box" in reservoir computing. This parallel structure lends itself to also being a low power intensive process.

7.1 The History of Transistors and Moore's Law

To contextualise the significance of exploring alternative computing architectures, it is essential to examine the history of transistors and the emergence of Moore's Law. The transistor, considered one of the most transformative inventions of the 20th century, revolutionised electronics and paved the way for modern computing. Developed in 1947 at Bell Labs by John Bardeen, Walter Brattain, and William Shockley, the transistor replaced bulky vacuum tubes and introduced a compact and reliable solid-state device capable of amplifying and switching electronic signals.

The widespread adoption of transistors fuelled a remarkable surge in computational power and led to the birth of integrated circuits (ICs). In 1965, Gordon Moore, co-founder of Intel Corporation, observed a trend that would shape the future of computing. Moore noted that the number of transistors on integrated circuits was doubling approximately every two years, predicting that this trend would continue for the foreseeable future. This observation came to be known as Moore's Law, which is still roughly accurate to this day.

Moore's Law became a guiding principle for the semiconductor industry, setting the pace for continuous advancements in computing power. The industry embraced the challenge of packing more and more transistors onto a single chip, leading to increasingly powerful processors and enabling a staggering pace of technological innovation. From the rise of personal computers and the internet to the development of mobile devices and the rapid progress of artificial intelligence, Moore's Law propelled an era of unprecedented technological growth.

7.2 The End of Moore's Law and the Need for Alternatives

Despite its remarkable endurance, Moore's Law is now approaching its limits. The miniaturization of transistors faces significant physical and economic constraints. As transistors shrink to nanoscale dimensions, they encounter quantum mechanical effects, thermal limitations, and power density challenges. Additionally, the increasing complexity of manufacturing processes and escalating costs pose substantial barriers to sustaining Moore's Law.

Given these imminent limitations, the computing industry finds itself in a precarious position. Demand for more computing power has not yielded, driven by emerging applications like big data analytics, machine learning, and autonomous systems. More money can be pumped into trying to consistently scale down fabrication but the risk of coming to a dead end is a shadow that constantly looms. To address this, researchers are actively exploring alternative computing architectures that can transcend the constraints of traditional von Neumann computing paradigms. One of

the most promising alternatives is neuromorphic computing, inspired by the structure and functionality of the human brain.

Neuromorphic computing leverages the principles of neural networks and brain-inspired computing to create highly efficient and parallel computing systems. By mimicking the parallel processing and synaptic connections of the brain, neuromorphic architectures have the potential to deliver exceptional computational power while consuming significantly less energy compared to conventional processors. Inroads have already been made, with cluster based neuromorphic architecture being used as the basis of machine learning that can already display pattern recognition. This thesis chapter explores the fabrication of neural network devices using the SAS deposition technique to reach a coverage that sits just under the percolation threshold. The introduction of voltage induces filament growth between the isolated particles which both form and break, not dissimilar to the neuroplasticity of biological neurons in the brain. Filament growth between clusters is still just a working theory, with little being known about formation mechanisms, spatial growth, etc. Therefore, it is of interest to investigate in-situ the growth of filaments in a TEM, potentially revealing how they are formed and give an insight into the system of formation. Before immediate testing on biasing chips, it is important to characterise and experiment with cluster coverage before attempting in-situ experiments.

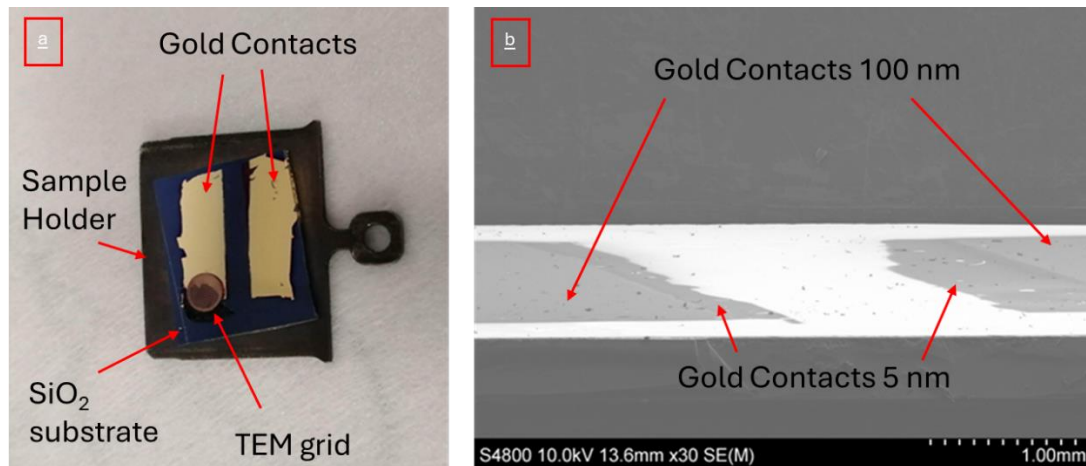## 7.3 Building, Fabricating and Testing of Neuromorphic Devices

Figure 40 a) photo SiO₂ wafer with electrical contacts with TEM grid attached b) SEM image of a), showing the contacts on the SiO₂ surface

The first iteration of the fabrication of electrical contacts on a relatively insulating surface is shown in Figure 40 a) with the support being a cleaved silicon wafer with an insulating layer of SiO_2, 500 nm thick. This is attached to an STM sample holder with double-sided carbon sticky tape. A TEM grid is attached to one of the gold contacts to give a rough estimate of the cluster coverage between the two contacts. Large gold contacts of more than 100 nm were fabricated in a Quorum sputter coater using a gold target as a material and a rudimentary mask made from aluminium foil to shape the contacts. Figure 40 b) shows a tilted view of the contacts, highlighting the thinner region shown by the darker contrast on the inside edges of the contacts.
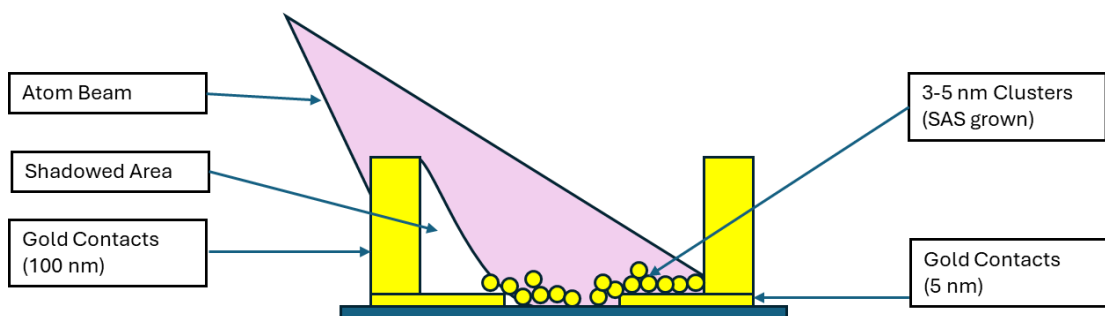

Figure 41: Diagram of the SAS, highlighting the need for a smaller base layer for contacts. The contacts were fabricated from using an initial wide mask to create the first 5 nm layer by way of exposure in the Quorum, subsequently changing out to a thinner mask to continue to the larger 100 nm contact fabrication

As the clusters are on the order of single digits, up to tens of nanometres, shadowing by the walls of the contacts can occur during deposition. Without movement of the sample during exposure, it will be impossible to create a network of connecting nanoparticles from one contact to another. This underscores the importance of employing PVD (Physical Vapor Deposition) from the Quorum sputter coater to precisely deposit a thin layer of target material that closely matches the cluster sizes inferred from the analysis of the calibration images presented in Figure 38 typically in the vicinity of 5 nm. When this is complete, a thicker layer (100 nm) of gold is deposited to guarantee there is enough material to ensure a solid contact to the measuring electrode.

There was a need to calibrate the synthesis before deposition due to low availability and high cost of the chips. A silicon wafer with a 200 nm layer of oxide was used to best simulate the environment on the chips. The viewing/deposition window of the chips consists of a very thin layer of SiO_2, which is electrically transparent for TEM viewing. This is an important step, using a nearly identical support surface, to simulate cluster formation on the chip's window. Due to the method of growth being surface dependant, a simulation on a differing material may lead to unforeseen effects such as different size clusters, or a higher concentration of smaller clusters. The second important factor that SiO_2 allows for is the higher resistance it provides in the form of an isolating layer beneath the area of interest. This assures that the signal measured is coming from the contact-nanoparticle-contact pathway and not shorting below the surface. Another material considered for testing was glass, but during assembly of the in-situ probe measurements, the significantly larger resistance of glass made it was impossible to tell if the probes were in contact with the sample. SiO_2 layer has a high enough resistance to avoid shorting the neural network but a low enough resistance to display that the probes are indeed in physical contact.
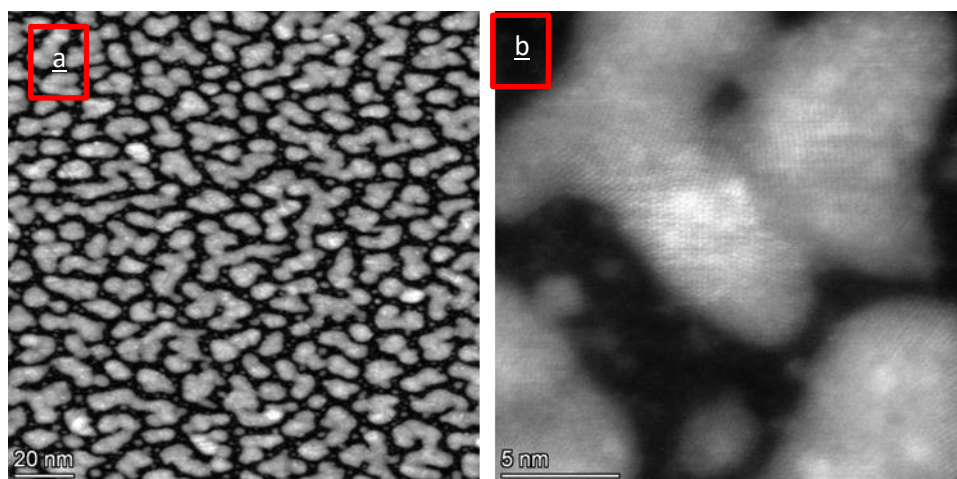
Figure 42 TEM Images of a) Au NP clusters after deposition and b) at high magnification to show crystalline structure

Figure 42 shows the cluster coverage of the TEM grid from Figure 41 a) after deposition. During cluster exposure, the two electrodes measuring across the two contacts allowed for in-situ monitoring of the resistance enabling termination of deposition after the correct exposure time. Termination at a resistance of 1.3 MΩ produced the nanostructures here as islands with a coverage of around 65%, which matches up to expectations from the literature. Figure 42 b) shows a higher magnification which displays the crystalline structure of the islands with many atomic columns. An important detail to note is that this image highlights voids between the islands. Several small clusters can be seen within these voids, some of which adhered to the side walls of the islands while others remain isolated and disconnected. It is vital to know which growth mechanism is in effect on this material. If it transpires that Stranski-Krastinov is the dominant mechanism then it could prove that the two contacts may have been bridged by a layer-by-layer growth, or similarly that FM mode is not idea for similar reasons. VW, isolated nanoparticles dispersed through the sample, is the preferable mechanism, ensuring there is no percolation without instigating bridging through filament formation. Conversely, it is not known if inducing filament growth will cause aggregation of the clusters due charge effects or even through heating, as it is a well-documented trait that adding heat to nanoparticles encourages sintering.
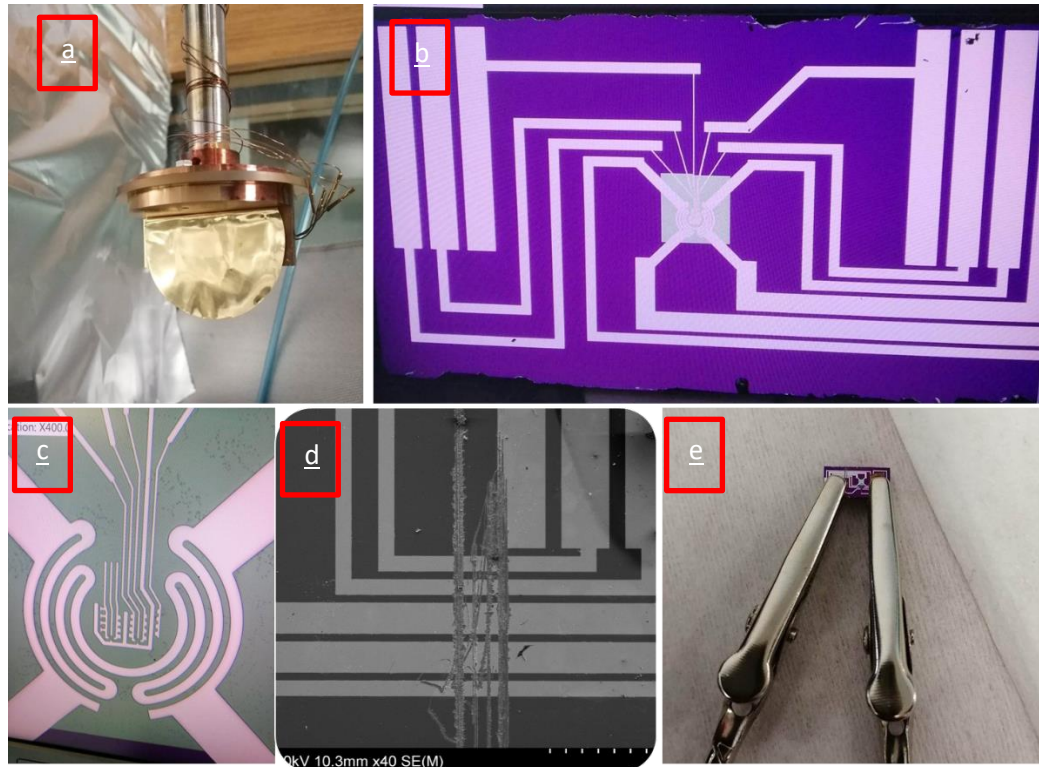
Figure 43 a) Photo of gold target attached to the matrix support, b) microscope image of biasing chip, c) images of platinum patterned contacts on the chip, d) scored heating tracks and e) crocodile clips attached to biasing chip for *in-situ* measuring of resistance during deposition

The apparatus and cumulative efforts to be able to deposit and record a coverage that sits just under the percolating threshold are shown in Figure 43. Figure 43 a) shows a 99.999% pure gold target attached to the matrix support of the MiniMACS to cut down on experimental prep time, avoiding the need for e-beam evaporation of target material. Figure 43 b) shows a microscopic image of the biasing chip to be used in-situ during neuromorphic filament formation. Figure 43 c) displays the area of interest on the chip, platinum patterned contacts, designed in a way that the most likely area for percolation will occur in the areas that are closest together. The film that the strips are supported on is a thin window of SiO2. It will be thin enough to allow electrons to pass through for TEM characterisation, yet be isolating enough as to not short the contacts, forcing the charge to go through the nanostructures. Due to the compact nature of the biasing chip and limited time available to complete this part of the project, a crude setup of crocodile clips were used along with a small foil of molybdenum to make contact with electrodes on the device. Some of these secondary electrodes were for the use of heating, but they bridged the whole chip. A

diamond pen was used to score the heating circuitry, meaning no readouts from them could interfere with the relevant measurements. An SEM image of the successful scoring can be seen in sample 41 d). The metallic contacts were secured, and resistance measured across them to confirm the disruption had been successful and there were no shorts.
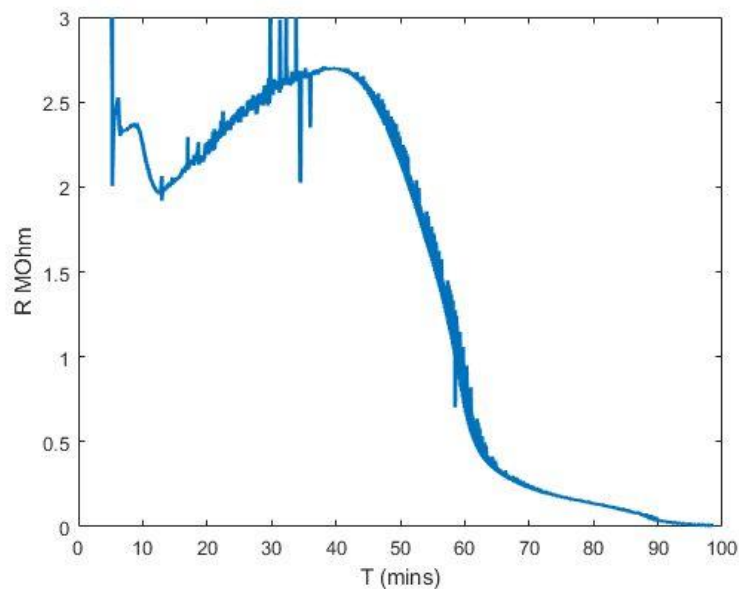

Figure 44: Graph of resistance against time of deposition

A calibration graph of resistance recorded by a Keithley 2601 SourceMeter in 0.5 s intervals is shown displayed in Figure 44. The sample was exposed to the atom beam and allowed to become saturated i.e., deliberately bridging the two contacts. The resistance appears to dip between the 10- and 15-minute mark. Thereafter the resistance begins to increase (possibly due to aggregation of atoms into clusters – further from each other). After reaching a peak resistance at 40 minutes, resistance sharply falls until about the 60-minute mark, where resistance still lowers but at a less accelerated rate. One possibility of this increase in resistance could be due to the nature of how the SAS works. With VW growth being the theorised cluster growth mechanism, atoms could be energetically moving around the sample, but as more and more clusters begin their formation, the clusters become a type of "sink" for the energetic atoms to be absorbed into. There might be a different initial growth mechanism, by way of SK or FM, where resistance is decreased due to the plethora of free atoms, but as exposure time increases, VW growth wins out. The region of

focus is between the 40- and 65-minute marks, where it is evidenced that the "s" curve mentioned in previous literature is observed. Alternatively, hot atoms of gold landing on the surface may be transferring heat to the silicon dioxide layer, increasing resistance across the reading.

 At first thought it would be forgiven to think that there would be a steep drop in resistance, as current will flow once there is a definite bridge between the measure areas. However, there are three regimes at play. The initial slow drop at 40 and 50 minutes can be attributed to quantum tunnelling, whereby conductive elements are close enough together for electrons to "jump" over to another constituent, if the right conditions are met (distance, energy). The steep decline in resistance from 50 to 60 mins is credited by the network reaching the percolation threshold. As more and more material lands on the surface, potential for more pathways become connected, allowing the transfer of energy until finally enough pathways are accessible for the electrons to move from source to drain without much difficulty. This is an exponential decay due to the probability of the atoms landing on an uninhabited area becoming less and less likely. This invaluable data allowed for estimation of time to complete each exposure for each chip as well as a deeper understand of the quirks of the process.
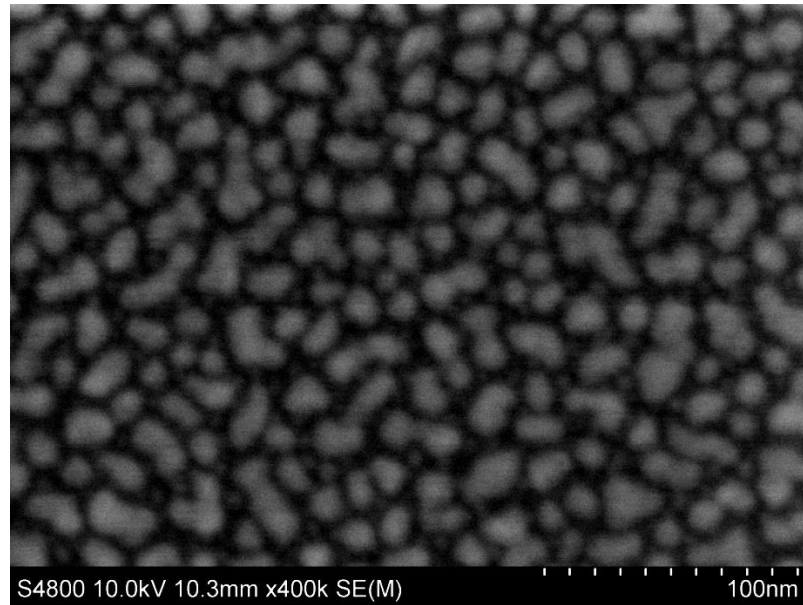
Figure 45: SEM image of Au nanoparticles on biasing chip 1, midway through the "s" curve

Figure 45 shows the first chip to be exposed to the beam. Before sending the samples to be imaged under TEM, the chips were imaged using an in-house SEM to get an initial idea of what the coverage may look like. As it is unknown where on the resistance curve the optimum circumstance to terminate exposure is, the three chips ceased being exposed to the beam at different and significant resistance markers. Figure 45 is a coverage with a resistance of 1.5MΩ, right in the middle of the "s" curve, with a coverage of 60-70%. As the SEM does not have as high a resolution as the TEM, it is difficult to affirm if there are a significant number of small clusters/single atoms presents in the voids. However, there are instances of signal between the larger clusters, indicating clusters of somewhere around the 5 nm range. The clusters in question can be seen to be just below the material threshold needed to form islands, with some evidence to suggest they are not as stable as spherical nanoparticles in this state. After using a threshold mask that relates to the intensity of the image, it was seen that the coverage by surface area was roughly 60-70%. Due to the comparatively low resolution of the SEM when compared to TEM, the exact coverage is quite imprecise.
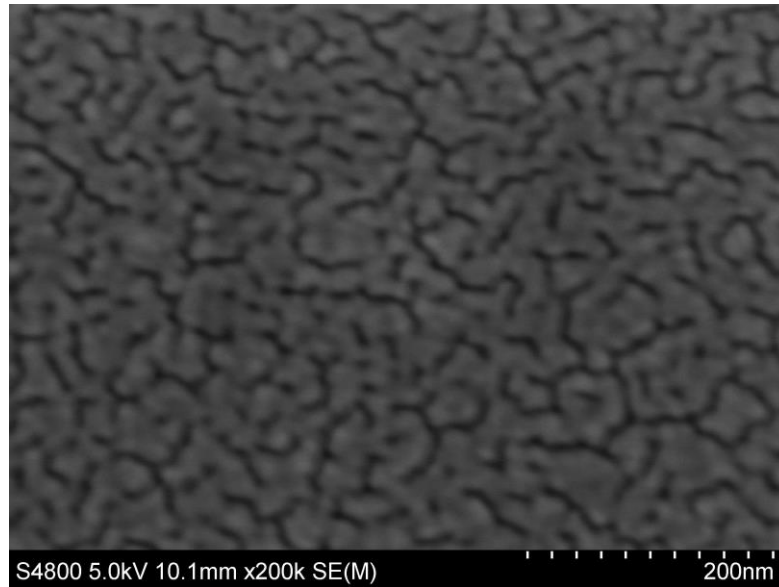
Figure 46: SEM Image of Au clusters on chip 2, forming interconnected networks. They are no long distinct nanoparticles, but is getting to thin film levels of thickness

A second chip was exposed to the atomic beam for longer, with a resistance of 1.25 MΩ and a surface area coverage, seen in Figure 46, of 68-70%. Here, spherical clusters are no more, instead shown to be larger interconnected networks of islands or "worms". The reason why there is still a modicum (but still significant) amount of resistance is the fact that despite being interconnected, the networks are isolated enough to have current flow through small bottlenecks. The image reveals bulky areas which occasionally filter down to other networks with single points of entry, severely hindering the flow of electrons. Later in this chapter, high magnification TEM images are used to examine the small voids in between the networks, investigating to see the volume of single atoms/small clusters, or if they have all been absorbed/adsorbed into the rest of the network. This could determine at which point during growth, through single atom sputtering, the device is at its most stable i.e., loose single atoms could have unforeseen consequences by being less stable and free to move around and bridge/decouple particles. After analysis, the area coverage was seen to be over the recommended range at between around 68-75%. However, the resistance measurement was still showing a value below the percolation limit, i.e., a lower conductivity of the native support. It can therefore be inferred that this coverage range is to be used as a guideline rather than implicit fact which may be explained because of differing cluster formation mechanisms or even other substrates.
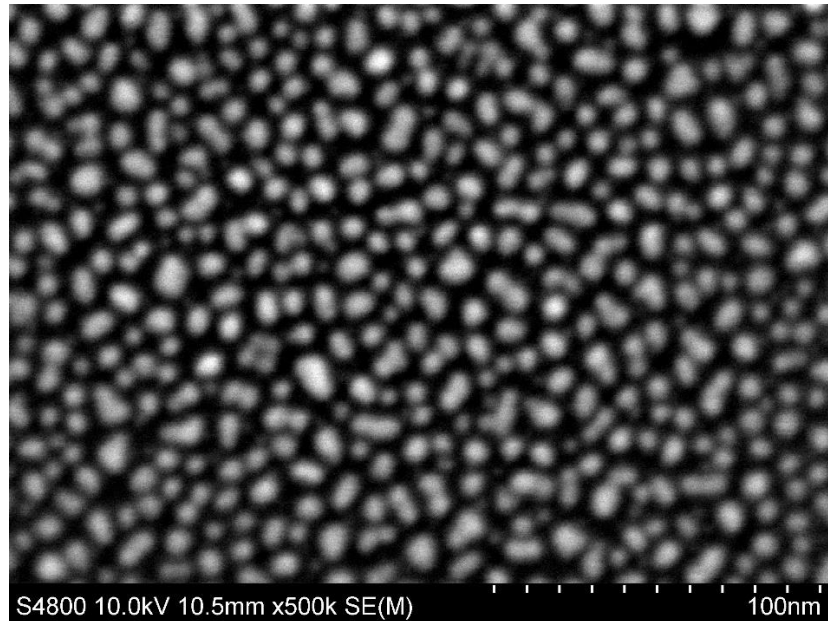
Figure 47: SEM image of chip 3, whereby the termination of cluster deposition was before the middle of the "s" curve, i.e., when the sample is measuring more resistant than the other two chips

Figure 47 shows an SEM image of chip 3, which had its exposure to the atom beam interrupted at the higher end of the permitted "s" curve area at 1.75 MΩ. This resulted in a coverage by surface area of 55-60%. The 500,000x magnification may show the unintentionally deceptive view that the clusters are of similar size as chip one, but after size analysis there are a lot of smaller particles in chip three. It is unsure whether this level of coverage is sufficient to allow the formation of filaments. This method of using three chips with different coverages around the desired resistance is ideal to see the range in which filament formation is achievable. The rough coverage for this is around 55% - 60% which is below the recommended coverage. It is much more difficult to determine beforehand if this chip can be induced to percolate as the resistance lies more towards the top of the "s" curve from Figure 44 with nothing indicating correct deposition.
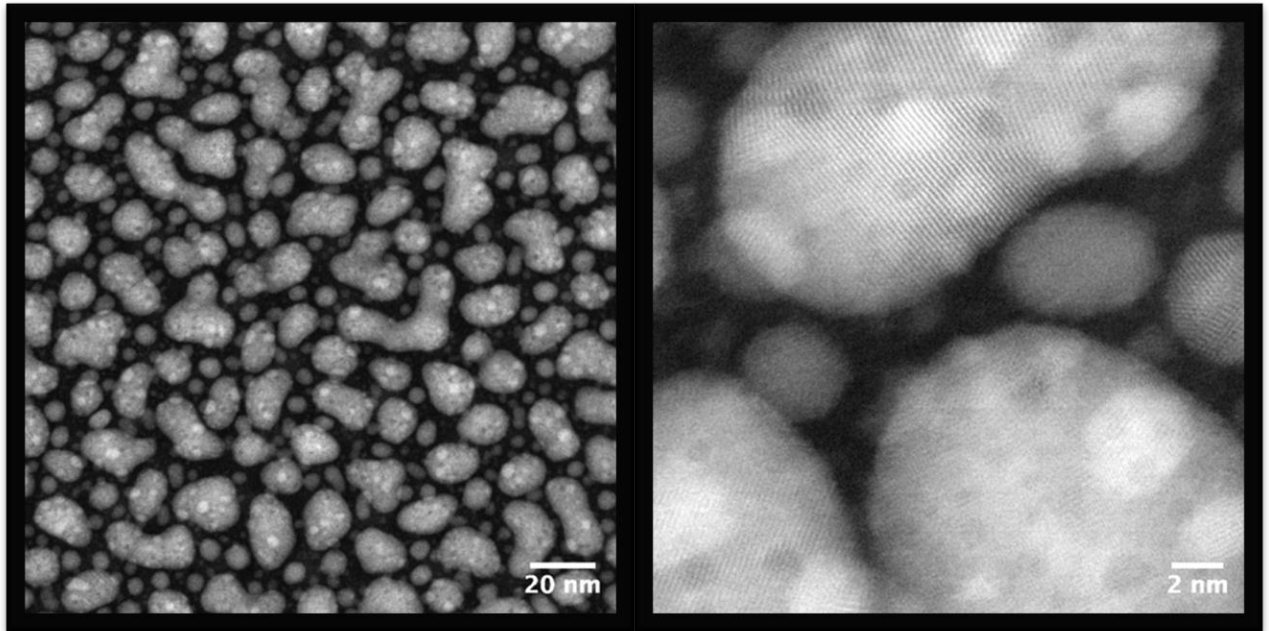
Figure 48: HAADF-STEM images of chip 1, highlighting the smaller clusters and potentially single atoms in between the voids of the larger clusters

HAADF-STEM images of chip one under the electron beam are shown in in Figure 48 and as would be showing smaller clusters positioned either below or above the larger cluster. This higher resolution allows for better observation of the details missed out by SEM imaging alone. Single atoms can be seen in between the clusters. Unfortunately, due to the impromptu loading of the system specifically for these chips, the TEM window Had been damaged along one of the contacts. Focused ion beam (FIB) was attempted to try and bridge the gap but was ultimately unsuccessful since a significant amount of the window sagged, too much for platinum to be deposited to bridge the gap. Meaning that there is no potential across the chip, with no chance to induce filament growth.
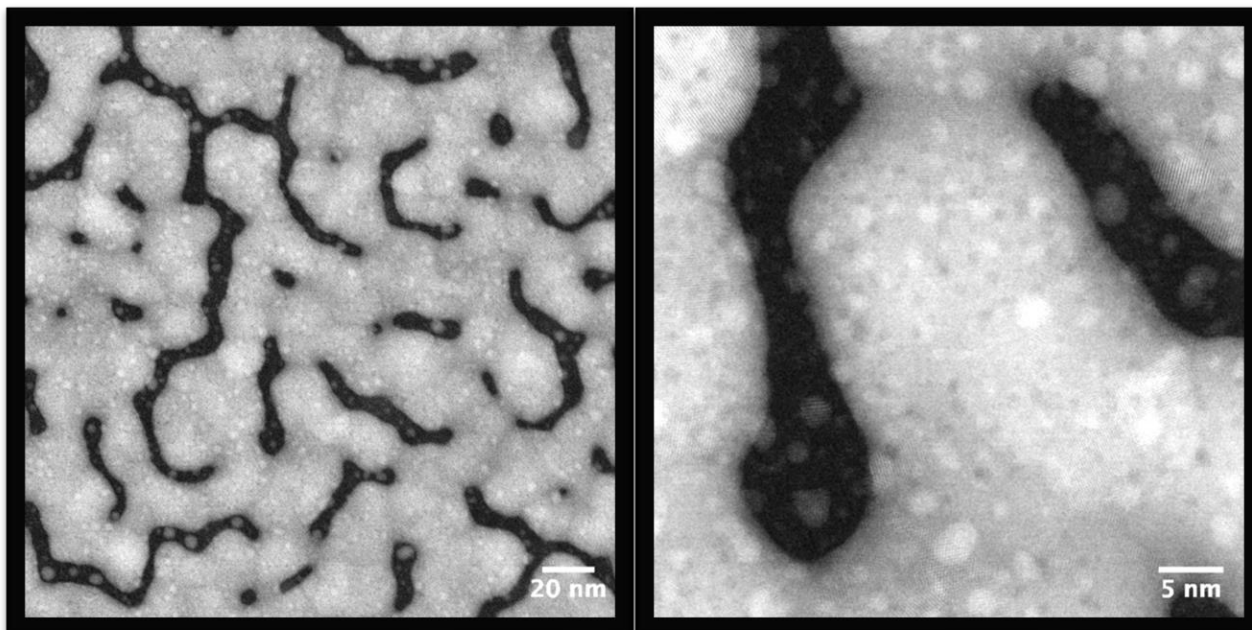
Figure 49: HAADF-STEM images of chip 2, further highlighting the smaller clusters growing in between the voids. Smaller clusters can also be seen underneath the larger formations

Figure 49 shows a more magnified view of the structure beyond the percolation threshold. The image reveals a network formed by gold nanoparticles, which have coalesced to create a continuous and interconnected structure. This indicates that any further application of voltage will not induce the growth of additional filaments between the nanoparticles, leading to a stable conductive network. Moreover, the image provides evidence of atom and cluster growth occurring within the void spaces of the gold percolating network, suggesting the presence of dynamic processes contributing to the film's formation. It is important to note that the termination point of the beam must be considerably before reaching this coverage, i.e., ceasing operations at a higher resistance on the "s" curve, demonstrated by Figure 44.

Figure 50: HAADF-STEM images of chip 3. Smaller clusters litter the sample surface, but are spaced in a way that could be difficult to induce filament growth

Figure 50 shows that it is evident the gold film contains less material compared to the previous chips. However, the image presents an intriguing characteris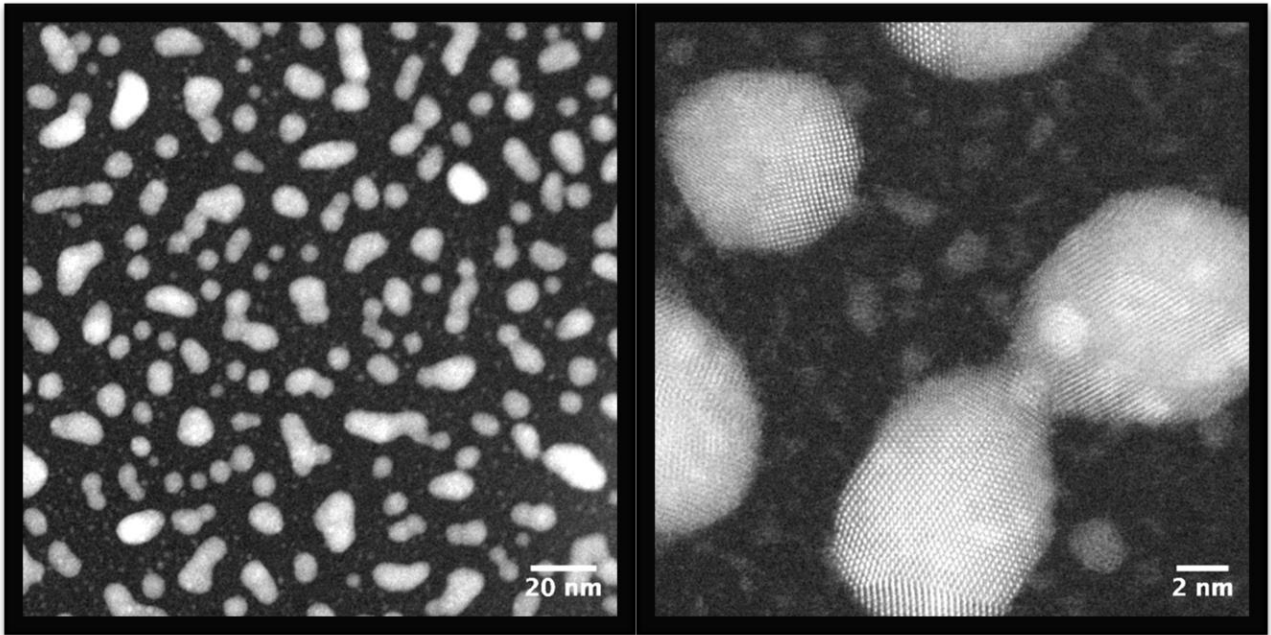tic that makes it a compelling candidate for identifying the termination point within the percolating network. There is ample space between the nanoparticles, potentially offering room for filament growth when subjected to applied voltage. The presence of numerous small 2D clusters and single atoms scattered throughout the film adds further complexity to the investigation. These nanostructures could play a significant role in the filament formation process, and their influence warrants exploration.

Unfortunately, as with chip one, the window on the chip as well as the circuitry had broken, with no means to be repaired with Pt deposition on the FIB. The windows of chips one and three broke during deposition, meaning the crude way of loading and unloading the samples in the chamber is problematic.

7.4 Conclusion

A testing rig has been successfully created to allow the in-situ measurement and recording of the resistance during deposition of clusters on a surface between two electrodes. Fabrication recipes of the electrodes, suitable candidates for support material, calibration of the "s" resistance curve and ideas of termination point of the beam were all investigated. Since all three chips had fractured windows, it has

become apparent that the current setup of loading and unloading the samples is currently not a viable option. Further alterations to the setup must be made to ensure that this does not happen again.

Neuromorphic work presented in Chapter 7 has already by used by Dr Milos Baljozovic who has imaged the percolating film of nanoparticles, used TEM during in-situ biasing and has observed the formation pathways. Further work is now needed to investigate the formation mechanism of the filaments. This work will lead to further exciting development in the field and open new and future technologies in computing and understanding of the workings of the brain. To gain a deeper understanding of the percolating gold film's behaviour, two experiments are proposed. The first experiment involves varying the dispersions of the gold clusters, creating different gap sizes between them. This investigation seeks to determine if larger gaps require a higher voltage to induce filament growth, offering insights into the critical role of spacing in the formation of conductive paths, as well as the limits of filament growth. The second experiment involves conducting in-situ voltage testing on the gold film and capturing before-and-after TEM images aiming to focus on the smaller clusters/single atoms. This analysis aims to observe any changes in the distribution and abundance of the small 2D clusters and single atoms within the film. If these nanostructures are found to decrease in number after voltage testing, it could indicate that they contribute to filament growth by being absorbed into larger clusters. Conversely, if they remain on the sample surface unaffected, it suggests that they may not significantly influence the filament formation process. Overall, these proposed experiments present promising avenues for further investigation, shedding light on the interplay between nanoparticle spacing, the presence of small 2D clusters/single atoms, and their role in filament growth within the percolating gold film. Such insights could hold valuable implications for the design and optimization of nanoelectronics and advanced materials.

Chapter 8: Conclusions

8.1 Conclusions

Nanoparticles are the subject of intense research by the scientific and engineering communities and the work presented in this thesis has added to the stock of knowledge in the field and developed new paths that the field could follow.

The work reported includes the creation of the MiniMACS system that can produce Au NPs by evaporating a metal into a cryocooled gas matrix that is then sputtered using an incident ion beam. Previously, this mechanism has used CO_2 solid for high matrix temperature usage but in fact at liquid helium temperatures. However, for the first time, the work reported here has used butane gas allowing Au NP synthesis at significantly high liquid nitrogen temperatures. The nanoparticles formed had an average diameter of 1.8 ± 0.5nm which compares favourably with previous MACS data where Au NPs were synthesised with diameter $2 - 3$ nm by Zhao et al. at lower temperatures.

While carrying out the MiniMACS experiments a more streamlined mode of operation was demonstrated by operating the system as a Sputtered Atom Source. The nanoparticles produced using this method varied in sized from $0.5 - 3.5$ nm, the size depends on the amount of material sputtered out of the sample, as well as the surface conditions used for nucleation. Structural analysis showed that gold nanoparticles on carbon films tend to be of an amorphous form when below 300 atoms in size, tending to FCC and decahedral structures when clusters were larger than 300 atoms. It was also found the FCC was narrowly more common that decahedral.

A very interesting observation made in this thesis occurred during the STEM imaging of Au NPs produced using the SAS method. It was seen in real time that when a decahedral cluster consisting of 259 atoms was close to an amorphous cluster of 50 atoms, the two clusters aggregated. Furthermore, after aggregation, the new cluster was an unstable FFC, switching between amorphous, with little evidence of

decahedral structures. This suggests that the "magic number" of 309 atoms is the approximate tipping point for isomer structural stability in gold nanoclusters grown at room temperature on carbon.

For nanoparticles produced using the MiniMACS or SAS methods to be commercially viable, industrial level scale up and the ability to switch metals is necessary, as was investigated in Chapter 6. Ag and Pb NPs were synthesised by the MACS method and calculations have shown that this would produce NPs at a rate of 50% of what is currently targeted in industry for research and development purposes. As the MACS method is also potentially significantly cheaper than current chemical methods and produces less waste and environmental impact, this is a promising result.

Lead nanoparticles produced by the MACS method have also been used for water purification by embedding them in carbon paper. The results demonstrated in Chapter 6 of this thesis are comparable to work done by other groups that have used electro – spinning of carbon fibre and nanoparticle paste. The advantage of the MACS methods is that the nanoparticle type and fibre material can be easily and quickly changed.

Silver nanoparticles produced by the MACS method have been deposited onto copper and silver foils for uses in catalysis. This work is still ongoing via a collaboration with the University of Bologna.

Finally, gold nanoparticles produced using the MiniMACS method were deposited between prefabricated electrodes for neuromorphic applications. Chapter 7 describes the process of fabrication, i.e., contact thickness and shape, choosing a suitable substrate and construction of the testing apparatus. A method has been developed to enabled controlled cluster deposition to the point of percolation and allow pathways to form and neuromorphic behaviour to be studied. Further development has been undertaken to build a more user-friendly *in-situ* testing rig, to allow for any delicate samples to be easily coated without breaking. Wire bonding along with a chip carrier has been implemented.

References

1. Ivask, A. *et al.* Toxicity mechanisms in Escherichia coli vary for silver nanoparticles and differ from ionic silver. *ACS Nano* **8**, 374–386 (2014).

2. Navarro, E. *et al.* Toxicity of silver nanoparticles to Chlamydomonas reinhardtii. *Environ Sci Technol* **42**, 8959–8964 (2008).

3. Lok, C. N. *et al.* Silver nanoparticles: Partial oxidation and antibacterial activities. *Journal of Biological Inorganic Chemistry* **12**, 527–534 (2007).

4. Lok, C. N. *et al.* Proteomic analysis of the mode of antibacterial action of silver nanoparticles. *J Proteome Res* **5**, 916–924 (2006).

5. Wong, K. K. Y. & Liu, X. Silver nanoparticles - The real 'silver bullet' in clinical medicine? *Medchemcomm* **1**, 125–131 (2010).

6. Marambio-Jones, C. & Hoek, E. M. V. A review of the antibacterial effects of silver nanomaterials and potential implications for human health and the environment. *Journal of Nanoparticle Research* **12**, 1531–1551 (2010).

7. Li, W. R. *et al.* Antibacterial activity and mechanism of silver nanoparticles on Escherichia coli. *Appl Microbiol Biotechnol* **85**, 1115–1122 (2010).

8. Rai, M. K., Deshmukh, S. D., Ingle, A. P. & Gade, A. K. Silver nanoparticles: The powerful nanoweapon against multidrug-resistant bacteria. *J Appl Microbiol* **112**, 841–852 (2012).

9. Reidy, B., Haase, A., Luch, A., Dawson, K. A. & Lynch, I. Mechanisms of silver nanoparticle release, transformation and toxicity: A critical review of current knowledge and recommendations for future studies and applications. *Materials* **6**, 2295–2350 (2013).

10. Lemire, J. A., Harrison, J. J. & Turner, R. J. Antimicrobial activity of metals: Mechanisms, molecular targets and applications. *Nat Rev Microbiol* **11**, 371–384 (2013).

11. Ivask, A. *et al.* Size-dependent toxicity of silver nanoparticles to bacteria, yeast, algae, crustaceans and mammalian cells in vitro. *PLoS One* **9**, (2014).

12. Agnihotri, S., Mukherji, S. & Mukherji, S. Immobilized silver nanoparticles enhance contact killing and show highest efficacy: Elucidation of the mechanism of bactericidal action of silver. *Nanoscale* **5**, 7328–7340 (2013).

13. Tian, J. *et al.* Topical delivery of silver nanoparticles promotes wound healing. *ChemMedChem* **2**, 129–136 (2007).

14.   Durán, N. *et al.* Silver nanoparticles: A new view on mechanistic aspects on antimicrobial activity. *Nanomedicine* **12**, 789–799 (2016).

15.   Prabhu, S. & Poulose, E. K. Silver nanoparticles: mechanism of antimicrobial action, synthesis, medical applications, and toxicity effects. *International Nano Letters 2012 2:1* **2**, 1–10 (2012).

16.   Liyanage, P. Y. *et al.* Nanoparticle-mediated targeted drug delivery for breast cancer treatment. *Biochim. Biophys. Acta Rev. Cancer* **1871**, 419–433 (2019).

17.   Bamrungsap, S. *et al.* Nanotechnology in therapeutics a focus on nanoparticles as a drug delivery system. *Nanomedicine* **7**, 1253–1271 (2012).

18.   Mirza, A. Z. & Siddiqui, F. A. Nanomedicine and drug delivery: a mini review. *Int. Nano Lett.* **4**, 94 (2014).

19.   Shi, J., Votruba, A. R., Farokhzad, O. C. & Langer, R. Nanotechnology in drug delivery and tissue engineering: from discovery to applications. *Nano Lett.* **10**, 3223–3230 (2010).

20.   Martinho, N., Damgé, C. & Reis, C. P. Recent advances in drug delivery systems. *J. Biomater. Nanobiotechnol.* **2**, 510–526 (2011).

21.   Felice, B., Prabhakaran, M. P., Rodríguez, A. P. & Ramakrishna, S. Drug delivery vehicles on a nano-engineering perspective. *Mater. Sci. Eng. C* **41**, 178–195 (2014).

22.   Jahangirian, H., Lemraski, E. G., Webster, T. J., Rafiee-Moghaddam, R. & Abdollahi, Y. A review of drug delivery systems based on nanotechnology and green chemistry: green nanomedicine. *Int. J. Nanomed.* **12**, 2957–2978 (2017).

23.   Al Tamimi, S. *et al.* Synthesis and analysis of silver–copper alloy nanoparticles of different ratios manifest anticancer activity in breast cancer cells. *Cancer Nanotechnol.* **11**, 1–16 (2020).

24.   Parveen, S., Misra, R. & Sahoo, S. K. Nanoparticles: a boon to drug delivery, therapeutics, diagnostics and imaging. *Nanomed. Nanotechnol.* **8**, 147–166 (2012).

25.   Wang, E. C. & Wang, A. Z. Nanoparticles and their applications in cell and molecular biology. *Integr Biol (Camb).* **6**, 9–26 (2014).

26.   Khan, I., Saeed, K. & Khan, I. Nanoparticles: properties, applications and toxicities. *Arab. J. Chem.* **12**, 908–931 (2019).

27.   Chandrakala, V., Aruna, V. & Angajala, G. Review on metal nanoparticles as nanocarriers: current challenges and perspectives in drug delivery systems. *Emergent Materials 2021 5:6* **5**, 1593–1615 (2022).

28.   Blanco, E., Shen, H. & Ferrari, M. Principles of nanoparticle design for overcoming biological barriers to drug delivery. *Nature Biotechnology 2015 33:9* **33**, 941–951 (2015).

29. Jeong, S. *et al.* Stable aqueous based Cu nanoparticle ink for printing well-defined highly conductive features on a plastic substrate. *Langmuir* **27**, 3144–3149 (2011).

30. Sun, J. *et al.* Printable nanomaterials for the fabrication of high-performance supercapacitors. *Nanomaterials* **8**, (2018).

31. MacDonald, W. A. *et al.* Latest advances in substrates for flexible electronics. *J Soc Inf Disp* **15**, 1075 (2007).

32. Tan, H. W., An, J., Chua, C. K. & Tran, T. Metallic Nanoparticle Inks for 3D Printing of Electronics. *Adv Electron Mater* **5**, (2019).

33. Kukkola, J. *et al.* Inkjet-printed gas sensors: Metal decorated WO 3 nanoparticles and their gas sensing properties. *J Mater Chem* **22**, 17878–17886 (2012).

34. Kamyshny, A. Metal-based Inkjet Inks for Printed Electronics. *The Open Applied Physics Journal* **4**, 19–36 (2011).

35. Yang, W. & Wang, C. Graphene and the related conductive inks for flexible electronics. *J Mater Chem C Mater* **4**, 7193–7207 (2016).

36. Rossouw, D., Botton, G. A., Najafi, E., Lee, V. & Hitchcock, A. P. Metallic and semiconducting single-walled carbon nanotubes: Differentiating individual SWCNTs by their carbon 1s spectra. *ACS Nano* **6**, 10965–10972 (2012).

37. Nayak, L., Mohanty, S., Nayak, S. K. & Ramadoss, A. A review on inkjet printing of nanoparticle inks for flexible electronics. *J Mater Chem C Mater* **7**, 8771–8795 (2019).

38. Wang, Y. *et al.* Fracture and failure of nanoparticle monolayers and multilayers. *Nano Lett* **14**, 826–830 (2014).

39. Hisatomi, T., Kubota, J. & Domen, K. Recent advances in semiconductors for photocatalytic and photoelectrochemical water splitting. *Chem Soc Rev* **43**, 7520–7535 (2014).

40. Liu, L. & Corma, A. Metal Catalysts for Heterogeneous Catalysis: From Single Atoms to Nanoclusters and Nanoparticles. *Chem Rev* **118**, 4981–5079 (2018).

41. Furukawa, H., Cordova, K. E., O'Keeffe, M. & Yaghi, O. M. The chemistry and applications of metal-organic frameworks. *Science (1979)* **341**, (2013).

42. Chen, Y. *et al.* Single-Atom Catalysts: Synthetic Strategies and Electrochemical Applications. *Joule* **2**, 1242–1264 (2018).

43. Li, Y., Keller, A. L., Cryan, M. T. & Ross, A. E. Metal Nanoparticle Modified Carbon-Fiber Microelectrodes Enhance Adenosine Triphosphate Surface Interactions with Fast-Scan Cyclic Voltammetry. *ACS Measurement Science Au* **2**, 96–105 (2022).

44. Bhatt, C. S. *et al.* Sustainable Bioengineering of Gold Structured Wide-Area Supported Catalysts for Hand-Recyclable Ultra-Efficient Heterogeneous Catalysis. *ACS Appl Mater Interfaces* **14**, 51855–51866 (2022).

45. Astruc, D., Lu, F. & Aranzaes, J. R. Nanoparticles as recyclable catalysts: The frontier between homogeneous and heterogeneous catalysis. *Angewandte Chemie - International Edition* **44**, 7852–7872 (2005).

46. Zhu, S. *et al.* One-Step Synthesis of a High Entropy Oxide-Supported Rhodium Catalyst for Highly Selective CO Production in CO 2 Hydrogenation . *ACS Appl Mater Interfaces* (2023) doi:10.1021/ACSAMI.3C02829.

47. Ghosh, M. & Khan, S. N-Heterocyclic Carbenes Capped Metal Nanoparticles: An Overview of Their Catalytic Scope. *ACS Catal* 9313–9325 (2023) doi:10.1021/ACSCATAL.3C01824.

48. Haruta, M., Kobayashi, T., Sano, H. & Yamada, N. Novel Gold Catalysts for the Oxidation of Carbon Monoxide at a Temperature far Below 0 °C. *Chem Lett* **16**, 405–408 (1987).

49. Yamamoto, K., Imaoka, T., Tanabe, M. & Kambe, T. New Horizon of Nanoparticle and Cluster Catalysis with Dendrimers. *Chem Rev* **120**, 1397–1437 (2020).

50. Szuwarzyński, M. *et al.* Enhanced Assembly of Ag Nanoparticles for Surface-Independent Fabrication of Conductive Patterns. *ACS Appl Nano Mater* **5**, 12711–12719 (2022).

51. Samantaray, M. K. *et al.* The Comparison between Single Atom Catalysis and Surface Organometallic Catalysis. *Chem Rev* **120**, 734–813 (2020).

52. Imaoka, T., Kitazawa, H., Chun, W. J. & Yamamoto, K. Finding the Most Catalytically Active Platinum Clusters with Low Atomicity. *Angewandte Chemie - International Edition* **54**, 9810–9815 (2015).

53. Xie, C., Niu, Z., Kim, D., Li, M. & Yang, P. Surface and Interface Control in Nanoparticle Catalysis. *Chem Rev* **120**, 1184–1249 (2020).

54. Zhu, J., Hu, L., Zhao, P., Lee, L. Y. S. & Wong, K. Y. Recent Advances in Electrocatalytic Hydrogen Evolution Using Nanoparticles. *Chem Rev* **120**, 851–918 (2020).

55. Meng, L. *et al.* Theoretical and Experimental Advances in High-Pressure Behaviors of Nanoparticles. *Chem Rev* (2023) doi:10.1021/ACS.CHEMREV.3C00169.

56. Qiao, B. *et al.* Single-atom catalysis of CO oxidation using Pt1/FeOx. *Nat Chem* **3**, 634–641 (2011).

57. Susanna, D., Balakrishnan, R. M. & Ponnan Ettiyappan, J. Ultrasonication-assisted green synthesis and characterization of gold nanoparticles from Nothapodytes

foetida: An assessment of their antioxidant, antibacterial, anticancer and wound healing potential. *J Drug Deliv Sci Technol* **87**, (2023).

58. Samantaray, M. K. *et al.* Surface organometallic chemistry in heterogeneous catalysis. *Chem Soc Rev* **47**, 8403–8437 (2018).

59. Aikens, C. M. & Jarrold, C. C. Virtual Issue on Experiment-Theory Synergies in the Study of Metal and Metal-Containing Clusters. *Journal of Physical Chemistry A* **127**, 3–5 (2023).

60. Xu, W., Li, S., Ji, J., Chen, H. & Feng, Y. Site-specific growth of gold nanoparticles on Bismuth Selenide hexagonal nanoplates. *J Colloid Interface Sci* **649**, 826–831 (2023).

61. Pasquale, L. *et al.* Atmosphere-Induced Transient Structural Transformations of Pd-Cu and Pt-Cu Alloy Nanocrystals. *Chemistry of Materials* **33**, 8635–8648 (2021).

62. Darmadi, I. *et al.* Bulk-Processed Plasmonic Plastic Nanocomposite Materials for Optical Hydrogen Detection. *Acc Chem Res* (2023) doi:10.1021/ACS.ACCOUNTS.3C00182.

63. Trindell, J. A., Duan, Z., Henkelman, G. & Crooks, R. M. Well-Defined Nanoparticle Electrocatalysts for the Refinement of Theory. *Chem Rev* **120**, 814–850 (2020).

64. Wang, A., Li, J. & Zhang, T. Heterogeneous single-atom catalysis. *Nat Rev Chem* **2**, 65–81 (2018).

65. Shifrina, Z. B., Matveeva, V. G. & Bronstein, L. M. Role of Polymer Structures in Catalysis by Transition Metal and Metal Oxide Nanoparticle Composites. *Chem Rev* **120**, 1350–1396 (2020).

66. Wang, Q. & Astruc, D. State of the Art and Prospects in Metal-Organic Framework (MOF)-Based and MOF-Derived Nanocatalysis. *Chem Rev* **120**, 1438–1511 (2020).

67. Zhu, M., Aikens, C. M., Hollander, F. J., Schatz, G. C. & Jin, R. Correlating the crystal structure of A thiol-protected Au25 cluster and optical properties. *J Am Chem Soc* **130**, 5883–5885 (2008).

68. Wang, Q. & Domen, K. Particulate Photocatalysts for Light-Driven Water Splitting: Mechanisms, Challenges, and Design Strategies. *Chem Rev* **120**, 919–985 (2020).

69. Zhang, L., Zhou, M., Wang, A. & Zhang, T. Selective Hydrogenation over Supported Metal Catalysts: From Nanoparticles to Single Atoms. *Chem Rev* **120**, 683–733 (2020).

70. Rampino, L. D. & Nord, F. F. Preparation of Palladium and Platinum Synthetic High Polymer Catalysts and the Relationship between Particle Size and Rate of Hydrogenation. *J Am Chem Soc* **63**, 2745–2749 (1941).

71. Ishida, T., Murayama, T., Taketoshi, A. & Haruta, M. Importance of Size and Contact Structure of Gold Nanoparticles for the Genesis of Unique Catalytic Processes. *Chem Rev* **120**, 464–525 (2020).

72. Du, Y., Sheng, H., Astruc, D. & Zhu, M. Atomically Precise Noble Metal Nanoclusters as Efficient Catalysts: A Bridge between Structure and Properties. *Chem Rev* **120**, 526–622 (2020).

73. Bowden, N., Arias, F., Deng, T. & Whitesides, G. M. Self-assembly of microscale objects at a liquid/liquid interface through lateral capillary forces. *Langmuir* **17**, 1757–1765 (2001).

74. Astruc, D. Introduction: Nanoparticles in Catalysis. *Chem Rev* **120**, 461–463 (2020).

75. Xie, C., Niu, Z., Kim, D., Li, M. & Yang, P. Surface and Interface Control in Nanoparticle Catalysis. *Chem Rev* **120**, 1184–1249 (2020).

76. Li, Z. *et al.* Well-Defined Materials for Heterogeneous Catalysis: From Nanoparticles to Isolated Single-Atom Sites. *Chem Rev* **120**, 623–682 (2020).

77. Ishida, T., Murayama, T., Taketoshi, A. & Haruta, M. Importance of Size and Contact Structure of Gold Nanoparticles for the Genesis of Unique Catalytic Processes. *Chem Rev* **120**, 464–525 (2020).

78. Liu, X. *et al.* In-situ fabrication of carbon-metal fabrics as freestanding electrodes for high-performance flexible energy storage devices. *Energy Storage Mater* **30**, 329–336 (2020).

79. Salazar, P., Martín, M., O'Neill, R. D., Roche, R. & González-Mora, J. L. Biosensors Based On Prussian Blue Modified Carbon Fibers Electrodes for Monitoring Lactate in The Extracellular Space of Brain Tissue. *Int J Electrochem Sci* **7**, 5910–5926 (2012).

80. Heidary, N. & Kornienko, N. Operando Raman probing of electrocatalytic biomass oxidation on gold nanoparticle surfaces. *Chemical Communications* **55**, 11996–11999 (2019).

81. Liu, J.-X., Filot, I. A. W., Su, Y., Zijlstra, B. & Hensen, E. J. M. Optimum Particle Size for Gold-Catalyzed CO Oxidation. *J. Phys. Chem. C* **122**, 7 (2018).

82. Gibson, G., Wang, Z., Hardacre, C. & Lin, W. F. Insights into the mechanism of electrochemical ozone production via water splitting on the Ni and Sb doped SnO2 catalyst. *Physical Chemistry Chemical Physics* **19**, 3800–3806 (2017).

83. De Sousa, L. G., Franco, D. V. & Da Silva, L. M. Electrochemical ozone production using electrolyte-free water for environmental applications. *J Environ Chem Eng* **4**, 418–427 (2016).

84. Abbasi, M., Bäckström, J. & Cornell, A. Fabrication of Spin-Coated Ti/TiH x /Ni-Sb-SnO 2 Electrode: Stability and Electrocatalytic Activity . *J Electrochem Soc* **165**, H568–H574 (2018).

85. Pushkarev, A. S., Pushkareva, I. V. & Grigoriev, S. A. Electrochemical generation of ozone in a system with a solid polymer electrolyte. *Russian Journal of Applied Chemistry* vol. 89 1054–1065 Preprint at https://doi.org/10.1134/S107042721607003X (2016).

86. Christensen, P. A., Zakaria, K., Christensen, H. & Yonar, T. The Effect of Ni and Sb Oxide Precursors, and of Ni Composition, Synthesis Conditions and Operating Parameters on the Activity, Selectivity and Durability of Sb-Doped SnO 2 Anodes Modified with Ni . *J Electrochem Soc* **160**, H405–H413 (2013).

87. Yuan, B. *et al.* Synergistic effect of size-dependent PtZn nanoparticles and zinc single-atom sites for electrochemical ozone production in neutral media. *Journal of Energy Chemistry* **51**, 312–322 (2020).

88. Wu, H. *et al.* Stable cycling of double-walled silicon nanotube battery anodes through solid-electrolyte interphase control. *NATURE NANOTECHNOLOGY | ***7**, (2012).

89. Mo, R., Rooney, D., Sun, K. & Yang, H. Y. 3D nitrogen-doped graphene foam with encapsulated germanium/nitrogen-doped graphene yolk-shell nanoarchitecture for high-performance flexible Li-ion battery. *Nat Commun* (2017) doi:10.1038/ncomms13949.

90. He, K. *et al.* Sodiation via Heterogeneous Disproportionation in FeF 2 Electrodes for Sodium-Ion Batteries. **16**, 57 (2024).

91. Nair, A. S. & Pradeep, T. Halocarbon mineralization and catalytic destruction by metal nanoparticles. *JSTOR* (2009).

92. Benn, T. M. & Westerhoff, P. Nanoparticle silver released into water from commercially available sock fabrics. *Environ Sci Technol* **42**, 4133–4139 (2008).

93. Li, X.-Q., Elliott, D. W. & Zhang, W.-X. Zero-Valent Iron Nanoparticles for Abatement of Environmental Pollutants : Materials and Engineering Aspects. *Particulate Systems in Nano- and Biotechnologies* 309–330 (2008) doi:10.1201/9781420007534-14.

94. Zhang, W. X. Nanoscale iron particles for environmental remediation: An overview. *Journal of Nanoparticle Research* **5**, 323–332 (2003).

95. Shim, S. Y., Lim, D. K. & Nam, J. M. Ultrasensitive Optical Biodiagnostic Methods Using Metallic Nanoparticles. *Nanomedicine* **3**, 215–232 (2008).

96. Colino, C. I., Millán, C. G. & Lanao, J. M. Nanoparticles for Signaling in Biodiagnosis and Treatment of Infectious Diseases. *International Journal of Molecular Sciences 2018, Vol. 19, Page 1627* **19**, 1627 (2018).

97. Kairdolf, B. A., Qian, X. & Nie, S. Bioconjugated nanoparticles for biosensing, in vivo imaging, and medical diagnostics. *Anal Chem* **89**, 1015–1031 (2017).

98. Slepička, P., Kasálková, N. S., Siegel, J., Kolská, Z. & Švorčík, V. Methods of Gold and Silver Nanoparticles Preparation. *Materials 2020, Vol. 13, Page 1* **13**, 1 (2019).

99. Eberhardt, W. *et al.* Photoemission from mass-selected monodispersed Pt clusters. *Phys Rev Lett* **64**, 780 (1990).

100. Fayet, P., Patthey, F., Roy, H. V., Detzel, T. & Schneider, W. D. Electronic structure of supported mass-selected transition metal clusters: a photoemission study. *Surf Sci* **269–270**, 1101–1108 (1992).

101. Roy, H. V. *et al.* Evolution of the electronic and geometric structure of size-selected Pt and Pd clusters on Ag(110) observed by photoemission. *Phys Rev B* **49**, 5611 (1994).

102. Vajda, Š., Leisner, T., Wolf, S. & Wöste, L. H. Reactions of size-selected metal cluster ions. *Philosophical Magazine B* **79**, 1353–1366 (1999).

103. Barborini, E., Podestà, A. & Milani, P. Supercapacitors based on nanostructured carbon electrodes grown by cluster-beam deposition Double-Layer Capacitors View project sp carbon View project. *Article in Applied Physics Letters* (1999) doi:10.1063/1.125111.

104. Barborini, E. & Milani, P. Supersonic cluster beam deposition of nanostructured titania. *Eur. Phys. J. D* **24**, 277–282 (2003).

105. Carbone, R. *et al.* Biocompatibility of cluster-assembled nanostructured TiO 2 with primary and cancer cells. *Biomaterials* **27**, 3221–3229 (2006).

106. Marelli, M. *et al.* Flexible and biocompatible microelectrode arrays fabricated by SCBD on SU-8 Flexible and biocompatible microelectrode arrays fabricated by supersonic cluster beam deposition on SU-8 Flexible and biocompatible microelectrode arrays fabricated by SCBD on SU-8 2.

107. Podestà, A. *et al.* Cluster-assembled nanostructured titanium oxide films with tailored wettability. *Journal of Physical Chemistry C* **113**, 18264–18269 (2009).

108. Villa, S. M. *et al.* Soft Piezoionic/Piezoelectric Nanocomposites Based on Ionogel/BaTiO3 Nanoparticles for Low Frequency and Directional Discriminative Pressure Sensing. *ACS Macro Lett* **8**, 414–420 (2019).

109. Barborini, E., Piseri, P. & Milani, P. A pulsed microplasma source of high intensity supersonic carbon cluster beams. *Journal of Physics D: Applied Physics RAPID COMMUNICATION J. Phys. D: Appl. Phys* **32**, 105–109 (1999).

110. Piseri, P., Podestà, A., Barborini, E. & Milani, P. Production and characterization of highly intense and collimated cluster beams by inertial focusing in supersonic expansions. *Review of Scientific Instruments* **72**, 2261–2267 (2001).

111. Barborini, E. *et al.* Nanostructured TiO2 films with 2 eV optical gaps. *Advanced Materials* **17**, 1842–1846 (2005).

112. Ghisleri, C. Patterning of gold--polydimethylsiloxane (Au--PDMS) nanocomposites by supersonic cluster beam implantation. (2014) doi:10.1088/0022-3727/47/1/015301.

113. Von Issendorff, B. & Palmer, R. E. A new high transmission infinite range mass selector for cluster and nanoparticle beams. *Review of Scientific Instruments* **70**, 4497–4501 (1999).

114. Palmer, R. E. *et al.* Size-selected cluster beam source based on radio frequency magnetron plasma sputtering and gas condensation Size-selected cluster beam source based on radio frequency magnetron plasma sputtering and gas condensation Size-selected cluster beam source based on radio frequency magnetron plasma sputtering and gas condensation. *Citation: Review of Scientific Instruments* **76**, 3252 (2005).

115. Haberland, H. *et al.* Thin film growth by energetic cluster impact (ECI): comparison between experiment and molecular dynamics simulations. *Materials Science and Engineering B* **19**, 31–36 (1993).

116. Singh, V. *et al.* Engineering high-performance Pd core–MgO porous shell nanocatalysts via heterogeneous gas-phase synthesis. *Nanoscale* **7**, 13387–13392 (2015).

117. Grammatikopoulos, P., Steinhauer, S., Vernieres, J., Singh, V. & Sowwan, M. Nanoparticle design by gas-phase synthesis. *Adv Phys X* **1**, 81–100 (2016).

118. Alton, G. D. A universal negative or positive ion source. *IEEE Trans Nucl Sci* **26**, 3708–3712 (1979).

119. Krohn, V. E. Emission of Negative Ions from Metal Surfaces Bombarded by Positive Cesium Ions. *J Appl Phys* **33**, 3523–3525 (1962).

120. Reddy, K. R., Lee, K. P., Lee, Y. & Gopalan, A. I. Facile synthesis of conducting polymer–metal hybrid nanocomposite by in situ chemical oxidative polymerization with negatively charged metal nanoparticles. *Mater Lett* **62**, 1815–1818 (2008).

121. Alton, G. *AN AXIAL GEOMETRY CESIUM SPUTTER NEGATIVE ION SOURCE WITH CONTINUOUS TUNGSTEN SURFACE IONIZER. Nuclear Instruments and Methods in Physics Research* vol. 244 (1986).

122. Hall, S. G. *et al.* Compact sputter source for deposition of small size-selected clusters ⬚ Compact sputter source for deposition of small size-selected clusters. *Rev. Sci. Instrum* **68**, 3335–3339 (1997).

123. Pratontep, S. *et al.* Scaling Relations for Implantation of Size-Selected Au, Ag, and Si Clusters into Graphite. (2003) doi:10.1103/PhysRevLett.90.055503.

124. Zhao, J., Cao, L., Palmer, R. E., Nordlund, K. & Djurabekova, F. Formation and emission mechanisms of Ag nanoclusters in the Ar matrix assembly cluster source. *Phys Rev Mater* **1**, 066002 (2017).

125. Spadaro, M. C. *et al.* Size control of Au nanoparticles from the scalable and solvent-free matrix assembly cluster source. *Journal of Nanoparticle Research* **22**, 1–6 (2020).

126. Vernieres, J. *et al.* Influence of air exposure on structural isomers of silver nanoparticles. *Communications Chemistry 2023 6:1* **6**, 1–5 (2023).

127. Cai, R., Jian, N., Murphy, S., Bauer, K. & Palmer, R. E. A new method to prepare colloids of size-controlled clusters from a matrix assembly cluster source. *APL Mater* **5**, (2017).

128. Palmer, R. E., Cao, ; L & Yin, ; F. Note: Proof of principle of a new type of cluster beam source with potential for scale-up. doi:10.1063/1.4947229.

129. Oiko, V. T. A., Mathieu, T., Cao, L., Liu, J. & Palmer, R. E. Note: Production of silver nanoclusters using a Matrix-Assembly Cluster Source with a solid CO2 matrix. *Journal of Chemical Physics* **145**, (2016).

130. Xu, J. *et al.* Cluster Beam Deposition of Ultrafine Cobalt and Ruthenium Clusters for Efficient and Stable Oxygen Evolution Reaction. *ACS Appl Energy Mater* **1**, 3013–3018 (2018).

131. Cai, R. *et al.* Scale-up of cluster beam deposition to the gram scale with the matrix assembly cluster source for heterogeneous catalysis (propylene combustion). *AIP Adv* **10**, (2020).

132. Cai, R. *et al.* Scale-Up of Cluster Beam Deposition to the Gram Scale with the Matrix Assembly Cluster Source for Heterogeneous Catalysis (Catalytic Ozonation of Nitrophenol in Aqueous Solution). *ACS Appl Mater Interfaces* **12**, 24877–24882 (2020).

133. Iijima, S. & Ichihashi, T. PHYSICAL REVIEW LETTERS Structural Instability of Ultrafine Particles of Metals. (1986).

134. Jennison, D. R., Schultz, P. A. & Sears, M. P. Ab initio calculations of Ru, Pd, and Ag cluster structure with 55, 135, and 140 atoms. *Journal of Chemical Physics* **106**, 1856–1862 (1997).

135. Koga, K., Ikeshoji, T. & Sugawara, K.-I. Size-and Temperature-Dependent Structural Transitions in Gold Nanoparticles. *The American Physical Society* **92**, 115507–115508 (2004).

136. Kuo, C.-L. & Clancy, P. Melting and Freezing Characteristics and Structural Properties of Supported and Unsupported Gold Nanoclusters. (2005) doi:10.1021/jp0518862.

137. Li, Z. Y. *et al.* Three-dimensional atomic-scale structure of size-selected gold nanoclusters. *Nature 2007 451:7174* **451**, 46–48 (2007).

138. Wang, Z. W. & Palmer, R. E. Determination of the ground-state atomic structures of size-selected Au nanoclusters by electron-beam-induced transformation. *Phys Rev Lett* **108**, 245502 (2012).

139. Chadderdon, X. H., Chadderdon, D. J., Pfennig, T., Shanks, B. H. & Li, W. Paired electrocatalytic hydrogenation and oxidation of 5-(hydroxymethyl)furfural for efficient production of biomass-derived monomers. *Green Chemistry* **21**, 6210–6219 (2019).

140. Sanghez De Luna, G. *et al.* Ag Electrodeposited on Cu Open-Cell Foams for the Selective Electroreduction of 5-Hydroxymethylfurfural. (2020) doi:10.1002/celc.201902161.

141. Bose, S. K., Mallinson, J. B., Gazoni, R. M. & Brown, S. A. Stable Self-Assembled Atomic-Switch Networks for Neuromorphic Applications. *IEEE Trans Electron Devices* **64**, 5194–5201 (2017).

142. Bose, S. K. *et al.* Neuromorphic behaviour in discontinuous metal films. *Nanoscale Horiz* **7**, 437–445 (2022).

143. Minnai, C., Bellacicca, A., Brown, S. A. & Milani, P. Facile fabrication of complex networks of memristive devices. *Scientific Reports 2017 7:1* **7**, 1–8 (2017).

144. Mirigliano, M. *et al.* Non-ohmic behavior and resistive switching of Au cluster-assembled films beyond the percolation threshold †. (2019) doi:10.1039/c9na00256a.

145. Marinella, M. J. & Agarwal, S. Efficient reservoir computing with memristors. *Nature Electronics 2019 2:10* **2**, 437–438 (2019).

146. Chu, M. *et al.* Neuromorphic Hardware System for Visual Pattern Recognition with Memristor Array and CMOS Neuron. *IEEE Transactions on Industrial Electronics* **62**, 2410–2419 (2015).

147. Zhu, X., Wang, Q. & Lu, W. D. Memristor networks for real-time neural activity analysis. *Nature Communications 2020 11:1* **11**, 1–9 (2020).

148. Zhong, Y. *et al.* A memristor-based analogue reservoir computing system for real-time and power-efficient signal processing. *Nature Electronics 2022 5:10* **5**, 672–681 (2022).

149. Fukamori, Y. *et al.* Fundamental insight into the substrate-dependent ripening of monodisperse Clusters. *ChemCatChem* **5**, 3330–3341 (2013).

150. Freund, L. B. & Suresh, S. *Thin Film Materials Stress, Defect Formation and Surface Evolution*. (Cambridge University Press, 2003).

151. Carroll, S. J., Weibel, P., Issendorff, B. von, Kuipers, L. & Palmer, R. E. The impact of size-selected Ag clusters on graphite: an STM study. *Journal of Physics: Condensed Matter* **8**, L617–L624 (1996).

152. Freund, L. B. & Suresh, S. *Thin Film Materials Stress, Defect Formation and Surface Evolution*. (Cambridge University Press, 2003).

153. Fisher Scientific - Technical Publications Hillsboro, T. *Talos Basic General Information*. https://www.mcgill.ca/femr/files/femr/tfs_talos_basic_guide.pdf (2019).

154. Nelli, D., Rossi, G., Wang, Z., Palmer, R. E. & Ferrando, R. Structure and orientation effects in the coalescence of Au clusters. *Nanoscale* **12**, 7688–7699 (2020).

155. Kelly, K. L., Coronado, E., Zhao, L. L. & Schatz, G. C. The optical properties of metal nanoparticles: The influence of size, shape, and dielectric environment. *Journal of Physical Chemistry B* **107**, 668–677 (2003).

156. Schmid, G. & Simon, U. Gold nanoparticles: assembly and electrical properties in 1–3 dimensions. *Chemical Communications* 697–710 (2005) doi:10.1039/B411696H.

157. Li, Z., Chai, F., Yang, L., Luo, X. & Yang, C. Mechanical properties and nanoparticles precipitation behavior of multi-component ultra high strength steel. *Mater Des* **191**, 108637 (2020).

158. James Brian, Huya-Kouadio Jennie & Houchins Cassidy. 2017 DOE Hydrogen and Fuel Cells Program Review Fuel Cell Systems Analysis. 15 https://www.hydrogen.energy.gov/pdfs/review17/fc163_james_2017_o.pdf (2017).

159. Bubnov, A. G., Grinevich, V. I. & Maslova, O. N. Barrier-discharge plasma treatment of surface water to remove organic compounds. *Russian Journal of Applied Chemistry* **79**, 934–940 (2006).

160. Kaur, G., Singh, H. P., Batish, D. R. & Kohli, R. K. A time course assessment of changes in reactive oxygen species generation and antioxidant defense in hydroponically grown wheat in response to lead ions (Pb2+). *Protoplasma* **249**, 1091–1100 (2012).